Demonstrating Quantum Speed-Up with a Two-Transmon Quantum Processor.

Andreas Dewes

June 12, 2012

Contents

List of Figures

List of Tables

Chapter 1

Introduction & Summary

1.1 Quantum Computing & Circuit Quantum Electrodynamics

This thesis presents experiments performed with a superconducting two-qubit quantum processor. The main goal of this work was to demonstrate a possible quantum computing architecture based on superconducting qubits that follows the canonical blueprint of a quantum processor as sketched in fig. 1.1, in accordance with the five criteria formulated by DiVincenzo (2000). By this definition, a universal quantum computer is a register of well-defined quantum bits (1) with long coherence times (2) on which one can implement any unitary evolution using a universal set of quantum gates (3), fitted with individual high fidelity readout of each qubit (4) and with qubit reset in their ground state (5).

Implementing this allegedly simple list of requirements in a system of superconducting qubits has been a major research challenge during the last decade. The observation of quantum tunneling of a current-biased Josephson junction out of its zero-voltage state by Devoret et al. (1985); Martinis et al. (1985), first demonstrated that an electrical vari-

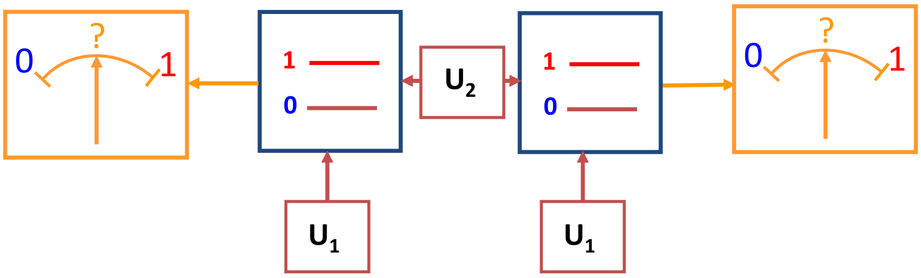

Figure 1.1: The blueprint of a “canonical” two-qubit quantum processor. The two qubits can be individually manipulated (U_1) and a by a universal two-qubit gate U_2 can be applied to them. Each of the qubits can be read out individually.

able such as the superconducting phase difference across a Josephson junction can exhibit quantum properties. This phase and the number of Cooper pairs transferred across the junction are conjugated variables that form a single degree of freedom. The observation of microwave induced transitions between quantum states of the system by Martinis et al. (1985) further confirmed the quantum nature of this degree of freedom (See also Martinis et al. (1985, 1987); Clarke et al. (1988)). A somewhat simpler quantum electrical circuit called the single Cooper Pair Box was later developed in the Quantronics group during the 1990s (Bouchiat et al., 1998) !1! . This circuit consists of a Josephson junction in series with a gate capacitor, and connected to a voltage source (include figure ?). Nakamura et al. (1999) first demonstrated with the Cooper Pair Box the coherent superposition of two quantum states in an electrical circuit, which was the first superconducting qubit experiment. Although the achieved coherence time was quite short, in the 5-10 ns range, this result attracted a huge interest and triggered the active development of research on superconducting quantum qubits. In the years after Nakamuras experiment, several types of superconducting qubits were proposed using Josephson junctions in different configurations. Different regimes, in which the quantum state of the junctions ranges from almost number states to phase states, were realized. Let us cite here the flux qubit (Mooij et al., 1999; Chiorescu et al., 2003). On the side of Cooper Pair Boxes, Vion et al. (2002) made a significant progress by operating a new version of the Cooper Pair Box called the *Quantronium*, fitted with a strategy for fighting dephasing due to the noise of the electrical control parameters, and with single-shot readout (although with limited fidelity). The robustness of the quantronium arises from its operation at a so-called sweet spot where the qubit frequency is stationary respectively to variations of the control parameters. The improved performance of the quantonium allowed to perform all the basic manipulations possible on spins and more generally on two level systems (Collin et al., 2004). Shortly after, another Cooper pair box design, inspired from cavity QED, was developed at Yale by Wallraff et al. (2004). In this so-called circuit-QED design, the Cooper Pair Box, embedded in a microwave resonator, can be thought as an artificial atom in a resonant cavity, and the resonator transmission (or reflection) gives access to the qubit state (Blais et al., 2004). In this CQED circuit, qubit readout is obtained through the cavity pull of the resonator frequency controlled by the qubit state, hence its name of dispersive readout method. This small frequency change results in a small phase change of a resonant microwave pulse, which yields after sufficient the probability of the two qubit states. Another great bonus of circuit QED is that the electromagnetic environment in which the qubit relaxes its energy consists of a microwave resonator with a controllable impedance. The modern version of the Cooper Pair Box called *Transmon*, follows this design with an extra feature that makes it insensitive to the charge noise that plagues single electron and single Cooper Pair devices. This feature consists in operating the Cooper Pair Box in the phase regime

Comment 1: I changed the reference to V. 1998 paper since I didn't find any publication from 1997 by adding an extra capacitance to the junction one and to exploit at all orders the trick exploited. Being at the sweet spot everywhere, the qubit frequency is totally insensitive to the gate charge, and hence to the charge noise. This new design, that however still leaves sufficient anharmonicity to operate the device as a qubit and allows to drive it, yielded a sizeable improvement in coherence times, qubit robustness and usability. Recently, a new type of CQED architecture has been developed by Paik et al. (2011) that combines Transmon qubits with 3D cavities instead of CPW resonators, resulting again in an impressive increase of qubit coherence times of up to two orders of magnitude, with reported qubit relaxation times as high as $80\ \mu s$!1! and decoherence times at a comparable time scale. These drastically improved coherence times have already made possible the realization of elemental quantum feedback and error correction schemes with these systems !2! .

To Do 1: verify this!

To Do 2: cite Irfan's paper here

The progress achieved on the Cooper Pair Box during the last decade has benefited to quantum processors, but, the CQED processors operated prior to this work did not follow the rules established by DiVincenzo (2000). So far, superconducting CQED processors with up to three qubits have been realized and two- and three-qubit quantum gates (Fedorov et al., 2011), multi-qubit entanglement (DiCarlo et al., 2010) and simple quantum algorithms (DiCarlo et al., 2009) as well as quantum error correction recently (Reed et al., 2011) have been demonstrated. These processors were all fitted with joint readout, which allows to measure the average value of a collective variable of the qubit register. By repeating a given sequence of gates a large number of times, one can nevertheless determine the quantum state at that stage of the algorithm being run, and probe it. Since the whole interest of quantum computing is to perform computational tasks more efficiently than achieved by sequential classical processors, it was nevertheless essential, in our mind, to demonstrate the quantum speed-up expected from quantum algorithms with a CQED quantum processor.

At the beginning of this thesis work, quantum speed-up of quantum algorithms had been demonstrated in an electrical quantum processor solely for the Deutsch-Josza algorithm with a phase qubit processor using a destructive readout**?**. Since the Deutsch-Josza algorithm has no mathematical interest, the demonstration of a superconducting quantum processor approaching more closely the DiVincenzo criteria, and able to demonstrate quantum speed-up, was an important goal to achieve. The research presented in this thesis precisely aims to complement the CQED architecture by combining a multi-qubit architecture based on Transmon qubits following the canonical blueprint and able to demonstrate quantum speed-up.

The first part of the thesis discusses the realization of a superconducting two-qubit processor based on Transmon qubits fitted with individual single-shot readouts. With this processor, we implement elementary one- and two-qubit quantum operations and use it to run a simple quantum algorithm that demonstrates probabilistic quantum speed-up. Finally, we discuss the realization of a four-qubit quantum processor using a more scalable approach that could possibly be extended to an even larger number of qubits.

1.2 Realizing a Two-Qubit Quantum Processor

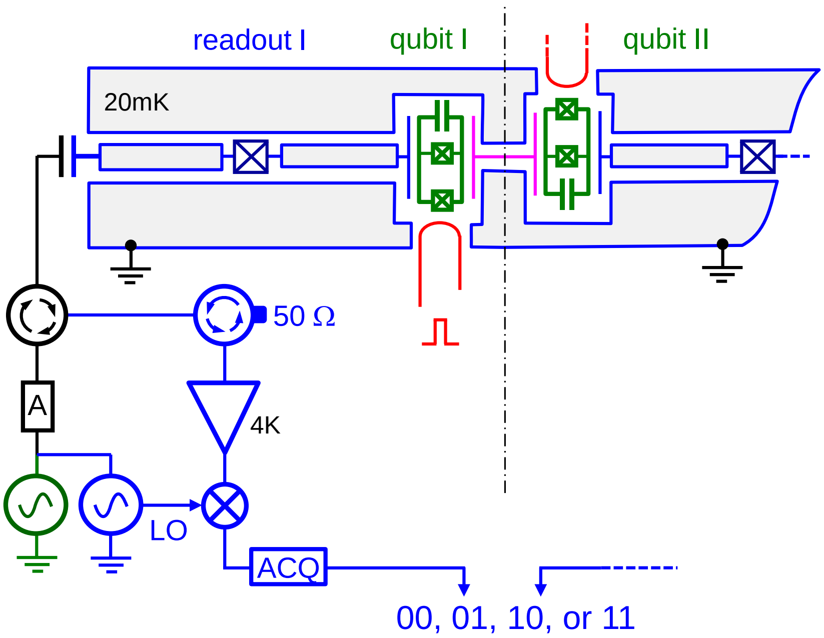

Figure 1.2: Circuit schematic of the two-qubit processor realized in this work, showing the two qubits in green, the qubit readouts in blue and the fast flux lines in red. Each qubit is embedded in its own nonlinear readout resonator and can be driven and read out through an individual microwave line.

The quantum processor implemented in this work is shown in fig. 1.2. It consists of two superconducting quantum bits of the Transmon type, each equipped with its own drive and readout circuit. In order to obtain a high fidelity single-shot readout of the qubit register, we used the Josephson Bifurcation Amplifier (JBA) readout method first developed in the team of Michel Devoret at Yale for the quantronium qubit (Siddiqi et al., 2004; Vijay et al., 2009). This method had indeed already been successfully adapted to the transmon, and yielded a 93 % readout fidelity (Mallet et al., 2009). The qubit read-out is realized using a nonlinear coplanar-waveguide resonator that serves as a *cavity bifurcation amplifier* (CBA)(Siddiqi et al., 2006; Vijay et al., 2009) and allows a single-shot readout of the qubit state (Mallet et al., 2009). Each qubit can be manipulated by driving it with microwave pulses through its readout resonator, allowing for robust and fast single-qubit operations. The qubit frequencies can be tuned individually using fast flux lines, allowing us to change the frequency of each qubit over a range of several GHz. The coupling between the two qubits is realized through a fixed capacitance that connects the two top-electrodes of the Transmons and implements a fixed σ_{xx}-type qubit-qubit coupling. This coupling allows us to generate entangled two-qubit states and to implement a two-qubit gate. We use this simple processor to generate entangled two-qubit states, test the Bell inequality, implement a universal two-qubit gate and perform a simple quantum algorithm that demonstrates quantum speed-up, as will be discussed in the following sections.

1.3 Demonstrating Simultaneous Single-Shot Readout

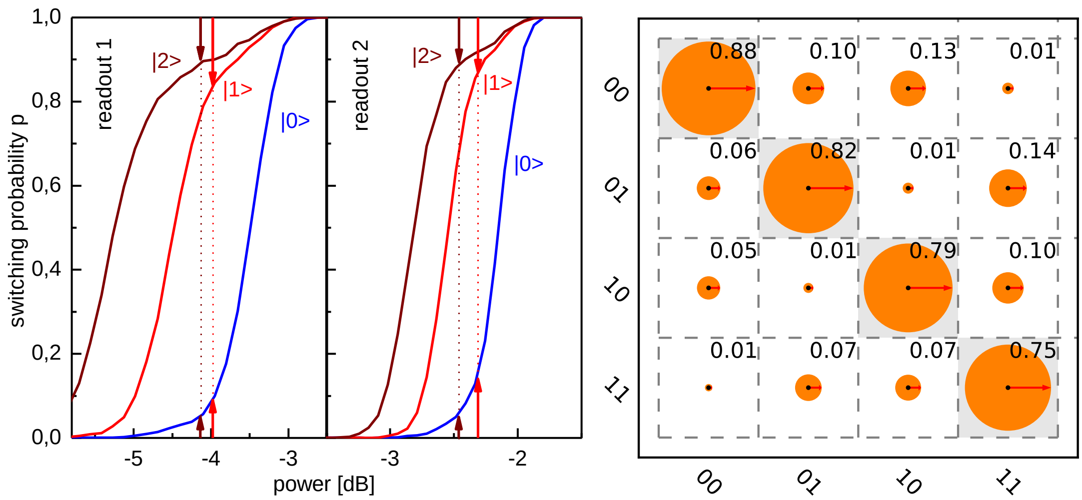

Figure 1.3: a) Switching probabilities of the two qubit readouts as a function of the readout drive power at a fixed driving frequency. The measurement is performed after preparing the qubits in the states $|0\rangle$, $|1\rangle$ and $|2\rangle$. The readout contrast is given as the difference in probability between the curves corresponding to the states $|0\rangle$ and $|1\rangle$ or $|2\rangle$, respectively. The highest contrasts of 88 and 89 % are achieved when the qubit is in state $|2\rangle$. b) Readout matrix of the two-qubit system. This matrix contains the probabilities to obtain the different readout outcomes after having prepared the system in the different computational basis states.

For the readout, each qubit is capacitively coupled to a coplanar waveguide resonator made nonlinear by placing a Josephson junction in its central conductor. We exploit the frequency pull of the bifurcation transition that occurs in such a resonator when driven at a suitable frequency and power to map the qubit state on the bifurcation state of the cavity, which is then measured by reflectometry. Here the hysteretic character of the bifurcation transition allows to reduce the power and to determine the bifurcation state without further affecting the qubit. The state of the resonator can thus be determined reliably without being limited by qubit relaxation, thereby providing a high-fidelity single-shot qubit readout. Contrary to previous CQED processors, our processor is fitted with individual readout, and a simultaneous readout of the full two-qubit register is possible, as requested by the DiVincenzo criteria. For single-qubit CBA readouts, readout fidelities up to 93 % have been reported (Mallet et al., 2009). However, due to the higher complexity and design constraints of our system, only 83-89 % fidelity has been achieved for the processor presented here. The full characterization of the readout of our processor is shown in fig. 1.3. Fig. 1.3a shows the switching probabilities of each individual qubit readout as a function of the drive amplitude, measured at a fixed drive frequency. Individual curves correspond to the qubit being prepared in different states $|0\rangle$, $|1\rangle$ or $|2\rangle$, the difference between either two curves giving the readout contrast between those qubit states. Preparing the qubit in state $|2\rangle$ before readout can increase the readout fidelity by more than 10 % and is therefore often used in the experiments presented in this thesis. Fig. 1.3b shows the full readout matrix of the two-qubit register that relates measured readout switching probabilities with real qubit state occupation probabilities and allows us to correct readout errors when performing quantum state tomography. In the main text of this thesis we discuss all relevant readout fidelities and errors in detail and analyze different error sources limiting the readout performance in our experiments.

1.4 Generating and Characterizing Entanglement

The capacitive coupling between the two qubits provides a σ_{xx}-type interaction that can be used to generate entangled two-qubit states. Conveniently, this coupling is only effective when the qubit frequencies are near-resonant and can therefore be effectively switched on and off by tuning the qubit frequencies in and out of resonance. For the processor realized in this work, the effective coupling constant g of the two qubits has been measured as $2g/2\pi = 8.2\ \mathrm{MHz}$. When the two qubits are in resonance, the effective evolution operator of the two-qubit system is:

$$U(t) = \begin{pmatrix} 1 & 0 & 0 & 0 \\ 0 & \cos 2\pi tg & i\sin 2\pi tg & 0 \\ 0 & i\sin 2\pi tg & \cos 2\pi tg & 0 \\ 0 & 0 & 0 & 1 \end{pmatrix} \tag{1.1}$$

where $U(t)$ is written in the basis $\{|00\rangle, |01\rangle, |10\rangle, |11\rangle\}$. By using fast flux pulses to non-adiabatically tune the qubits in and out of resonance we can switch on this interaction for a well-defined time. We first characterize the effect of the coupling on the qubit register by preparing the state $|10\rangle$, tuning the qubits in resonance for a given time and measuring the qubit state afterwards. The resulting curve is shown in fig. 1.4 and shows

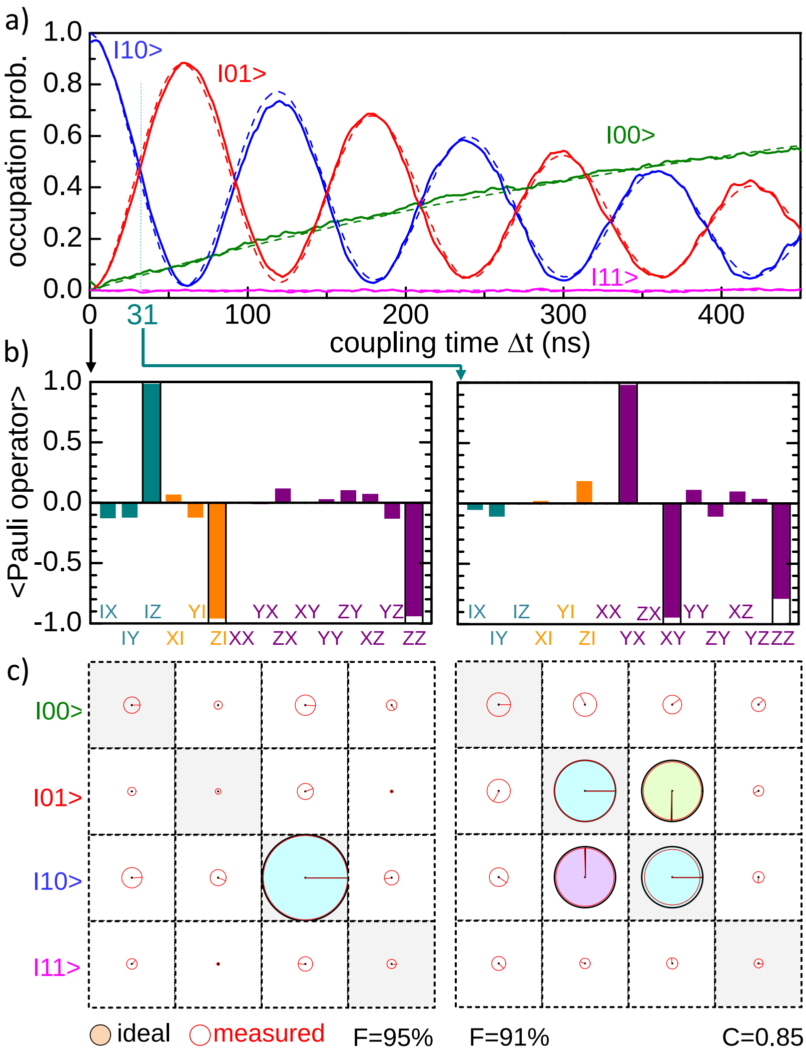

Figure 1.4: Swapping oscillations between the two qubits induced by a resonant interaction between them. a) Qubit state probabilities after a swapping time Δt. The frequency of the oscillations corresponds to $2g/2\pi = 8.7\ \mathrm{MHz}$. b) Measurement of the Pauli set of the two-qubit state at times $0\ \mathrm{ns}$ and $31\ \mathrm{ns}$. c) The reconstructed density matrices corresponding to the two measured Pauli sets. In c), the area of each circle corresponds to the absolute value of each matrix element and the color and direction of the arrow give the phase of each element. The black circles correspond to the density matrices of the ideal states $|10\rangle$ and $1/\sqrt{2}/(|10\rangle + i\,|01\rangle)$, respectively. Figure Comment 2: verify sign!

swapping oscillations between the two qubits. Analyzing this curve allows us to extract the effective coupling strength between the qubits. Leaving the interaction between the qubits on for a well-defined time allows us to generate entangled Bell states that we characterize by performing quantum state tomography. The experimental reconstruction of the density matrix of such a Bell-state of the type $|\psi\rangle = 1/\sqrt{2}(|01\rangle + i\,|10\rangle)$ is shown in fig. 1.4b. The measured fidelity of the prepared state of 91 % and the concurrence of 85 % confirm that entanglement is present in the system. We also characterize the entanglement between the two qubits by measuring the so-called *Clauser-Horne-Shimony-Holt* operator (Clauser et al., 1969), which combines measurements of the state of the two qubits along different axes on the Bloch sphere and provides a test that can distinguish between classical correlation and quantum entanglement in a two-qubit system.

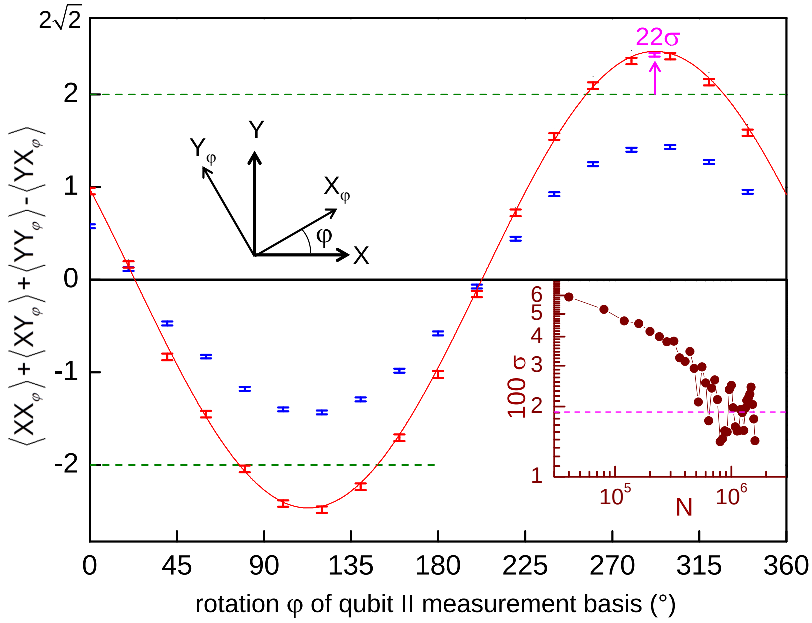

Figure 1.5: Measurement of the CHSH operator for an entangled two-qubit state. The renormalized CHSH expectation value (red points) exceeds the classical boundary of 2 by a large amount. The raw measurement data (blue points) lies below this critical threshold. The inset shows the standard deviation σ at the highest point of the curve as a function of the measurement sample size. For the highest sample count, the classical boundary is exceeded by 22 standard deviations.

For classical states, the maximum value of the CHSH operator is bound by 2 but for entangled states it can reach a maximum of $2\sqrt{2}$. Fig. 1.5 shows the result of such a CHSH-type measurement performed on a state created by the method described above, showing the value of $\langle\mathrm{CHSH}\rangle$ as a function of the angle ϕ of the measurement basis (more details about the measurement and the preparation of the entangled state can be found in the main text). We observe a violation of the classical boundary 2 of the operator by 22 standard deviations when correcting the readout errors that are present in our system. The raw, uncorrected data fails to exceed the classical threshold because of readout errors mainly caused by qubit relaxation during the readout. Nevertheless, the observed violation of the equation in the calibrated data is a strong indication of entanglement in the system.

1.5 Realizing a Universal Two-Qubit Quantum Gate

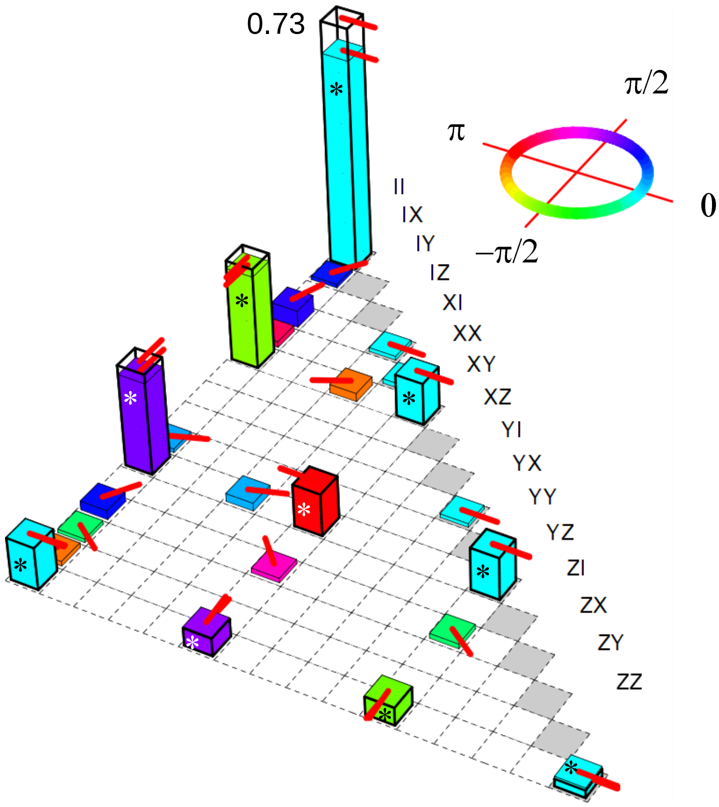

Figure 1.6: The measured χ-matrix of the implemented $\sqrt{i\mathrm{SWAP}}$ gate. The row labels correspond to the indices of the E_i operators, the height of each bar to the absolute value of the corresponding matrix element and the color and direction of the red arrow to the complex phase of each element. The ideal χ-matrix of the $i\sqrt{\mathrm{SWAP}}$ gate is given by the outlined bars. The upper half of the positive-hermitian matrix is not shown.

The swapping evolution given by eq. (1.1) allows not only to prepare entangled two-qubit states but also to implement of a two-qubit universal gate. When switching on the interaction for a time $t_{\pi/2} = 1/8g$ one realizes the so-called $\sqrt{i\mathrm{SWAP}}$ gate, which has the representation

$$U(t) = \begin{pmatrix} 1 & 0 & 0 & 0 \\ 0 & 1/\sqrt{2} & i\sqrt{2} & 0 \\ 0 & i\sqrt{2} & 1/\sqrt{2} & 0 \\ 0 & 0 & 0 & 1 \end{pmatrix} \tag{1.2}$$

and is a universal two-qubit quantum gate. We characterize the operation and errors of our implementation of this gate by performing quantum process tomography, obtaining a gate fidelity of 90 % . The 10 % error in gate fidelity is caused mainly by qubit relaxation and dephasing during the gate operation and only marginally by deterministic preparation errors, as will be discussed in the main text of the thesis. Fig. 1.6 shows the measured χ matrix of the gate, that describes its effect in the Pauli basis of two-qubit operators. The χ matrix provides the full information on the unitary and non-unitary action of the gate. The achieved fidelity of the gate operation is sufficient to allow the implementation of simple quantum algorithms with our processor.

1.6 Running a Quantum Search Algorithm

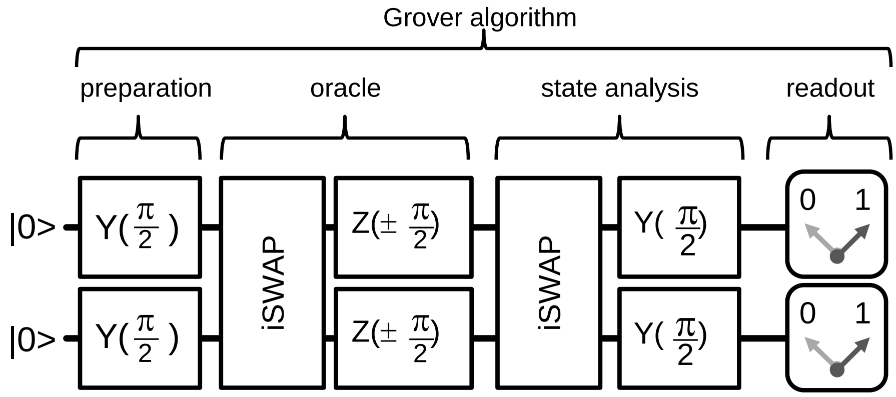

Figure 1.7: Implementation of the Grover search algorithm on our two-qubit quantum processor. The algorithm consists in preparing a fully superposed state, applying a given Oracle operator to it, and analyzing the resulting output to determine the quantum state tagged by this Oracle operator with only a single call.

The implementation uses a two-qubit quantum gate related to the one described above to run a simple quantum algorithm on our processor, the so called *Grover search algorithm* (Grover, 1997). The version of this algorithm that we implemented operates on a two-qubit basis $x_i \in \{ |00\rangle , |01\rangle, |10\rangle , |11\rangle\}$ and can distinguish between four different *Oracle functions* $f(x)$ with $x \in x_i$ that each tag one given basis state x_j. In the two-qubit case, this algorithm requires only one evaluation of the Oracle function $f(x)$, which is now an operator, to determine which state among the four possible ones it tags. This case thus provides a simple benchmark of the operation of the quantum processor, and a simple and illustrative example of quantum speed-up in comparison with classical algorithms (although there are some subtleties, as discussed in the main text). The diagram of the Grover search algorithm implemented in our processor is shown in fig. 1.7 and involves two $i\mathrm{SWAP}$ gate operations and six single-qubit operations along with a single-shot qubit readout at the end of the algorithm. We measured the success probability of the algorithm from the obtained outcomes, and completed the analysis of its operation by performing the tomography of the quantum state at different steps of the algorithm. We first discuss this evolution that sheds light on how quantum speed-up is achieved.

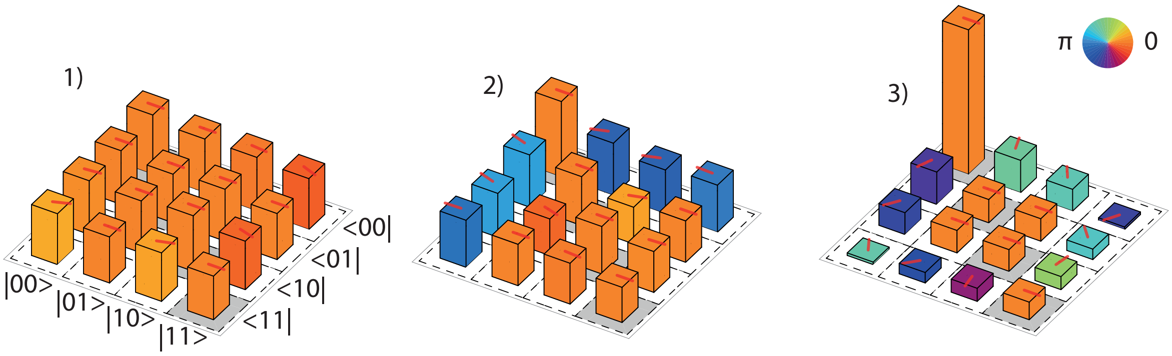

Figure 1.8: Measured density matrices when running the Grover search algorithm with a search oracle marking the state $|00\rangle$. 1) shows the state after the generalized Hadamard transform, 2) after applying the quantum oracle and 3) after the final step of the algorithm.

Fig. 1.8 shows the density matrices determined experimentally when running the Grover search algorithm with the Oracle operator that tags the state $|00\rangle$. State tomography is first shown after preparation with a generalized Hadamard transform applied to the initial state $|00\rangle$. It clearly corresponds then to the superposition of all the computational basis states, as often done in quantum algorithms. The quantum state after the quantum Oracle is more subtle since the information on the tagged state is encoded in the phase of tha matrix elements involving $|00\rangle$ once only. At the end of the algorithm, the tomography displays a large peak on state $|00\rangle$, as expected. The fidelity of the final quantum state of the algorithm is 68%, 61%, 64% and 65% for the four different Oracle operators, respectively. These fidelities, corrected for readout errors, do not quantify the quantum speed-up achieved when running the algorithm. For this, it is necessary to analyze the uncorrected single-shot readout outcomes.

1.7 Demonstrating Quantum Speed-Up

The main interest of running a quantum algorithm is to obtain an advantage in the run-time in comparision to a classical algorithm, the so-called *quantum speed-up*. To characterize this quantum speed-up as obtained with our processor, we run the Grover algorithm for all four possible Oracle functions and directly read out the state of the qubit register after the last step of the algorithm instead of performing quantum state tomography, thus not correcting any readout errors. By averaging the outcomes of many such individual runs of the algorithm with different Oracle functions we obtain the so-called *single-run fidelities*, which –for the four different Oracle functions– have been measured as 66%, 55%, 61% and 52%. The full probability distributions for the four possible cases

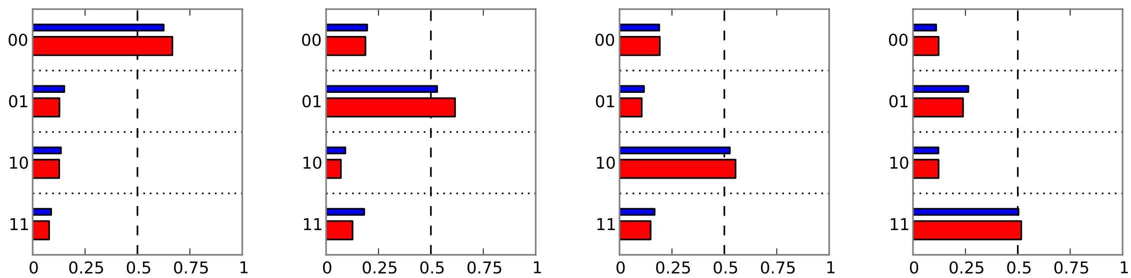

Figure 1.9: Single-run results when running the Grover search algorithm on our two-qubit quantum processor. Shown are the probabilities of obtaining the results $00, 01, 10, 11$ as a function of the Oracle function provided to the algorithm, indicated by the number on top of each graph. In all four cases, the success probability of the algorithm is $> 50\%$, thus outperforming any classical query-and-guess algorithm in the required number of calls to the Oracle function.

and are shown in fig. 1.9. The achieved success probability is always lower than the theoretically possible value of 100 % , mainly because of relaxation and decoherence of the qubit state during the runtime of the algorithm, and also of errors in the pulse sequence, but to a small degree. The measured success probabilities are however larger than the $> 50\%$ success probability of a classical query-and-guess algorithm using the outcome of a single query, which demonstrates the quantum speed-up achieved with our processor, as explained in greater detail in the main text. Indeed, a random query-and-guess allows either to find the searched state, or to rule out one, which yields to guess the correct answer with $> 50\%$ probability instead of with $> 25\%$ for a random guess-and-check. However, since the gain obtained from a query-and-guess algorithm is not scalable, the comparison with the $> 25\%$ guess-and-check success probability is more relevant.

Chapter 2

Theoretical Foundations

The goal of this chapter is to provide the theoretical foundations needed to interpret and analyze the experiments discussed in the following chapters. We will therefore briefly introduce some basic concepts of quantum mechanics and quantum computing, discuss Transmon qubits and circuit quantum electrodynamics (CQED) and introduce the reader to the *cavity bifurcation amplifier (CBA)* that we use in our experiments. More detailed discussions of the properties of all the circuit components discussed here will be provided in the relevant sections of the "Experiments" chapter.

2.1 Clasical & Quantum Information Processing

By definition, computing designates the activity of using computer hardware and software to process information, or *data*. Classical information processing can be divided in so-called *analog and digital information processing*, the former being based on continously changeable physical quantities whereas the latter is based on incrementally changeable quantities. The fundamental unit of digital information processing is the so-called *bit*, which represents a boolean (true/false) information. The discipline of theoretical computer science has been created to investigate the fundamental limits and properties of classical information processing. One of the main foundational theorems of theoretical computer science is the so-called *Church-Turing thesis* which provides a universal computing model by saying (basically) that everything which is computable can be efficiently computed using a *Turing machine*. Such a Turing machine, in turn, is a simple theoretical devices which is able to run programs that operates on a discrete set of data using a well-specified set of operations. The Turing machine is universal in the sense that any other classical computing device can be efficiently simulated using a Turing machine with the appropriate program and data.

Surprisingly, Richard Feynman discovered in the early 1980 that a classical Turing machine as described above would be unable to efficiently simulate a quantum-

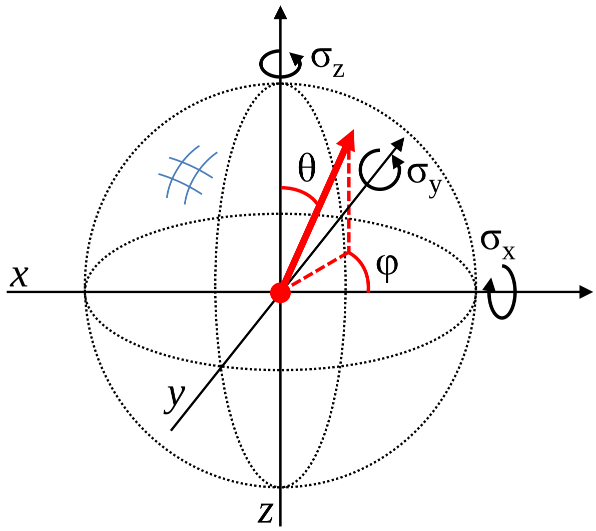

Figure 2.1: The Bloch sphere representation of a qubit state $|\psi\rangle = \cos\frac{\theta}{2}|0\rangle + e^{i\phi}\sin\frac{\theta}{2}|1\rangle$. The state $|\psi\rangle$ is fully characterized by specifying its "altitude" and "azimuth" angles θ and ϕ. Pure quantum states will always lie on the surface of the Bloch sphere, whereas mixed quantum states can also lie anywhere inside the sphere.

mechanical system (Feynman, 1982). A few years later, David Deutsch took up Feynman's idea and developed an information processing framework based on quantum mechanics. He showed that by using this so-called *quantum computing* or *quantum information processing* framwork one could solve certain problems faster than would be possible with any classical Turing machine (Deutsch, 1985). The work by Feynman and Deutsch created a large interest in the physics community and led to a huge experimental and theoretical effort aimed at realizing a working quantum computer.

2.2 Principles of Quantum Computing

In this section we will discuss the basic principles of quantum computing, including quantum bits and quantum gates. We will also briefly dicsuss some examples of quantum algorithms that are relevant to this work.

2.2.1 Quantum Bits

Similar to classical computing, in quantum computing one can define a fundamental unit of information, the so called *quantum bit* or *qubit*. Such a qubit is a quantum-mechanical two-level system described by the wavefunction

$$|\psi\rangle = \cos\frac{\theta}{2}|0\rangle + e^{i\phi}\sin\frac{\theta}{2}|1\rangle \tag{2.1}$$

As can be seen, the state of such a qubit can be described by a pair of real numbers θ and ϕ that characterize the occupation probability of each of the two basis states $|0\rangle$ and $|1\rangle$ and the phase between them. A useful and intuitive representation of such a single-qubit state is the so-called *Bloch sphere representation* of a quantum state, which is shown in fig. 2.1. In this representation, the state $|\psi\rangle$ is located on a unit sphere. The north and south poles of this sphere correspond to the qubit states $|0\rangle$ and $|0\rangle$. All states lying between those two correspond to superposition states, which are characterized by their "altitude" and "azimuth" angles θ and ϕ.

2.2.2 Quantum Gates

Analogously to classical information processing it is necessary to define *quantum gates* which act on individual or multiple qubits and allow us to process information with them. In the most general sense, a quantum gate is a unitary quantum operator that acts on one or several qubits. Theoretically there is an infinite number of possible quantum gates, however in order to describe all possible quantum operations that can be performed on a register of qubits it is sufficient to defined an *universal set of quantum gates*. Such a universal gate set that will be especially relevant to this work consists of the three single-qubit rotation matrices

$$R_x(\theta) = \begin{pmatrix} \cos\theta/2 & -i\sin\theta/2 \\ -i\sin\theta/2 & \cos\theta/2 \end{pmatrix} \tag{2.2}$$

$$R_y(\theta) = \begin{pmatrix} \cos\theta/2 & -\sin\theta/2 \\ +\sin\theta/2 & \cos\theta/2 \end{pmatrix} \tag{2.3}$$

$$R_z(\theta) = \begin{pmatrix} e^{-i\theta/2} & 0 \\ 0 & e^{+i\theta/2} \end{pmatrix} \tag{2.4}$$

togehter with the so-called $i\mathrm{SWAP}$ two-qubit operator, which has the representation

$$i\mathrm{SWAP} = \begin{pmatrix} 1 & 0 & 0 & 0 \\ 0 & 0 & -i & 0 \\ 0 & -i & 0 & 0 \\ 0 & 0 & 0 & 1 \end{pmatrix} \tag{2.5}$$

in the basis $(|00\rangle, |01\rangle, |10\rangle, |11\rangle)$. Often we will represent these gates schematically as shown in fig. **??**.

2.2.3 Quantum Algorithms

The interest in quantum computing is mainly due to the fact that certain problems can be solved faster on a quantum computer than on a classical computer. By faster we mean here that the order $\mathcal{O}$ of the runtime of the algorithm increases faster on a classical computer than on a quantum computer as a function of the problem size. Up to this day it has not been shown that a quantum computer can perform all tasks faster than a classical computer, however certain real-world problems have been found that can be solved exponentially to polynomially faster on a quantum computer. Here we will briefly discuss some of them:

1. **Grover's Search Algorithm**: Discovered by Lev Grover in 1996 (Grover, 1996), this search algorithm can find a single well-defined state in an unsorted database of size N in $\mathcal{O}(\mathcal{N})$ steps, being hence quadratically faster than a classical search algorithm.

2. **Shor's Factorization Algorithm** Discovered by Peter Shor in ???? (), this algorithm can factorize a binary number of length N into its prime factors in $\mathcal{O}(???)$ steps, therefore exponentially outperforming any known classical factorization algorithm. There is large interest in this algorithm since products of large prime numbers are routinely used in asymmetric cryptography.

2.2.4 Quantum Simulation

Another domain of interest for quantum computers is so called *quantum simulation*. Here the goal is to simulate the behaviour of an arbitrary quantum system using a quantum computer by either engineering the quantum computer in direct analogy with the system being modeled (so called *analog quantum simulation*) or by numerically simulating the Hamiltonian of the quantum system on a general-purpose quantum computer (so-called *digital quantum simulation*). Since no classical computer can simulate a quantum system efficiently, there is a large interest in quantum simulation, especially in the fields of biology and chemistry (e.g. for protein folding !3!)

To Do 3: include references!

2.2.5 Realization of a Quantum Computer

To realize a working quantum computer it is necessary to implement highly coherent qubits that can be manipulated, read out and coupled with high fidelity. So far, no fully working quantum computer has been experimentially demonstrated. However, larger progress towards the realization of such a quantum computer has been achieved in the last decade. Promising approaches for the realization of a quantum computer include –among others– ions trapped in magnetic and electric fields (), cold atomic gases (), photonic circuits (), semiconductor structures () and, last but not least, superconducting structures. Since this work treats only superconducting qubits of the Transmon type we will focus our attention on them in the following sections. We will explain how we can realize a reliable qubit using superconducting structures and how we can implement circuits to manipulate, couple and read out the qubit state.

2.3 Superconduting Quantum Circuits

In this section we will discuss several types of superconducting circuit elements that are most relevant to this work. We will introduce the reader to the Josephson junction, discuss the properties of transmission lines and tranmission line resonators and introduce a general method for the quantization of arbitrary circuits. Afterwards we will discuss the Cooper pair box and the Transmon qubit, give a short overview of circuit quantum electrodynamics and finally introduce the reader to the Josephson and cavity bifurcation amplifier.

2.3.1 The Josephson junction

The core element used to construct quantum circuits is the so-called *Josephson junction*, being equivalent to the transitor in classical circuits in significance. A Josephson junction is based on a disovery of Brian Josephson, which published a now-classical paper on quantum tunneling between weakly coupled superconductors (Josephson, 1962). He found, that such a *weak link* between two superconductors could support a supercurrent I described by the simple formula

$$I = I_c \sin \phi \tag{2.6}$$

where $\phi = \phi_2 - \phi$ and ϕ_1 and ϕ_2 are the superconducting phases at each side of the link. This simple equation, together with the current-phase relation of a Josephson junction,

$$U = \frac{\hbar}{2e} \frac{\partial \phi}{\partial t} \tag{2.7}$$

yields a system exhibiting a wealth of interesting physical phenomena that are used today in various applications in physics. The energy associated with the Josephson junction is given as

$$E = E_J (1 - \cos \phi) \tag{2.8}$$

where $E_J = I_c \Phi_0 / 2\pi$ is the so-called *Joesephson energy*. In addition to this Josephson energy, the junction usually has an energy associated to the capacitance formed by the two seperated electrodes of the junction and given as $E_c = Q^2/2C$.

For currents $I \ll I_c$, a Josephson junction behaves approximatively like a nonlinear inductor with inductance

$$L_J = \frac{\Phi_0}{2\pi I_c \cos \phi} \tag{2.9}$$

where $\Phi_0 = h/2e \approx 2.05 \times 10^{-15}\,\mathrm{Wb}$ is the so-called *magnetic flux quantum*. Later we will show how to make use of these properties of the Josephson junction to construct a

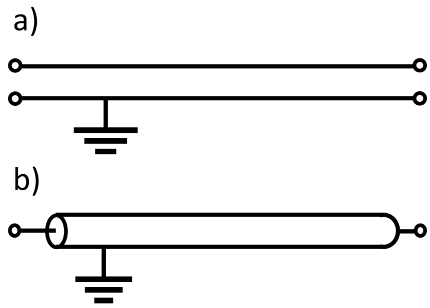

Figure 2.2: a) The circuit diagram of a grounded tranmission line. b) The circuit diagram of a grounded coaxial tranmission line.

qubit with it.

2.3.2 Transmission Lines

Another circuit element that we will encounter many times in this work is the so-called *transmission line*. In the most general way, a transmission line is a structure with a large extension in one direction which is capable of transmitting electromagnetic waves along itself. Two possible symbols by which one usually designates tranmission lines in a circuit schematic are shown in fig. 2.2. A detailed treatment of the physics of tranmission lines can be found e.g. Pozar (2011). For this introduction we will skip these basics and start directly with the equation that describes the propagation of an electromagnetic wave along the extended dimension z of the tranmission line and which is given as

$$V(z,t) = \exp(i\omega t) \cdot \Big(V^+ \exp(-i\gamma z) + V^- \exp(i\gamma z)\Big) \tag{2.10}$$

$$I(z,t) = \frac{1}{Z_0} \exp(i\omega t) \cdot \Big(V^+ \exp(-i\gamma z) - V^- \exp(i\gamma z)\Big) \tag{2.11}$$

Here, $\gamma = \alpha + i\beta = \sqrt{(R + i\omega L)(G + i\omega C)}$ is the so-called *propagation constant* which describes the dispersion and damping of electromagnetic waves along the transmission line and ω the circular frequency of the electromagnetic wave. The voltages V^+ and V^- correspond to waves traveling in different directions along the waveguide.

If we regard a CPW of fixed length l, we can model the voltages and currents at its end by using the formula(Pozar, 2011)

$$\begin{pmatrix} V_1 \\ I_1 \end{pmatrix} = \begin{pmatrix} \cos\gamma l & iZ_r \cos\gamma l \\ iY_r \sin\gamma l & \cos\gamma l \end{pmatrix} \cdot \begin{pmatrix} V_2 \\ I_2 \end{pmatrix} \tag{2.12}$$

2.3.3 Transmission Line Resonators

One can easily create a resonator using a coplanar waveguide as described in the last section. As an example, we will discuss an open-ended $\lambda/2$ CPW resonator that is used

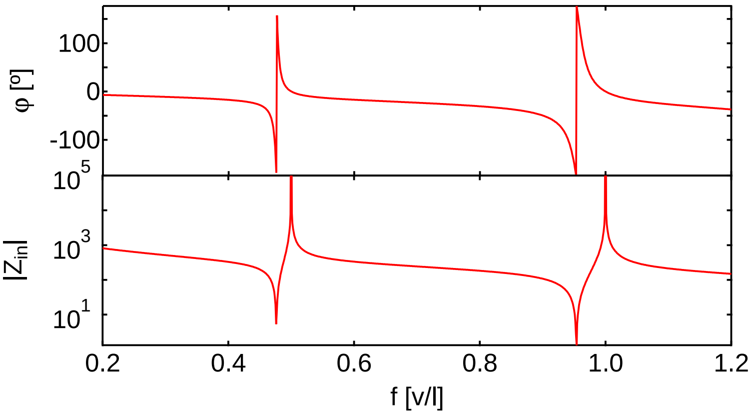

Figure 2.3: This is the side caption which is maybe already to small to support such long text..

in our experiments as well and thus highly relevant to this work. To create a resonator out of a CPW line, we terminate the line by an open and and connect it to a drive line through an input capacitance C. To calculate the voltages and currents going into the CPW resonator, we can use eq. (2.12). Since the far end of the resonator is open we demand that $I_2 =$ and thus obtain for the voltage V_1 and current I_2 the relation

$$V_1 = \cos\gamma l V_2 \tag{2.13}$$
$$I_1 = iY_r \sin\gamma l V_2 \tag{2.14}$$

Hence, the impedance of the resonator is given as $Z_{res} = V_1/I_1 = iZ_r \cot\gamma l$, where Z_r is the impedance of the tranmission line of which the resonator is made of. We couple this resonator to an input line through a gate capacitance C_g, thus the impendance seen from the input of the circuit is given as

$$Z_{in} = iZ_r \cot\gamma l - \frac{i}{\omega C_g} \tag{2.15}$$

It is straightforward to calculate the S_{11} reflection coefficient of the resonator when coupling it to an input line with impedance Z_0 as

$$S_{11} = \frac{Z_{in} - Z_0}{Z_{in} + Z_0} = \frac{Z_r \cot\gamma l - /\omega C_g - Z_0}{Z_r \cot\gamma l - /\omega C_g + Z_0} \tag{2.16}$$

Now, when measuring the reflection of an incoming signal with voltage V^+ at frequency $f = 2\pi\omega$ and phase ϕ_0, the phase of the relected signal ϕ_{ref} will be simply given as $\phi_{ref} = \mathrm{Arg}[V^-/V^+] - \phi_0 = \mathrm{Arg}[S_{11}] - \phi_0$. Fig 2.3 shows this phase for an exemplatory resonator, plotted for $f = 2\pi\omega$ in reduced units of $[l/v]$, with impendances $Z_r, Z_0 = 50\ \Omega$, $\alpha = 0$ and with the resonator coupled to the input line through a normalized capacitance $C_g = 10^{-3}/\omega\ [\mathrm{Hz}\cdot\mathrm{F}]$.

We can calculate the quality factor of such an open-ended CPW resonator by modeling it as a series-LC circuit. Indeed, if we regard the input impedance of the resonator in the vicinity of ω_0 such that $\Delta\omega = \omega - \omega_0$ with $\Delta\omega \ll \omega_0$ and $\beta l = \pi + \pi\Delta\omega/\omega_0$, we obtain an effective impedance

$$Z_{in} = \frac{Z_r}{\alpha l + i(\Delta\omega\pi/\omega_0)} \tag{2.17}$$

We can identify the quantities in this equation with the input impedance of a parallel LCR-resonator, which at $\omega \approx \omega_0$ is approximatively given as

$$Z_{in} = \frac{R}{1 + 2iQ\Delta\omega/\omega_0} \tag{2.18}$$

with $W = \omega_0 RC$. This yields an effective resistance, inductance and capacitance for the transmission line resonator of

$$R_r = \frac{Z_r}{\alpha l} \tag{2.19}$$

$$L_r = \frac{1}{\omega_0^2 C} \tag{2.20}$$

$$C_r = \frac{\pi}{2\omega_0 Z_r} \tag{2.21}$$

When coupling this resonator to an input transmission line of impedance Z_0 through a gate capacitance C_g as before, the quality factor of the coupled (or *loaded*) resonator will be given as (Göppl et al., 2008)

$$Q_L = \omega_0^* \frac{C + C^*}{1/R_r + 1/R^*} \tag{2.22}$$

where we have introduced an effective resistance, capacitance and resonance frequency given as

$$R^* = \frac{1 + \omega_0^2 C_g^2 Z_0^2}{\omega_0^2 C_g^2 Z_0} \tag{2.23}$$

$$C^* = \frac{C_g}{1 + \omega_0^2 C_g^2 Z_0^2} \tag{2.24}$$

$$\omega_0^* = \frac{1}{\sqrt{L_r(C_r + C_g)}} \tag{2.25}$$

Thus, we can effectively tune the quality factor of the resonator by changing the gate capacitance by which we couple it to the input tranmission line.

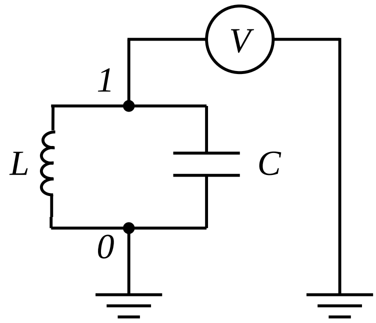

Figure 2.4: An exemplatory superconducing circuit made of a Josephson junction, a capacitor and a voltage source. The circuit topology can be described by one node (plus ground) and one branch.

2.3.4 Quantization of Electrical Circuits

In this section we will outline a general method to treat arbitary electrical circuits as the ones discussed before within the framework of quantum-mechanics, hence *quantizing* them. This introduction on circuit quantization presented in this chapter is based on an article by Devoret (1995).

Fig. 2.4 shows an exemplatory circuit made of an inductance, a capacitor and a voltage source. A circuit as this one is fully characterized by the parameters of its elements and its toplogy. The latter can be described – following the laws of Kirchhoff – as a set of nodes connected by a number of branches. In classical circuit theory, each branch i is described by a voltage V_i between its ends and a current I_i flowing through it. The Kirchhoff laws demand that the sum of the branch voltages V_i along any closed path must be zero, i.e. $\sum_{\oint} V_i = 0$. Equivalently one may demand that the sum of currents flowing in and out of each node must be zero. For the quantization of electrical circuits it is usually more convenient to replace voltages and currents with branch charges and fluxes that are defined as

$$\Phi_i(t) = \int_{-\infty}^{t} V_i(t')dt' \tag{2.26}$$

$$Q_i(t) = \int_{-\infty}^{t} I_i(t')dt' \tag{2.27}$$

In analogy with the Kirchhoff laws for the sums of currents and voltages along a closed branch, we can formulate a Kirchhoff law for the charges Q_i at each node of the circuit, given as

$$\sum_i Q_i = Q_0 \tag{2.28}$$

where Q_0 is constant . To quantize such a circuit made up of non-dissipative elements we can follow the method given in Yurke and Denker (1984), writing the Lagrangian of the circuit as

$$\mathcal{L} = \sum_i V_i - \sum_i T_i \tag{2.29}$$

where V_i and T_i are the potential and kinetic energies associated to each circuit element. !4! . For a circuit composed entirely of capacitors and inductor, this Lagrangian is given as

To Do 4: Clarify why kintetic energy is mapped to capacitive energy and potential energy to inductive energy

$$\mathcal{L} = \frac{1}{2}\sum_i \frac{Q_i^2}{C_i} - \frac{1}{2}\sum_i L\left(\frac{dQ_i}{dt}\right)^2 \tag{2.30}$$

If needed, resistors can be described within the Lagrangian formalism by modeling them as transmission lines with a characteristic impedance matching their resistance (Yurke and Denker, 1984). From the Lagrangian as given in eq. (2.30) we obtain then the equations of motion of the system by variation of the action

$$\frac{\partial}{\partial t}\left(\frac{\partial \mathcal{L}}{\partial(\partial_t Q_i)}\right) - \frac{\partial \mathcal{L}}{\partial Q_i} = 0 \tag{2.31}$$

Finally, by imposing the charge-conservation equations as given by eq. (2.28) we obtain then a complete description of the underlying circuit. From the variable Q_i we obtain the canonically conjugate momentum Φ_i by solving the equation

$$\Phi_i = \frac{\partial \mathcal{L}}{\partial(\partial_t Q_i)} \tag{2.32}$$

First Quantization of the circuit variables can then be done by imposing commutation relations between the set of canonical variables Q_i and Φ_i such that

$$[Q_i(t), Q_j(t')] = 0 \tag{2.33}$$

$$[\Phi_i(t), \Phi_j(t')] = 0 \tag{2.34}$$

$$[Q_i(t), \Phi_i(t')] = i\hbar\delta_{ij}\delta(t-t') \tag{2.35}$$

Having obtained Φ_i and Q_i, it is also trivial to obtain the Hamiltonian $\mathcal{H}$ of the system by applying the transformation

$$\mathcal{H} = \sum_j \Phi_i \dot{Q}_i - \mathcal{L} \tag{2.36}$$

In the next section we will use this method to quantize the Cooper pair box circuit.

2.3.5 The Cooper Pair Box

The *Cooper pair box (CPB)* is a device containing a (split) Josephson junction coupled to an input voltage source through a gate capacitance C_g, as shown in fig. 2.5. Following the circuit quantization method outlined in the last section, we obtain the following

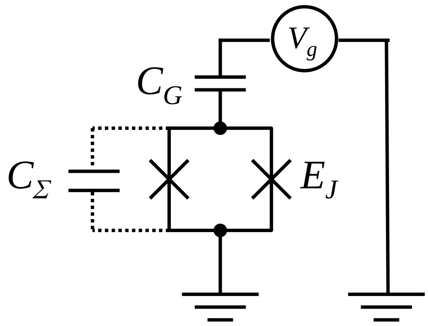

Figure 2.5: The circuit schematic of a Split Cooper Pair Box. The device consists of two Josephson junctions arranged in a loop, where the capacitance of the junctions is modeled as the extra capacitor indicated on the left. By putting the two junctions in series with a gate capacitance one creates an island one which charges can accumulate. The gate voltage can be controlled by an external voltage source.

Hamiltonian for the CPB (Cottet, 2002)

$$\hat{H} = 4E_C\left(\hat{n} - n_g\right)^2 - E_J \cos\hat{\theta} \tag{2.37}$$

Here we have defined $E_C = e^2/C_\Sigma$ as the charging energy of the system, with $C_\Sigma = C_J + C_B + C_g$ the total gate capacitance, $\hat{n} = \hat{Q}/2e$ the number of Cooper pairs transferred between the islands, $n_g = V_g C_g/2e$ the gate charge, E_J the Josephson energy of the junction and $\hat{\phi}$ the quantum phase across the junction.

$\hat{n}$ and θ are conjugate variables such that $[\theta, \hat{n}] = -i$, the corresponding wavefunction $\Psi_k(\theta) = \langle\theta, k\rangle$ will therefore satisfy a Schrödinger equation of the form

$$E_k\Psi_k(\theta) = E_C\left(\frac{1}{i}\frac{\partial}{\partial\theta} - n_g\right)^2\Psi_k(\theta) - E_J\cos(\theta)\Psi_k(\theta) \tag{2.38}$$

Since the potential $E_J\cos(\theta)$ is periodic, we may demand that the solution also possesses a periodicity of the form

$$\Psi_k(\theta) = \Psi_k(\theta + 2\pi) \tag{2.39}$$

Using this assumption it is possible to map eq. (2.38) to a simular and well-known differential equation, the so-called *Mathieu equation*, that is given as

$$\frac{d^2y}{dx^2} + \left[a - 2q\cos(2x)\right]y = 0 \tag{2.40}$$

The *Floquet theorem* states that all solutions to this equation can be written in the form

$$F(a, q, x) = \exp(i\mu x)P(a, q, x) \tag{2.41}$$

Using such a Floquet ansatz for eq. (**??**), the most general solutions that one obtains are given as (Cottet, 2002)

$$\Psi_k(r,q,\theta) = \mathcal{C}_1 \exp\left(in_g\theta\right)\mathcal{M}_C\left(\frac{4E_k}{E_C}, -\frac{2E_J}{E_C}, \frac{\theta}{2}\right) + \mathcal{C}_2 \exp\left(in_g\theta\right)\mathcal{M}_S\left(\frac{4E_k}{E_C}, -\frac{2E_J}{E_C}, \frac{\theta}{2}\right) \tag{2.42}$$

with

$$E_k = \frac{E_C}{4}\mathcal{M}_A\left(r_k, -\frac{2E_J}{E_C}\right) \tag{2.43}$$

Here, $\mathcal{M}_C$, $\mathcal{M}_S$ are the so-called *Mathieu functions* and $\mathcal{M}_A$ corresponds to the eigenvalue corresponding to each solution. Following the convention in (Cottet, 2002) we order the E_k such that the energy increases with increasing k, yielding

$$r_k = k + 1 - [(k+1)\mathrm{mod}2] + 2n_g(-1)^k \tag{2.44}$$

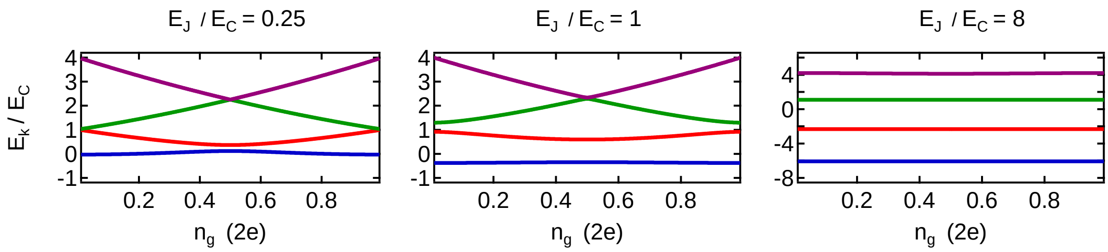

Figure 2.6: Energies of the first four energy level of the Cooper pair box for different ratios E_J/E_C, plotted as a function of the gate charge n_g. As can be seen, for $E_J \ll E_C$, the charge-dispersion curve becomes almost completely flat.

We denote the energy differences between individual energy level by $E_{ij} = E_j - E_i$. We also define the absolute and relative anharmonicities of the first two energy levels as $\alpha 12 \equiv E_{12} - E_{01}$ and $\alpha_r \equiv \alpha/E_{01}$. In the limit $E_J \gg E_C$ these anharmonicities are well approximated by $\alpha \simeq -E_C$ and $\alpha_r \simeq -(8E_J/E_C)^{-1/2}$. An in-depth treatment of the Cooper pair box can be found e.g. in (Cottet, 2002) !5! .

To Do 5: cite original paper by Zorin?

2.4 The Transmon Qubit

The Transmon qubit is a Cooper pair box operated in the regime where $E_J \gg E_C$. As shown above, in this regime the charge dispersion of the energy levels of the Cooper pair box becomes flat, thus rendering the transition frequency E_{01} almost insensitive to the value of the gate charge n_g. This reduced sensitivity to charge noise is highly advantageous in experiments. However, when increasing the ratio E_J/E_C, we also reduce the anharmonicity α_r of the qubit, therefore limiting the speed of gate operations that can be realized with this system (driving errors related to weak anharmonicity will be discussed more thoroughly in the Experiments section of this thesis). Remarkably

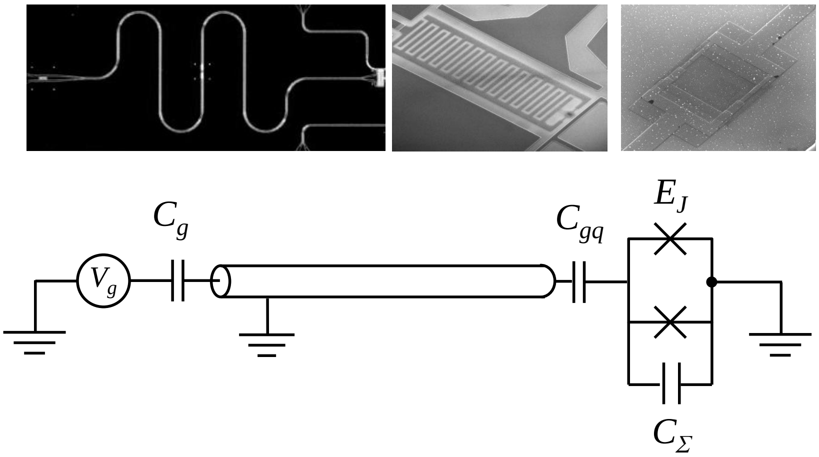

Figure 2.7: A typical circuit QED setup consisting of a Transmon qubit capacitively coupled to a $\lambda/2$ resonator.

though, α_r decreases only geometrically with E_J/E_C, whereas the sensitivity of the qubit to charge noise decreases exponentially with the ratio of Josephson and charging energy. Fig **??** shows the relaxation rate and relative anharmonicity of a Cooper Pair box for different values of E_J/E_C. As can be seen,

2.5 Circuit Quantum Electrodynamics

Cavity quantum electrodynamics is a research domain where one investigates the physics of an atom (or a large number of atoms) coupled to a high-Q microwave cavity. Analogously, *circuit quantum electrodynamics* investigates the coupling of an articial atom (e.g. a Transmon qubit) coupled to a microwave resonator that is realized on the surface of a chip. Usually, such a qubit-resonator system can be represented as in fig. 2.7. There, a Transmon qubit is capacitively coupled to a $\lambda/2$ resonator which itself is capacitively coupled to an input tranmission line. Due to the capacitance between the qubit and the resonator, a coupling energy of the form

$$E_{rq} = \frac{1}{2} C_g \hat{V}_g^2 = \frac{1}{2} C_g \left(V_{rms}^0 (a^\dagger + a) - \hat{V} \right)^2 \tag{2.45}$$

arises, where V_g is the voltage across the coupling capacitance C_g, $\hat{V} = 2e/C_\Sigma \cdot (n_g - \hat{n})$ is the voltage across the Transmon electrodes and $V_{rms}^0 = \sqrt{\hbar\omega_r/2C_r}$ is the root mean square voltage corresponding to one photon in the resonator. Hence the coupling energy can be rewritten as

$$\begin{aligned} E_{rq} &= \frac{1}{2} C_g \left(V_{rms}^0 (a^\dagger + a) - \frac{2e}{C_\Sigma} [n_g - \hat{n}] \right)^2 \\ &= 2e\beta V_{rms}^0 \hat{n} (a^\dagger + a) + \ldots \end{aligned} \tag{2.46}$$

where we defined $\beta = C_g/C_\Sigma$. The terms ommitted in eq. (2.46) correspond to energy shifts of the qubit and the resonator which are not directly relevant for the coupling between them. In the limit where the resonator capacity $C_r \gg C_\Sigma$ we can write the effective Hamiltonian of the system using the uncoupled basis states $|i\rangle$ as

$$\hat{H} = \hbar \sum_j \omega_j |j\rangle \langle j| + \hbar\omega_r \hat{a}^\dagger \hat{a} + \hbar \sum_{i,j} g_{ij} |i\rangle \langle j| (\hat{a} + \hat{a}^\dagger) \tag{2.47}$$

Here, $\omega_r = 1/\sqrt{L_r C_r}$ gives the resonator frequency of the resonator. The coupling energies g_{ij} are given as

$$\hbar g_{ij} = 2\beta e V^0_{rms} \langle i| \hat{n} |j\rangle = \hbar g^*_{ji} \tag{2.48}$$

When the coupling between the resonator and the Transmon is weak, such that $g_{ij} \ll \omega_r, E_{01}/h$ we can ignore the terms in eq. (2.47) that describe simultaneous excitation or deexcitation of the Transmon and the resonator and obtain the so-called *rotating wave approximation*, which is given as

$$\hat{H} = \hbar \sum_j \omega_j |j\rangle \langle j| + \hbar\omega_r \hat{a}^\dagger \hat{a} + \hbar \sum_i \Big(g_{i,i+1} |i\rangle \langle i+1| \hat{a}^\dagger + H.c. \Big) \tag{2.49}$$

This Hamiltonian describes a multi-level quantum system coupled to a resonator through a capacitive interaction. The first two terms correspond to the energies of the n-level system and the resonator, respectively. The term $|i\rangle \langle i+1| \hat{a}^\dagger$ describes the creation of a photon in the resonator accompanied by the deexcitation of the n-level system by one energy level.

2.5.1 Dispersive Limit & Qubit Readout

When the qubit frequency is far detuned from the resonator frequency such that $|\omega_{ij} - \omega_r| \gg g_{ij}$, direct qubit-resonator interactions are almost completely supressed and the only a dispersive shift of the transition frequency of both systems remains as an effect of the coupling between them. This effect has been discussed e.g. in Koch et al. (2007) and yields an effective Hamiltonian of the form

$$\hat{H}_{eff} = \frac{\hbar\omega'_{01}}{2} \hat{\sigma}_z + (\hbar\omega'_r + \hbar\chi\hat{\sigma}_z) \hat{a}^\dagger \hat{a} \tag{2.50}$$

Here, the resonance frequencies of the qubit and the resonator are shifted as $\omega'_{01} = \omega_{01} + \chi_{01}$ and $\omega'_r = \omega_r - \chi_{12}/2$ and the dispersive shift is given as $\chi = \chi_{01} - \chi_{12}/2$, where $\chi_{ij} = g^2_{ij}/(\omega_{ij} - \omega_r)$. As can be seen, for a state with n photons, the energy difference between the two qubit levels is given as

$$\omega_{01}^{n} = \omega_{01}' + 2\chi n \tag{2.51}$$

Thus, there is a dispersive shift of the qubit transition frequency that is proportional to the number of photons in the resonator. Likewise, the resonance frequency of the resonator gets also shifted by 2χ depending on the state of the qubit. The latter effect is very useful since it allows us to read out the state of the qubit by measuring the state-dependent frequency displacement of the resonator, as will be explained later.

2.5.2 Qubit-Qubit Interaction

In this section we will discuss possible qubit-qubit coupling schemes. We will regard a direct coupling scheme involving a capacitive coupling between two qubits and an indirect scheme involving the coupling of multiple qubits to a resonator which acts as a "quantum bus".

Coupling Bus

(Blais et al., 2007) showed that extending the single-qubit rotating-wave Hamiltonian as given in eq. (2.49) to the case of two qubits yields an effective qubit-qubit coupling Hamiltonian of the form

$$H_{2q} \quad = \quad \hbar\frac{g_1 g_2(\Delta_1 + \Delta_2)}{2\Delta_1\Delta_2}(\sigma_1^+\sigma_2^- + \sigma_1^-\sigma_2^+) \tag{2.52}$$

This approximation is valid in the limit of large qubit-resonator detuning where $\Delta_1 \gg g_1, \Delta_2 \gg g_2$. Here $\Delta_{1,2} = \omega_{01}^{1,2} - \omega_r$ is the detuning of the $|0\rangle \rightarrow |1\rangle$ transition frequency of each qubit to the bus resonator. Full energy-exchange between the qubits is achieved when the qubit frequencies are in resonance. By detuning the qubits from the resonator, the effective coupling constant can be varied, which is advantageous in many settings.

Direct Capacitive Coupling

A direct capacitive coupling C_{qq} between two qubits yields a coupling Hamiltonian of the form

$$\hat{H}_{qq} \quad = \quad \frac{1}{2}C_{qq}\hat{V}_{qq}^2 = \frac{1}{2}C_{qq}\left(\frac{2e}{C_{\Sigma 1}}(n_{g1} - \hat{n}_1) - \frac{2e}{C_{\Sigma 2}}(n_{g2} - \hat{n}_2)\right)^2 \tag{2.53}$$

$$\quad = \quad \frac{4e^2 C_{qq}}{C_{\Sigma 1}C_{\Sigma_2}}\hat{n}_1\hat{n}_2 + \ldots \tag{2.54}$$

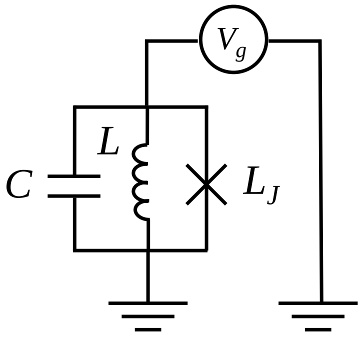

Figure 2.8: The circuit model of the JBA.

This equation is valid in the limit where $C_{qq} \ll C_{\Sigma 1}, C_{\Sigma 2}$, otherwise the coupling gets renormalized by a factor $\alpha = 1/(1 - C_{qq}^2/[C_{\Sigma 1} C_{\Sigma 2}])$ (**?**). Rewriting it in the basis of uncoupled qubit states yields the effective Hamiltonian

$$\hat{H}_{qq} = \hbar 2 g_{qq} \left(\sigma_1^+ \sigma_2^- + \sigma_1^- \sigma_2^+ \right) \tag{2.55}$$

where we have defined the effective qubit-qubit coupling as $\hbar g_{qq} = 2e^2 C_{qq}/C_{\Sigma 1} C_{\Sigma 2}$. As before, full energy exchange between the qubits is achieved when the qubit frequencies are in resonance. Directly coupling two qubits can be advantageous since it simplifies the circuit layout and does not require an auxiliary quantum system. However, since the coupling is always turned on it is difficult to achieve a sufficiently good ON/OFF ratio that is needed for many applications (e.g. to realize a quantum gate).

2.6 The Josephson Bifurcation Amplifier

In this section we will briefly discuss the physics of superconducting nonlinear bifurcation amplifiers. The two devices that we will discuss are the so-called *Josephson bifurcation amplifier (JBA)* as shown in fig. 2.8 and the so-called *cavity bifurcation amplifier (CBA)* as shown in fig. 2.9. The JBA typically consists of a Josephson junction in parallel with a capacitor and (optionally) an inductor. The CBA, on the other hand, consists of a tranmission line resonator with a Josephson junction embedded in its central conductor. As shown in one of the last sections, a transmission line resonator can be treated mathematically as a lumped elements resonator, hence the physics of the CBA can be mapped to that of the JBA. Hence we will restrict our discussion in this section to the JBA. A more detailed comparision between the JBA and CBA can be found e.g. in Palacios-Laloy (2010).

The circuit in fig. 2.8 can be modeled as

$$[L_e + L_J(i)]\ddot{q} + R_e \dot{q} + \frac{q}{C_e} = V_e \cos(\omega_m t) \tag{2.56}$$

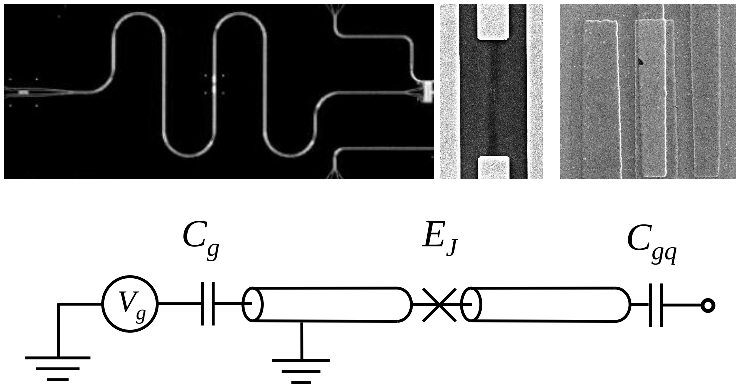

Figure 2.9: The Cavity Bifurcation Amplifier used in this work.

Here, L_J the Josephson inductance as given by eq. (2.9) and L_e, C_e and R_e are the resistance, inductance and capacitance parallel to the Josephson junction in the circuit. V_e is the amplitude of the driving voltage, which oscillates at a frequency ω_m. Expanding the Josephson inductance in this equation to second order leads to the equation

$$\left(L_e + L_J\left[1+\frac{\dot{q}^2}{2I_0^2}\right]\right)\ddot{q} + R_e\dot{q} + \frac{q}{C_e} = V_e\cos\left(\omega_m t\right) \tag{2.57}$$

Defining the total inductance $L_t = L_e + L_J$, the participation ratio $p = L_J/L_t$, the resonance frequency $\omega_r = 1/\sqrt{L_t C_e}$ and the quality factor $Q = \omega_r L_t/R_e$ we can rewrite this as

$$\ddot{q} + \frac{\omega_r}{Q}\dot{q} + \omega_r^2 q + \frac{p\dot{q}^2\ddot{q}}{2I_0} = \frac{V_e}{L_t}\cos\left(\omega_m t\right) \tag{2.58}$$

Introducing the reduced variables $\beta = (V_e/\phi_0\omega_m)^2(pQ/2\Omega)^3$, $\Delta_m = \omega_r - \omega_m$, $\tau = t\Delta_m$, $\Omega = 2Q\Delta_m/\omega_r$ and $u(t) = \sqrt{pQ/2\Omega}\cdot q(t)\omega_m/I_0$ we can further rewrite this equation to obtain

$$\begin{aligned}&\frac{\Delta_m}{\omega_m}\frac{d^2u}{d\tau^2} + \left(\frac{1}{Q\omega_m} + 2i\right)\frac{du}{d\tau}\\ &+\left[2\left(\frac{\omega_r^2-\omega_m^2}{2\omega_m\Delta_m}\right) + \frac{1}{Q\Delta m} - 2|u|^2\right]u = 2\sqrt{\beta}\end{aligned} \tag{2.59}$$

In the limit where $Q \gg 1$, $\Delta_m\omega_m \ll 1$ such that $\omega_m + \omega_r \approx 2\omega_m$ and $\ddot{u} \ll \omega_m\dot{u}$ we can simplify this equation to obtain

$$\frac{du}{d\tau} = -\frac{u}{\Omega} - iu\left(|u|^2 - 1\right) - i\sqrt{\beta} \tag{2.60}$$

The stationary solutions of this equation describe stable oscillator states and have the form

$$\frac{|u|^2}{\Omega^2} + |u|^2\left(|u|^2-1\right)^2 = \beta(\Omega) \tag{2.61}$$

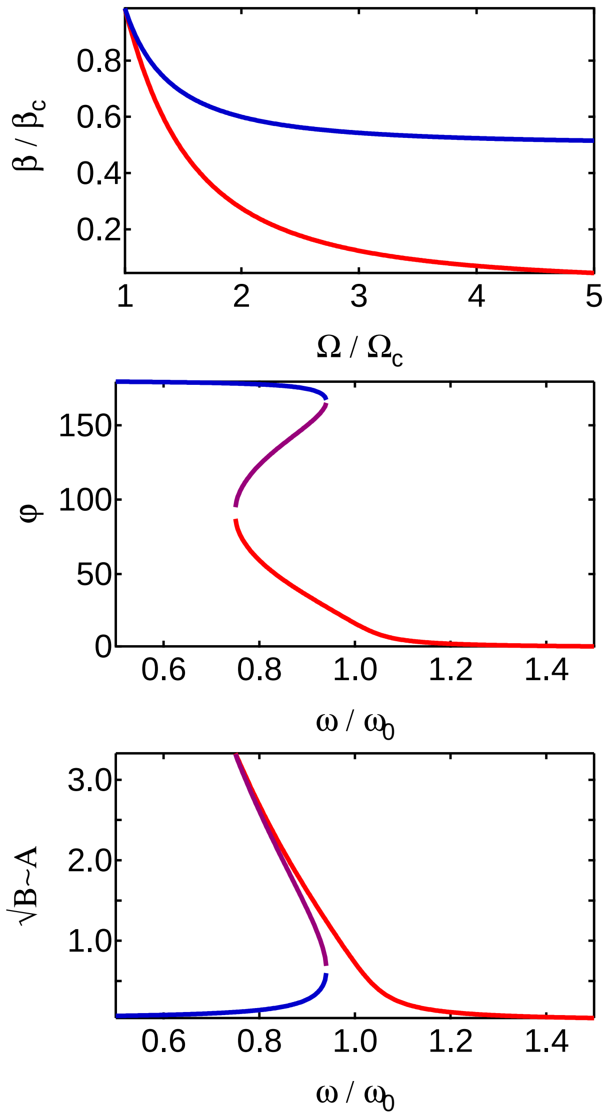

Figure 2.10: a)The bistability boundaries $\beta^{\pm}$ of a JBA, plotted as a function of Ω/Ω_c. b/c)The phase $\phi = \arg(u(t))$ and amplitude $A \simeq |u(t)|$ of different solutions of eq. (2.60) for the JBA parameters $\alpha = 0.05$ and $\gamma = 0.01$. In the hysteretic region, three solutions exists, two of which are stable. The solution realized at a given moment depends thus on the history of the system, allowing for hysteretic behaviour.

This equation can have one or two physical solutions depending on the parameter $\beta(\Omega)$. The region where multiple solutions exist is usually called the *bistability region* and is limited by the the two parameter boundaries $\beta^{\pm}(\Omega)$ that are given as

$$\beta^{\pm}(\Omega) = \frac{2}{27}\left[1 + \left(\frac{3}{\Omega}\right)^2 \pm \left(1 - \frac{3}{\Omega^2}\right)^{3/2}\right] \tag{2.62}$$

Fig. 2.10 shows the values of $\beta^{\pm}(\Omega)$ as well as the phase $\phi \simeq \arg(u(t))$ and the amplitude $\sqrt{B} \propto A \simeq |u(t)|$ of different stable solutions of eq. (2.60) for a JBA with $\alpha = 0.05$ and $\gamma = 0.01$, where $\alpha = V_e p^{3/2}/\phi_0\omega_r$ and $\gamma = R_e/L_t\omega_r$ characterize the drive strength and dissipation in the JBA, respectively.

Chapter 3

Realizing a Two-Qubit Processor

This chapter discusses in depth the design process for the realization of the 2-qubit processor which was used in this work. We will start by introducing the general constraints we face when designing a two-qubit processor, followed by a component-wise discussion of the individual parts of the processor and the associated parameters we need to choose.

3.1 Introduction & Motivation

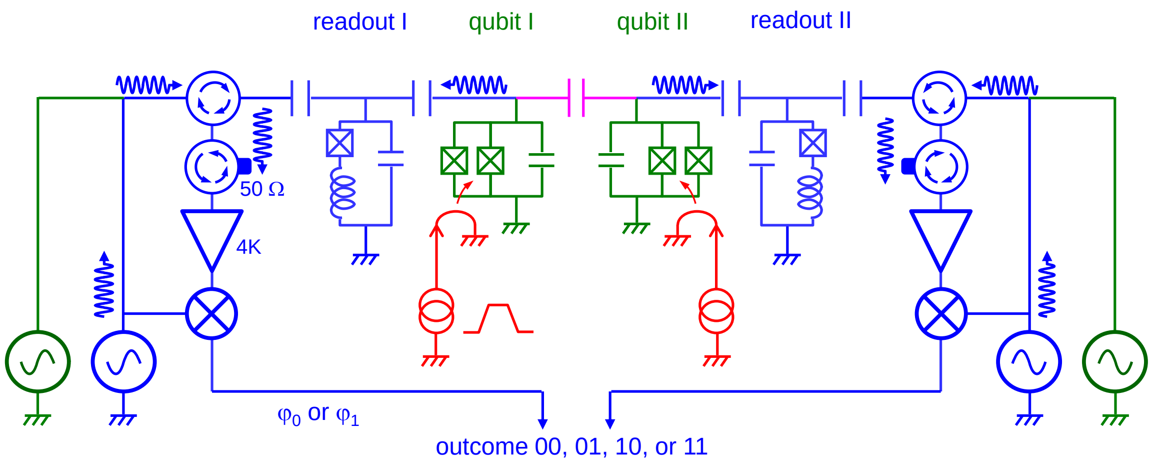

Figure 3.1: The circuit schematic of the two-qubit processor used in this work. Shown are the two Transmon qubits in green, the drive and readout circuit in blue, the fast flux lines in red and the coupling capacitance in magenta.

As discussed in the introduction, the most simple, usable quantum processor contains two qubits that can be manipulated and read out individually and between which one can realize a universal 2-qubit gate. We implement such a two-qubit processor using two Transmon qubits that are coupled by a fixed capacitance and that can be read out out individually by a pair of Josephson bifurcation amplifiers (JBAs). The circuit diagram of our processor is shown in fig. 3.1, it shows the two qubits in green, the drive and readout circuit in red, the coupling capacitance between them in magenta and the fast flux lines in read. Also shown is the basic microwave setup used for manipulating and reading out the qubits. In the following sections we will discuss each of these components and the parameters we have chosen for them individually.

3.2 Qubit Design

For the qubits, the main design goal is high coherence time, good frequency tunability and the possibility of fast qubit driving. The coherence time of the qubits is limited by relaxation to the ground state and dephasing due to coupling to external noise sources. The dephasing of the qubit state is caused mainly by noise-induced fluctuations of the qubit frequency, which we will discuss in the next section. The relaxation is caused mainly by the coupling of the Transmon to its environment and by internal losses inside the Josephson junctions and the capacitor of the qubit.

Frequency tunability is important since it will allow us to implement two-qubit gates and to position the qubit ideally for readout or manipulation, as will be explained later. However, strongly coupling the qubit to a fast flux line can induce relaxation and dephasing as well. In the following sections we discuss therefore which coupling strength is adequate and how much the flux coupling contributes to the decoherence time of the qubit.

The drive speed of the qubit –i.e. the frequency at which we can drive qubit transitions– is ultimately limited by its anharmonicity. When the drive frequency becomes comparable to the anharmonicity we start to induce transitions to higher Transmon levels, therefore "leaking" out of the computational basis and producing unitary errors. As we will see, the anharmonicity of the Transmon cannot be chosen arbitarily high since the sensitivity of the Transmon to charge noise increases exponentially with its anharmonicity, it is therefore necessary to find a compromise.

We will start our discussion of the qubit design by discussing the choice of the following qubit parameters:

1. The maximum qubit transition frequency f_{01}
2. The qubit anharmonicity α
3. The qubit critical current asymmetry d
4. The size of the qubit flux loop and its coupling to the fast flux line

3.2.1 Qubit Transition Frequency and Anharmonicity

The maximum transition frequency $f_{01}^0 = \sqrt{E_J E_C/2}/h$!6! of the qubit should be chosen in function of the readout resonator frequency such that it is possible to tune the two of them sufficiently close, thereby achieving the optimal readout fidelity. Chosing a qubit frequency above the cavity frequency should therefore be avoided, since it implies a stronger flux dependence of the qubit frequency at frequencies below the resonator frequency, thus increasing qubit dephasing when operating the qubit there. Hence, ideally the maximum qubit frequency should be chosen such that it corresponds to the optimal frequency for the qubit readout, as will be discussed later.

To Do 6: verify constants!

The anharmonicity $\alpha_r = -(8E_J/E_C)^{-1/2}$ of the qubit can be tuned by changing the ratio of charging and Josephson energy E_J/E_C. In general, one aims to have as much anharmonicity as possible in order to avoid inducing leakage to higher level of the quantum system when driving the qubit at high transition frequencies. On the other hand, increasing the anharmonicity (and thus decreasing E_J/E_C) will also lead to more charge-induced dephasing of the qubit, thus limiting the coherence time. For our setup, we chose an anharmonicity of the order of -240 MHz which allows us to perform single qubit gates at ≈ 100 MHz transition frequency without inducing too much leakage to the higher qubit states (a detailed analysis of this leakage will be given in the main section of this thesis).

Given f_{01}^0 and α_r (or equivalently α), we can calculate the required charging and Josephson energies of our qubit easily as

$$E_C = -\alpha \tag{3.1}$$

$$E_J = \frac{(4\pi\hbar f_{01}^0)^2}{|\alpha|} \tag{3.2}$$

For our processor, we chose values $f_{01}^0 = 7.0$ GHz and $\alpha = -240$ MHz, respectively, which yields a Josephson energy $E_J =$ and a charging energy $E_C =$.

We can estimate the dpehasing time of the qubit as a function of these energies by using an equation given in Koch et al. (2007):

$$T_2 \simeq \frac{\hbar}{A} \left| \frac{\partial E_{01}}{\partial n_g} \right|^{-1} \simeq \frac{\hbar}{A\pi|\epsilon_1|} \tag{3.3}$$

where A is an empirical parameter and ϵ_m depends exponentially on E_J/E_C and is given as

$$\epsilon_m \simeq (-1)^m E_C \frac{2^{4m+5}}{m!} \sqrt{\frac{2}{\pi}} \left(\frac{E_J}{2E_C} \right)^{m/2+3/4} e^{-\sqrt{8E_J/E_C}} \tag{3.4}$$

The dephasing time of the qubit is thus increasing exponentially with the ratio E_J/E_C if

Figure 3.2: Image of the fast flux line used in our 2-qubit processor. The fluxline is separated from the qubit SQUID loop through a stretch of ground plane, the seperation between the fluxline and the qubit is $\approx 20\ \mu\mathrm{m}$. The flux coupling coefficient is given as $1\Phi_0/20\ \mathrm{mA}$.

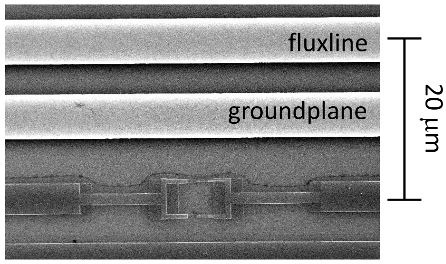

$E_J \gg E_C$, whereas the anharmonicity decreases only geometrically with E_J/E_C. For our values of E_J and E_C and for a value $A =$, we obtain a dephasing time $T_2 =$.

3.2.2 Qubit Critical Current Asymmetry

The critical current asymmetry of the qubit SQUID determines the modulation depth of the transition frequency as a function of the flux applied to the SQUID loop. The interest of choosing a non-zero d (and thus a reduced frequency modulation depth) is to reduce the flux-induced dephasing of the qubit state, which is given as (Koch et al., 2007)

$$T_2 = \frac{\hbar}{A}\left|\frac{\partial E_{01}}{\partial \Phi}\right|^{-1} \tag{3.5}$$

where A is an emperical parameter. Hence, the coherence rate increases proportional to the derivative of the qubit energy as a function of the applied flux. On the other hand, cricital current asymmetries can open additional relaxation channels () such that the overall effect of increasing d is not necessarily monotonous. For our qubits, we chose values of the asymmetry of $d_I = 0.2$ and $d_{II} = 0.35$. However, as we will show later this choice did not led to increased dephasing times of the qubits and should generally be avoided. !7!

To Do 7: cite relevant sections of the Koch paper!

3.2.3 Coupling of the Qubit to the Fast Flux Line

Another critical parameter to chose is the coupling of the qubit the fast flux line. This coupling must be sufficiently strong to allow large frequency displacements of the qubit during operation of the processor but not so strong as to induce additional qubit relaxation or dephasing. A comprehensive summary of fluxline-induced dephasing and relaxation mechanism can be found in Koch et al. (2007). For our qubit chip, we chose a geometry as depicted in fig. 3.2. Here, the distance between the qubit SQUID loop and the flux line is approx. $20\ \mu\mathrm{m}$, thus the flux coupling to the qubit is given as approx. $1\Phi_0/20\ \mathrm{mA}$. The capacitive coupling between the qubit electrodes and the fluxline is $C_{qf}\ =??\ \mathrm{fF}$. This capacitive coupling yields an additional contribution to the qubit relaxation rate of the order of $\Gamma_{qf} \approx$. !8! .

To Do 8: add more info on the relevant relaxation

3.2.4 Qubit-Qubit Coupling

To realize universal two-qubit gate operations it is necessary to provide a kind of coupling between the two qubits of our processor. As discussed before, we use direct capacitive coupling to achieve this for our processor. The coupling strength g_{qq} between the two qubits can be calculated by using eq. (2.54). This coupling strength must be chosen such that the interaction between the qubits is sufficiently fast to realize two-qubit gate operations with adequate fidelity but not too strong in order to still allow us to controllably switch on and off the coupling by detuning the qubit frequencies. In general, by diagonalizing the Hamiltonian given in eq. (2.55) we find for the swapping frequency f_{qq} and the swap amplitude a_{qq} of the two coupled qubits as a function of the qubit-qubit detuning $\Delta = f_{01}^{I} - f_{01}^{II}$ the values

$$\begin{aligned} f_{qq} &= \frac{1}{2}\sqrt{16g^2 + \Delta^2} \\ a_{qq} &= \frac{4g}{\sqrt{16g^2 + \Delta^2}} \end{aligned} \tag{3.6}$$

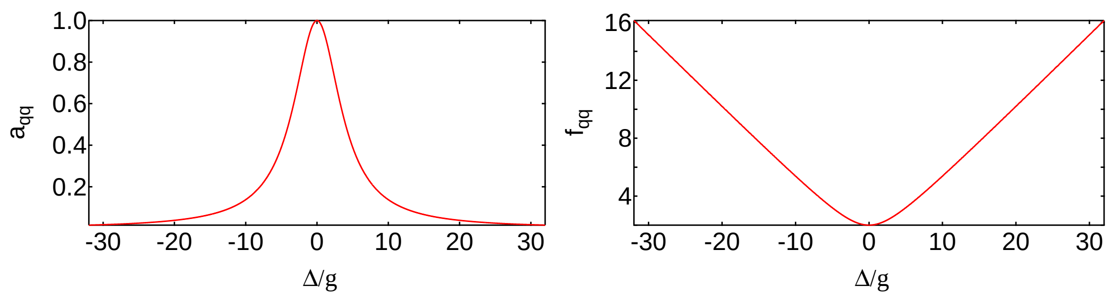

Figure 3.3: The swapping amplitude a_{qq} and frequency f_{qq} as given by eq. (3.6). For $\Delta \gg g$, the amplitude of the swap decreases $\propto 1/\Delta$ and the frequency increases $\propto \Delta$. To effectively switch of the qubit-qubit level below the 1 % error level, a detuning of $\Delta \approx 40g$ is required.

Fig. 3.3 shows this amplitude and frequency as a function of the normalized qubit-qubit detuning Δ/g. As can be seen, for $\Delta \gg g$ the swap amplitude decreases $\propto 1/\Delta$ whereas the swap frequency increases $\propto \Delta$. To turn off the qubit-qubit coupling below the 1 % level it is necessary to detune the qubits by $\Delta \approx 40g$. It is therefore important to choose g such that it is possible to tune the qubits in and out of resonance sufficiently fast in order to realize a reliable two-qubit gate and switch of the qubit-qubit interaction if wanted. For our processor, we chose $2g = 10$ MHz, hence we need to detune the qubits by only 200 MHz to switch off the coupling between them, which is easily achievable using our fast flux lines. In resonance, the swap frequency of 100 MHz allows us to realize an $\sqrt{i\mathrm{SWAP}}$ gate in $25\ \mathrm{ns}$ and an $i\mathrm{SWAP}$ gate in $50\ \mathrm{ns}$, which is sufficiently fast compared to the estimated relaxation and dephasing times of the qubits.

3.3 Readout Design

In the following section we discuss the design of the qubit readout. The main parameters that we need to choose for the readout are

1. The frequency ω_r, quality factor Q and nonlinearity K of the readout resonator
2. The coupling g_{qr} between the qubit and the readout resonator

The frequency f_r of the resonator is chosen high enough to have a negligibly low thermal photon occupation probability at the operating temperature $T = 20\ \mathrm{mK}$ of our experiment. Also, the choice of frequency is limited by the availability of sufficiently good cryogenic microwave components (especially circulators) in the chosen frequency band. For our qubit processor, we chose resonator frequencies of $f_r^I = 6.7\ \mathrm{GHz}$ and $f_r^{II} = 7.85\ \mathrm{GHz}$. The resonance frequencies of the two resonators are detuned by $150\ \mathrm{MHz}$ in order to reduce the effect of unwanted microwave crosstalk between them.

The other relevant parameters of the readout resonator are its quality factor Q and its Kerr constant K. The choice of the quality factor influences the relaxation rate of the qubit through the Purcell effect as well as the rate at which photons can be created in or extracted from the resonator, which in turn also determines the speed of the qubit readout. A comprehensive review of the interplay between qubit relaxation, readout speed and readout fidelity can be found in Mallet et al. (2009). To quantify the Purcell relaxation of the qubit trough the readout resonator we can use an equation given in (Koch et al., 2007):

$$\gamma_k^{(i,i+1)} = \kappa \frac{g_{i,i+1}^2}{(\omega_{i,i+1} - \omega_r)^2} \tag{3.7}$$

Here, ω_r is the frequency of the readout resonator, $\omega_{i,i+1}$ is the $|i\rangle \rightarrow |i+1\rangle$ transition frequency of the Transmon and $g_{i,i+1}$ is the qubit-resonator coupling strength for this transition. As can be seen, the Purcell relaxation rate decreases quadratically with the qubit-resonator detuning and increases quadratically with the qubit-resonator coupling strength $g_{i,i+1}$!9! . For our resonators, we chose $Q = 800$ which yields $\kappa_I = 52.6\ \mathrm{MHz}$ and $\kappa_{II} = 53.8\ \mathrm{MHz}$. Thus, for the above quality factors, a qubit-resonator coupling $2g_{qr}^{01} = 2\pi \cdot 50\ \mathrm{MHz}$ and a detuning of $\omega_{01} - \omega_r = 2\pi \cdot 500\ \mathrm{MHz}$ we obtain a Purcell relaxation time of $T_1^{01} \approx 7.5\ \mu\mathrm{s}$, which is bigger than the intrinsic relaxation time of a typical Transmon qubit by a large factor (however, certain new types of Transmon qubits can surpass this relaxation time).

To Do 9: choose consistent notation, e.g. $g_{qr}^{i,i+1}$!

The choice of the Kerr nonlinearity K determines the number of photons in the low- and high-amplitude oscillation state of the resonator and the size of the "bifurcation region" of the JBA. It is important to choose K sufficiently high in order to be able to achieve reliable readout operation. On the other hand, the photons present in the resonator during the readout can induce decoherence in the qubit and will shift its resonance frequency proportional to the number of photons. This frequency shift can create unwanted effects such as recoupling of the two qubits of our processor and should therefore be minimized. Theoretically, the maximum readout fidelity is achieved when the bifurcation point of the resonator is shifted by more than its linewidth, as a function of the qubit state. The linewidth of the switching probability distribution of the JBA as a function of the incident microwave power can be calculated numerically but usually we use experimental values to characterize it. In our case, this measured linewidth in dB was given as $\Delta p = xx$ dB. !10!

To Do 10: add more detail about the readout contrast at a given detuning for the chosen set of parameters.

3.4 Processor Fabrication

We fabricate the processor on a silicon substrate with a 50 nm thermal oxide layer. First, we depose a 150 nm layer of Niobium by magentron sputtering. Afterwards, we spin a photoresist and define an etch mask through optical lithography. Then we dry-etch in aSF_6 plasma, defining the readout resonators, tranmission lines and qubit flux lines on the chip. This optical patterning is performed for the wafer as a whole. Afterwards, we spin a bilayer of MAA/PMMA electron beam resist (with typically 1050 nm of MMA and 115 nm of PMMA thickness). Then the wafer gets diced and the qubits and JBA junctions are patterned per chip using electron beam lithography, using a double-angle shadow evaporation technique to define the Josephson junctions and capacitances on the chip. The e-beam resist is then lifted off chemically in an Acetone bath. We characterize the chip optically afterwards. In addition, we place "twin" structures of the Transmon qubits and the JBAs on each chip whose normal state resistance we measure at room temperature. Giving the normal-state resistance of a Josephson junction we can calculate the Josephson energy by using the Ambegaokar-Baratoff relation

$$E_J = \frac{2\pi^2\Delta}{R_n h} \tag{3.8}$$

,where $E_J = hI_c/4\pi e$. Furthermore, we perform numerical microwave simulations to extract the values of all relevant capacitances and inductances on the chip, which allows us to calculate all relevant parameters of our qubit chip.

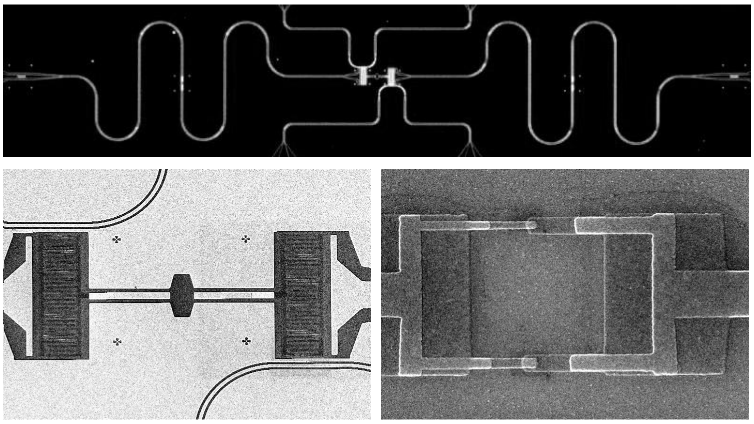

Figure 3.4: Optical and electron microscope photos of the two-qubit processor realized in this work. a) shows the full processor with the two coupled qubits, fluxlines and readout resonator. b) shows an enlarged version of the central region of the chip with the two qubits and the coupling capacitance. c) Shows a single Transmon qubit.

Chapter 4

Measurement Setup & Techniques

In this chapter we will discuss the measurement setup and techniques that we use in our experiments. We will discuss all individual parts of our signal generation and measurement chain, putting emphasis on the generation and measurement of high-frequency signals. Afterwards we will briefly discuss the calibration and compensation techniques that we use to correct signal imperfections.

Finally we will introduce the reader to the different measurement techniques that we use in this work, including techniques used for qubit readout and driving as well as more advanced measurement methods that we use to characterize the qubits and their decoherence times.

4.1 Sample Holder & PCB

The qubit chip is first glued to a high-frequency PCB. The coplanar transmission lines present on the chip are bond-wired to their counterparts on the microwave PCB, where they are terminated by a set of Mini-SMA !2! connectors. Additional bond wires are used to connect ground planes of the chip to the PCB. Also, bond wires are used to connect different parts of the on-chip ground plane that are isolated from each other due to the circuit topology. As Schuster (2007) showed, non-connected on-chip ground planes can induce parasitic resonances on the qubit chip and should therefore be avoided. The mounted chip on the PCB is then placed in a Copper or Aluminium sample holder that fully encloses the PCB and provides electromagnetic shielding of the environment. The inner dimensions of the sample holder are chosen such that no spurious box resonances in the frequency range relevant to our experiment can arise.

Comment 2: SMP???

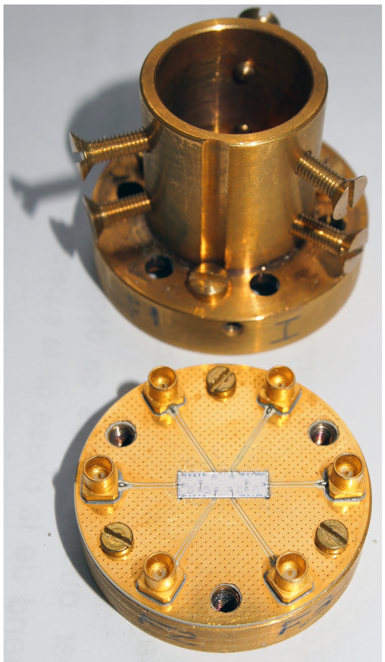

Figure 4.1: The sample holder with the mounted PCB carrying the qubit chip. Bond wires are used to connect the on-chip tranmission lines to the PCB, which in turn uses a Mini-SMP connector to connect the bond-wire to a set of external coaxial SMP cables. The top part of the sample holder is screwed to the bottom part, forming a closed box with cavities only for the tranmission lines and the qubit chip. The whole sample holder is screwed to the 20 mK stage of the dilution cryostat.

4.2 Cryogenic Wiring

Microwave signals that are generated at room temperature are sent to the qubit chip through a series of transmission lines. Fig. 4.2 shows the wiring of our experiment from room temperature down to the 20 mK state of the dilution cryostat. Superconducting cables are used where adequate to minimize signal attenuation, in addition lossy cables made from special compounds (e.g. CuNi) are used to minimize heat transfer into the dilution cryostat, which is especially critical between the 4K and 300 mK and the 300 mK and 20 mK states of the cryostat. In addition to high frequency transmission lines we also use a pair of bifilar cables to power a superconducting Nb coil which is used for flux biasing the qubits.

4.3 Signal Generation & Acquisition

For the experiments prsented below we need to generate pulsed high-frequency signals with a well-defined frequency, amplitude and phase. In addition we need to characterize microwave signals measured using microwave reflectometry using standard microwave demodulation techniques. In the following sections we discuss in detail the signal generation and measurement chain used for our experiments.

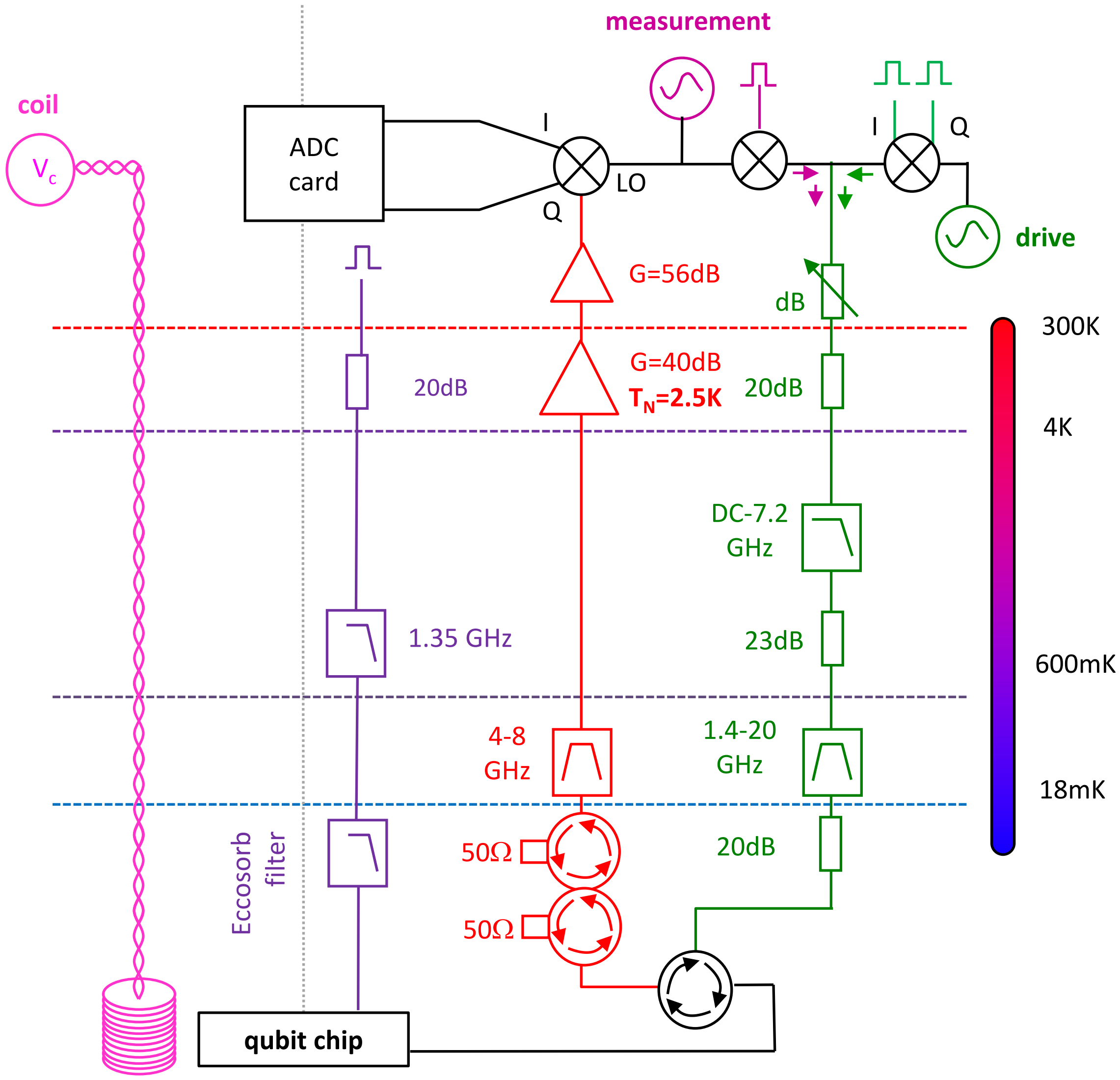

Figure 4.2: The measurement setup used for the two-qubit experiments. Exactly the same drive and readout scheme is used for both qubits with phase-locked microwave sources and arbitrary waveform generators.

4.3.1 Driving and Measurement of the Qubit

Each of the qubits together with the corresponding readout resonator on our chip is fitted with an individual drive and readout circuit. At room temperature we generate qubit and resonator drive waveforms using phase-locked single-tone microwave sources whose continous output is mixed with fast control pulses generated by two arbitrary waveform generators (the details of this microwave mixing will be discussed in the following paragraph). The drive and readout signals are then combined and sent to the qubit chip through a series of (cryogenic) attenuators and filters. A cryogenic circulator at the 20 mK sample stage of the dilution cryostat routes the incoming pulses to the qubit chip where they are sent to the qubit readout resonator and finally reflected by it. The reflected signal passes again through the input microwave circulator and gets routed through a double isolator and a band-pass filter to a cryogenic HEMT amplifier with a gain of 40 dB. The amplified signal gets transmissted to the room temperature electronics, where it gets filtered and amplified further. Finally, the signal is demodulated with a continous microwave reference tone and fed to an ADC board through a pair of low-noise amplifiers.

In addition to this, each qubit is equipped with a pair of fast flux lines. High-frequency and DC flux pulses are generated using an arbitrary waveform generator at room temperature. The flux signal is then sent to the qubit chip through 20 dB of attenuation, a conventional Microtronics low-pass filter as well as a custom-made high-frequency powder filter that uses an absorptive material (Eccosorb) to attenuate high-frequency noise. After passing through the transmission line on the qubit chip, the outgoing flux signal gets routed to room temperature through a tranmission line identical to the input line. There, the signal can be measured, which is useful for correcting possible signal imperfections caused by the non-ideal character of the tranmsission line (we will detail in one of the following sections how to numerically compensate the imperfect frequency response of the flux line).

4.3.2 Microwave Sideband Mixing

To Do 11: Add exact type number

To generate the qubit drive pulses we use single-sideband mixing techniques. We use a pair of IQ mixers (Hittite !11!) that we drive with a continous single-frequency microwave tone and two synchronized fast control signals generated by an arbitrary waveform generator (Tektronix AWG5014b). In general, when feeding a signal $LO(t) = i_0 \cos(\omega_{rf} t)$ to the LO port of an IQ mixer and two signals $I(t)$, $Q(t)$ to the I and Q ports of the mixer, we obtain a signal

$$RF(t) = I(t)\cos(\omega_{rf} t) + Q(t)\sin(\omega_{rf} t) \tag{4.1}$$

at the RF port of the mixer. Since the IQ mixer that we use is a passive, reciprocal device one can as well feed two input signals to the LO and RF ports and obtain the demodulated signal quadratures at the I and Q ports, a technique that we make use in our qubit readout scheme, as will be detailed later in this chapter.

Typically we use sideband mixing to generate drive pulses that are displaced in frequency in respect to the original LO (carrier) waveform. This if often advantageous since it eliminates microwave leakage at the signal frequency for zero voltage on the IQ inputs, which is often a big problem for commercially available IQ mixer, as we will discuss below.

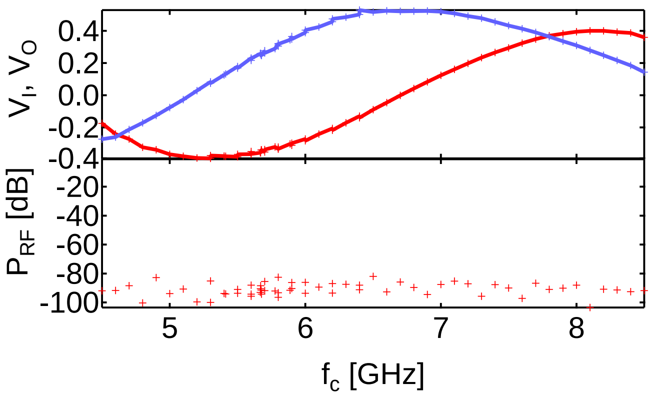

Figure 4.3: a) The offset voltages that we need to apply to the IQ ports of the mixer to eliminate unwanted leakage from the LO to the RF port of the device, plotted as a function of the carrier frequency f_c. b)The measured remaining signal power at the RF port of the mixer at the optimal IQ bias point.

Commercially available IQ mixers often deviate from the ideal behavior as given by eq. (4.1). Typical imperfections include large insertion losses –i.e. loss of signal power between the different ports of the mixer–, RF signal leakage at zero IQ-input and frequency-dependent phase and amplitude errors of the mixed sideband signals. In order to achieve reliable single-qubit operations we need to correct the signal leakage and quadrature-specific amplitude and phase errors. The signal leakage causes a small part of the LO signal to leak through to the RF port even when the IQ inputs are zeroed. This leakage can be compensated by adding center-frequency ω_c dependent DC offset voltages to the IQ ports. The appropriate offset voltages can be determined by applying a continuous input signal at a frequency ω_c to the LO port of the mixer and minimizing the measured signal power at the RF port by varying the IQ offset voltages. To correct the sideband amplitude and phase errors we apply another correction procedure that we outline here. First, for the signals at the IQ inputs of the mixer we introduce the notation

$$A(t) = I(t) + iQ(t) = a(t)\exp(-i\phi(t)) \tag{4.2}$$

We consider an IQ signal at a single sideband frequency ω_{sb} and at fixed complex amplitude $a(t) = a = a_0 \exp(i\phi_0)$ such that $A(t) = a\exp(-i\omega_{sb}t)$. The effect of the gain and phase imperfections of the IQ mixers can then be modeled by assuming that the mixer adds another IQ signal $\epsilon(\omega_{sb}, \omega_c)A^*(t)$ at the mirrored sideband frequency $-\omega_{sb}$. We can correct this unwanted signal by adding a small correction $c(\omega_{sb}, \omega_c)A^*(t)$ to our IQ input signal. The correction coefficient $c(\omega_{sb}, \omega_c)$ usually depends both on the carrier frequency ω_c and the sideband frequency ω_{sb}. We determine the correction coefficients by generating a continuous waveform at a given center and sideband frequency, measuring the amplitude of the unwanted sideband signal with a fast spectrum analyzer and minimizing its amplitude by varying the correction coefficient $c(\omega_s b, \omega_c)$.

Both the offset and the sideband-amplitude and -phase corrections have been automatized using our data acquisition software, the resulting correction coefficients are summarized in fig. 4.3. By using the optimization techniques described above we can achieve -80 dBm residual power at the RF port of the mixer when no input IQ signal is present and a supression of the unwanted mirror sideband in heterodyne modulation > 70 dB !12! .

To Do 12: verify this number!

4.3.3 Fast Magnetic Flux Pulses

For the fast flux lines we use superconducting transmission lines which are attenuated by 20 dB and filtered at the 4K and 20 mK stages of the cryostat. The filtering at the 20 mK stage is realized using custom-built, highly absorptive high-frequency microwave filters. Fig. **??** shows an image of such a filter and the attenuation characteristic obtained for it. As can be seen, the filter shows an exponential attenuation and filters very effectively at high frequencies. This heavy filtering of the flux line is helpful since it greatly reduces high-frequency noise seen by the qubit but it also distorts all deterministic signals sent through the flux line. This distortion is unwanted especially at high frequencies and needs to be corrected. To do this we need to measure and compensate the frequency response of the flux line. In order to do this, we make use of the return line of the flux line and feed back the flux signal sent to the sample to room temperature. This allows us to measure the returning signal and – assuming symmetric distortion in the input and return line – to calculate the response function of the input line. Fig. 4.4 shows the different parts of the response function of the flux line as measured in our experiment. We can obtain the response function of the input part of the fluxline by sending a step-pulse through the flux line, measuring the Fourier spectrum of the returning signal and solving

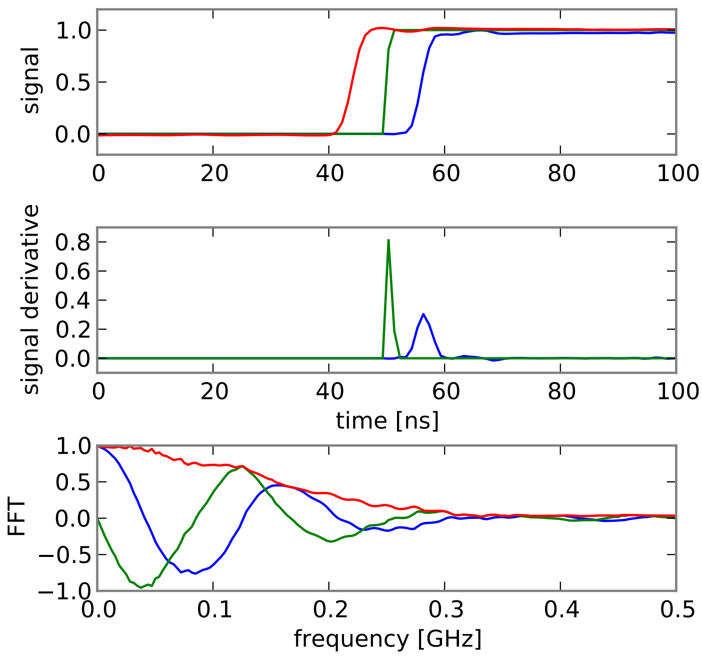

Figure 4.4: (response function filtered with a Gaussian filter with a cut-off at 0.4 GHz)

$$\chi_{out}(\omega) = \chi_{ideal}(\omega) \cdot \chi_{DAC} \cdot \chi_{in} \cdot \chi_{out} \cdot \chi_{ADC} \tag{4.3}$$

Here, χ_{ADC} and χ_{DAC} describe the response functions of the DAC and ADC, χ_{in} corresponds to the Fourier spectrum of the ideal input waveform and χ_{out} corresponds to the Fourier transform of the digitized return signal. We assume that $\chi_{in} \approx \chi_{out}$. By measuring χ_{out} and correcting the measured Fourier spectrum for the response function of the ADC χ_{ADC} we obtain the input line response $\chi_{DAC}\chi_{in}$ including the DAC response. We can then correct our digital input waveforms by applying

$$\chi_{in}^{corr} = \chi_{in} \cdot (\chi_{DAC} \cdot \chi_{in})^{-1} \cdot \mathrm{G}(f_0) \tag{4.4}$$

Here, $G(f_0)$ is a Gaussian filter that we apply to the measured response function to attenuate possible signal distortion that is caused by the fact that we are not able to accurately measure the response function of the system above a certain frequency. Usually, we set the cutoff frequency to $f_0 = 300$ MHz which allows us to correct most signal distortion effects in the frequency band relevant to us.

4.3.4 Pulse Synchronization

We use a 10 MHz chain to synchronize all relevant signal generator and acquisition cards of our setup. The chain topology is shown in detail in fig. **??**. In addition, we take great care to synchronize the frequencies of the microwave generators with the repetition interval of our arbitrary waveform generator to avoid phase-jitter which is catastrophic when generating IQ drive pulses for qubit control. In addition, we use a 1 GHz synchronization chain to phase-lock the microwave generators that produce the drive pulses for both qubits. Delays between qubit drive and fluxline signals that are caused by differences in electrical length of the respective signal lines are corrected for by using the qubit itself as a probe of the applied flux: For this, we use a step-like flux signal which shifts the qubit out of resonance with a pre-chosen Rabi pulse that performs a π rotation of the qubit state when in resonance. By varying the position of the step in respect to the π-pulse we can determine the exact timing between the two and correct for possible delays.

4.4 Measurement Techniques

In this section we will discuss the techniques used to characterize and manipulate our two-qubit processor. We will cover the qubit readout and manipulation and will describe how we can determine all relevant qubit parameters using microwave reflectometry measurements.

4.5 Qubit Readout

We use the nonlinear resonator as a Josephson bifurcation amplifier to read out the state of the qubit. This works by sending a drive pulse shaped as in fig. 4.5 to the sample. The frequency of this pulse is chosen such that it is inside the bistability region as given by eq. (2.62). Thus, there exists an amplitude for which the resonator will transit from a low-amplitude state to a high-amplitude one when continously increasing the drive power during the first part of the pulse. The value of this amplitude depends on the resonance frequency of the resonator, which itself depends on the state of the qubit through the dispersive coupling. If we choose the peak power of our measurement pulse such that it is very close to this transition amplitude, a small qubit-induced frequency shift of the resonator frequency will be able to significantly change the transition probability of the resonator when ramping up the power during the measurement pulse, thus making possible a measurement of the qubit state. After ramping up the microwave power to its peak value and holding it there for a certain amount of time, we reduce the power slightly to put the resonator within the bistability regime where its state is no longer sensitive to a shift of the resonator frequency, thus effectively decoupling the evolution of the resonator state from that of the qubit. We can then hold this state for an arbitrarily long time and measure the phase and amplitude of the reflected microwave signal during this “latching” period, thereby obtaining a precise measurement of the resonator state. The low- and high-amplitude resonator states are easily distinguishable when demodulating the reflected signal during the latching part of the pulse and averaging their respective IQ quadratures. When plotting many such averaged IQ quadratures for a measurement pulse which induces around 50 % switching to the high-amplitude state, one obtains a family of points as shown schematically in fig. 4.5. To distinguish between the two states H and L we perform a principal axes transformation of the data, effectively obtaining the separator plane P that distinguishes ideally between the two families. Projecting the IQ data along this discrimination line yields an effective probability distribution in one dimension from which we can directly calculate the switching

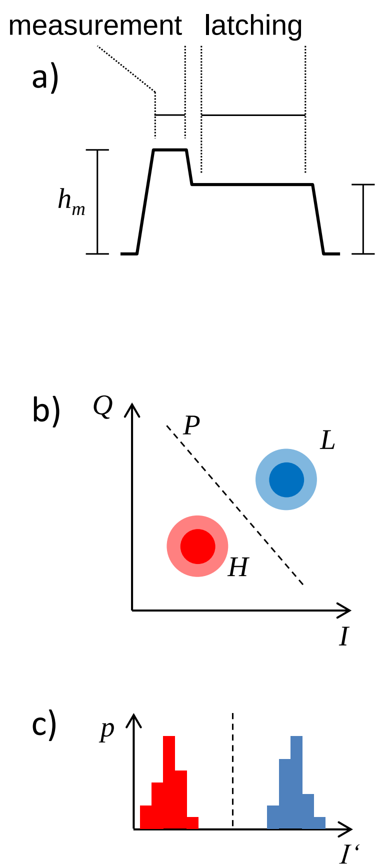

Figure 4.5: ...

probability for a given family of measurements.

4.6 Qubit Manipulation

To drive the qubits, we need to generate fast microwave pulses with a well defined frequency and phase. As described in one of the previous paragraphs we can use IQ sideband mixing to shape arbitrary drive pulses of the form

$$u(t) = I(t)\cos\omega_{rf}t + Q(t)\sin\omega_{rf}t \tag{4.5}$$

We can rewrite this as a product of two complex quantities

$$u(t) = \Re\left[A(t)\cdot\exp\left(-i\omega_{rf}t\right)\right] \tag{4.6}$$

where we defined, as before, $A(t) = I(t) + iQ(t)$. The reference phase defining an x-pulse can be chosen arbitrarily but must be conserved during one single experimental run. Thus, to realize a rotation of the qubit state in the xy-plane of the bloch sphere around an axis defined through an angle ϕ we can use a Gaussian-shaped pulse of the form

$$A(t) = A_0\cdot\exp\left(-\frac{(t-t_0)^2}{2\sigma_t}\right)\cdot\exp\left(-i\phi\right) \tag{4.7}$$

In the following chapter we will discuss more in detail the calibration of these drive pulses and possible errors induced when driving the qubit at frequencies comparable to its anharmonicity.

4.6.1 Spectroscopic Measurements of the Qubit State

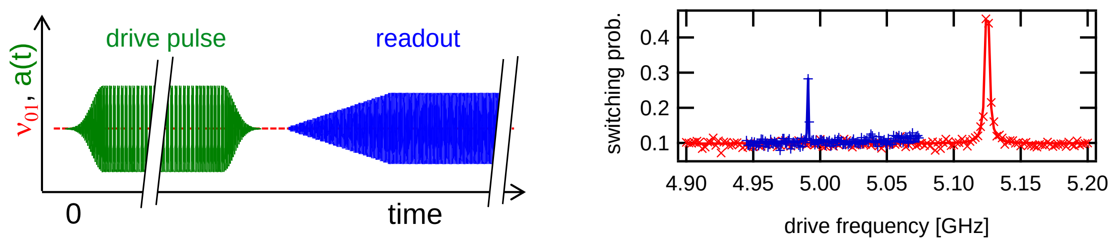

Figure 4.6: Example of a measured qubit spectroscopy. Shown is the switching probability of the qubit readout when driving the qubit with a very long drive pulse (typically 1 μs) at a given drive frequency. The resonance to the right corresponds to the $|0\rangle \rightarrow |1\rangle$ (at frequency f_{01})transition of the qubit, the resonance on the left to the 2-photon $|0\rangle \rightarrow |2\rangle$ (at frequency $f_{02}/2$) transition. We perform a Lorentzian fit of the two resonances to obtain the $|0\rangle \rightarrow |1\rangle$ and $|0\rangle \rightarrow |2\rangle/2$ resonance frequencies, from which we can calculate all other qubit transition frequencies.

In order to characterize the transition frequency and anharmonicity of the qubit it is useful to perform spectroscopic measurements of the qubit state. For this we drive the qubit with a very long Rabi pulse (usually > 500 ns at a well-defined frequency f_r. When the drive frequency f_r corresponds to the f_{01} frequency of the qubit the drive pulse will induce a strong Rabi oscillation of the quantum state of the qubit. Since the decoherence time of the qubit is of the order of the length of the drive pulse, the qubit state will decay and dephase during the driven evolution, effectively yielding an equal probability to measure the qubit in either of the states $|0\rangle$ or $|1\rangle$ at the end. When the drive frequency is detuned from the qubit transition frequency, no oscillation will be induced and hence the qubit will remain in the state $|0\rangle$. The width of the resonance in frequency space is inversely proportional to the dephasing time of the qubit, following the equation

$$\ldots \tag{4.8}$$

Fig. 4.6 shown an exemplatory qubit spectroscopy. Plotted is the probability of measuring the qubit in state $|1\rangle$ after applying a $1\ \mu$s rabi pulse at a given drive frequency to it. The blue curve has been measured at 10 dB higher power than the red curve and shows the $|0\rangle \rightarrow |2\rangle$ transition of the qubit. By fitting the resonance curves with a Lorentzian model we obtain the qubit frequencies f_{01} and $f_{02}/2$, which allow us to calculate the effective Josephson and charging energies at the given working point.

4.6.2 Rabi Oscillations

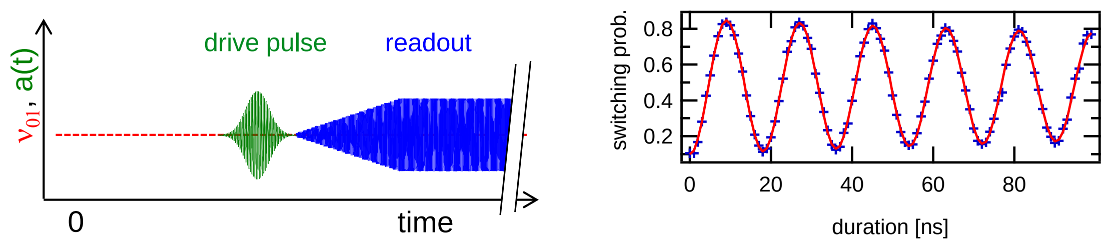

Figure 4.7: Example of a measured qubit Rabi experiment. Shown is the switching probability of the qubit readout when driving the qubit at f_{01} with a Gaussian drive pulse of varying duration. The measurement results are not corrected for readout errors.

After having obtained the proper qubit transition frequency f_{01} using the technique described above, we can perform a Rabi oscillation experiment by driving the qubit for a well-defined time with a drive pulse at the f_{01} transition frequency and measuring the state of the qubit directly afterwards. Fig. 4.7 shows an exemplatory Rabi measurement. The blue dots correspond to measured data points whereas the continuous red line corresponds to a fit of a model of the form $p(t) = p_0 + a\cos\Omega t \exp -\Gamma_1 t$ to the experimental data. As can be seen, the amplitude of the Rabi oscillations gets damped the longer the drive pulse becomes, which is due to relaxation and dephasing during the driven evolution of the qubit. The maximum probability contrast is limited due to readout errors, as we will explain in more detail in the following chapter. From the fit of the Rabi data we obtain the Rabi frequency Ω, which we can then use to perform precise single-qubit rotations, as will be explained later. Due to the finite anharmonicity of the qubit, there will always be a leakage to the second excited state $|2\rangle$ of the qubit wich gets stronger, the faster we drive the system. This leakage mechanism is an important source of errors and very relevant to the experiments that will be discussed later, so we will quantify it in detail in the following chapter as well.

4.7 Dephasing Time Measurement

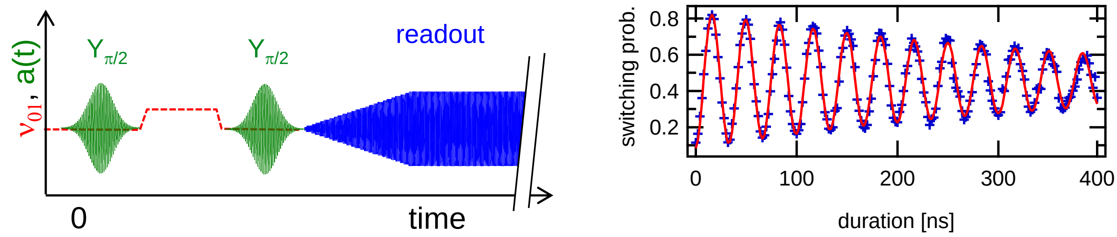

Figure 4.8: Example of a measured qubit Ramsey experiment. Shown is the switching probability of the qubit readout after performing a $X_{\pi/2}$-wait-$X_{\pi/2}$ drive sequence at a frequency $f_{01} - \delta f$. Fitting the resulting curve with an attenuated sine-wave model allows us to determine the f_{01} frequency of the Qubit with high accuracy.

After having obtained the transition frequency f_{01} of the qubit and the Rabi frequency Ω, we can characterize the dephasing of the qubit by performing a so-called *Ramsey fringe experiment*(). In this experiment, we perform a $Y_{\pi/2}$ rotation of the qubit from the state $|0\rangle$, obtaining thus a superposed qubit state of the form $1/\sqrt{2}(|0\rangle + |1\rangle)$. Then we displace the qubit frequency by an amount Δf by using e.g. a fast magnetic flux pulse and let the qubit state evolve freely during a certain amount of time Δt. Finally, we apply another $Y_{\pi/2}$ pulse to the qubit and measure the state of the qubit directly afterwards. Since the qubit frequency has been deplaced during the free evolution, the qubit will acquire a phase $\Delta\phi = 2\pi\Delta f\Delta t$. The final state of the qubit after applying the second $Y_{\pi/2}$ pulse will therefore be given as

$$|\phi_f\rangle = \begin{pmatrix} 1 & -1 \\ 1 & 1 \end{pmatrix} \cdot \begin{pmatrix} 1 \\ e^{i\Delta\phi} \end{pmatrix} = \begin{pmatrix} i\sin\Delta\phi/2 \\ -\cos\Delta\phi/2 \end{pmatrix} \tag{4.9}$$

Hence, the resulting state $|\phi_f\rangle$ will oscillate between the state $|0\rangle$ and $|1\rangle$ with a frequency $\Delta f/2$. As before, due to dephasing and relaxation during the free evolution of the qubit state, the amplitude of these oscillations will decay. If the system dephasing time is limited by qubit relaxation, the decay will follow a Gaussian decay of the form $\exp(-\Gamma t^2)$, otherwise it will also exhibit an exponential decay $\simeq \exp(-\Gamma t)$ (). In the Ramsey sequence, instead of detuning the qubit frequency during the free evolution phase we can also detune the qubit drive frequency instead. If this detuning is small in comparision to the Rabi frequency Ω, we will induce only a negligible error when applying the first $Y_{\pi/2}$ pulse. But since the drive frequency is detuned, the qubit will also acquire a phase $\Delta f \Delta t$ during the free evolution phase. Fitting the experimental data obtained for such an experiment to a model of the form $p(|1\rangle) = p_0 + a\cos(\Delta f \Delta t + \phi_0)\exp -\Gamma_2 t^2/2$ we can obtain an estimate of Δf. Since we know the frequency detuning of the drive during the free evolution of the qubit we can substract it from the fitted value in order to obtain the remaining detuning of the qubit from the drive frequeny at zero drive detuning. This method allows us thus to make a precise fit of the qubit frequency and to correct drive frequency errors with an accuracy of typically $100\,\mathrm{kHz}$.

4.8 Relaxation Time Measurement

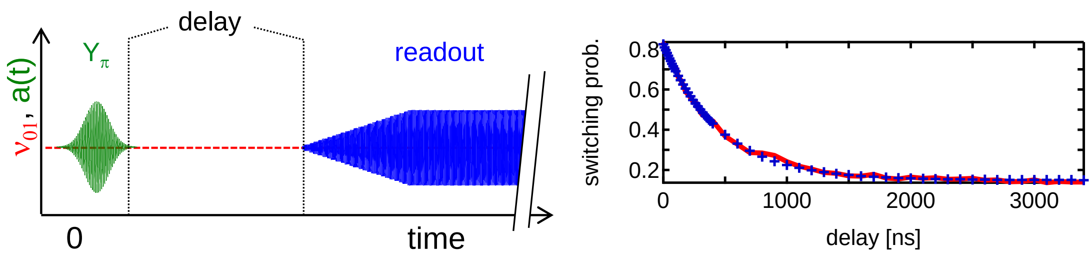

Figure 4.9: Example of a qubit relaxation time measurement. Shown is the probability of measuring the qubit in state $|1\rangle$ as a function of the delay time between the preparation of the state $|1\rangle$ and the actual measurement of the qubit state. The decay of this probability follows an exponential law of the form $p(|1\rangle) \simeq \exp(-\Gamma_1 t)$

We can characterize the relaxation time of the qubit by performing a simple experiment where we put the qubit in state $|1\rangle$ by applying a X_π pulse and let the qubit evolve freely for a given time before measuring its state. The resulting curve when performing such an experiment is shown in fig. 4.9. It shows the probability of measuring the qubit in state $|1\rangle$, plotted as a function of the delay between the initial state preparation and measurement. As can be seen, this probability decreases exponentially as a function of time. As before, in the curve the blue markers correspond to experimental data and the red line corresponds to a fit of this data to a model of the form $p(|1\rangle) = p_0 + p_a \exp(-\Gamma_1 t)$. From this fit we can then easily extract the relaxation rate Γ_1 of the qubit at the given working point. In the following chapter we will look more in detail at the relaxation time of both qubits as a function of their transition frequency and their detuning from the readout resonator.

Chapter 5

Characterizing the Two-Qubit Processor

This section discusses the detailed characterization of individual circuit parts that will be used later to realize two-qubit gate and to run a quantum algorithm on the processor. The discussion will focus on the readout and microwave manipulation of the qubits as well as on the reconstruction of quantum states from measurement data, which will be used later for characterizing gate and processor operation.

5.1 Qubit & Readout Characterization

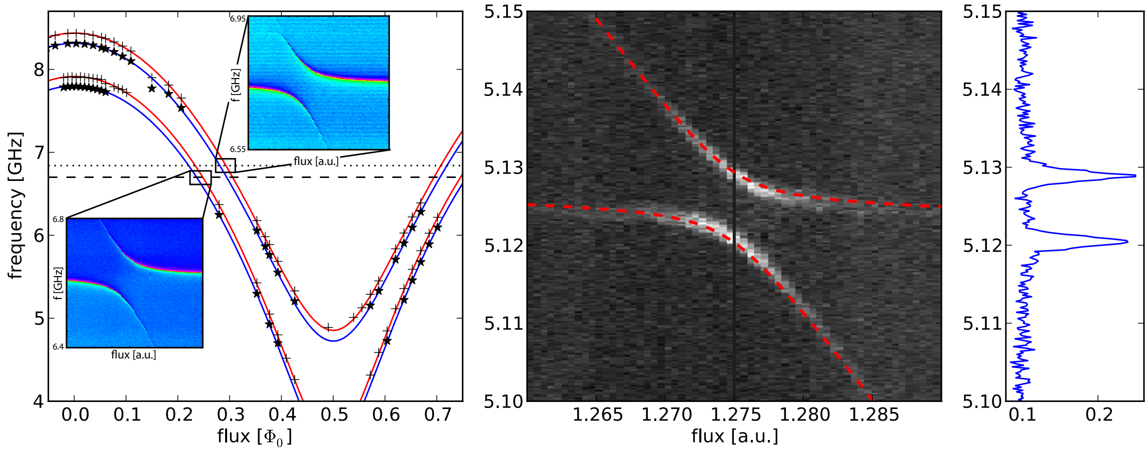

Figure 5.1: Spectroscopy of the realized two-qubit processor. a) $|0\rangle \rightarrow |1\rangle$ and $(|0\rangle \rightarrow |2\rangle)/2$ transition frequencies of the two qubits with fitted dependence and cavity frequencies. b) Avoided level crossing of the $|01\rangle$ and $|10\rangle$ levels of the qubits with fit, $g = 8.7\ \mathrm{MHz}$. c) Spectroscopy of qubit 1 at the point indicated in b).

The following section discusses the parameters of our two-qubit processor that have been obtained by various measurements.

5.1.1 Qubit Parameters

To obtain all the relevant parameters of our two-qubit processor, we perform a set of measurements from which we obtain the qubit frequencies, anharmonicities, junction asymmetries, the inter-qubit coupling, the coupling to the microwave drive lines, the coupling of each qubit to its readout and the relaxation and dephasing times of the qubits. The drive and readout couplings as well as the relaxation and dephasing times are measured for a range of qubit frequencies, which will allow us later to pick an ideal working point for our two-qubit experiments. The qubit parameters obtained from spectroscopic measurements are as follows:

- *Qubits*: Spectroscopic measurement of the qubit transitions yielded parameter values of $E_J^I/h = 36.2\ \mathrm{GHz}$, $E_c^I/h = 0.98\ \mathrm{GHz}$ and $E_J^{II}/h = 43.1\ \mathrm{GHz}$, $E_C^{II}/h = 0.87\ \mathrm{GHz}$ for the Josephson and charging energies of the two qubits and values of $d^I = 0.2$, $d^{II} = 0.35$ for the qubit junction asymmetries.
- *Readout resonator*: The frequencies of the readout resonators have been measured as $\nu_R^I = 6.84\ \mathrm{GHz}$ and $\nu_R^{II} = 6.70\ \mathrm{GHz}$ with quality factors $Q^I \simeq Q^{II} = 730$, independent measurements of the Kerr nonlinearities yielded $K^I/\nu_R^I \simeq K^{II}/\nu_R^{II} = -2.3 \pm 0.5 \times 10^{-5}$!13! .

To Do 13: add junction parameters inferred from the bare resonator frequencies

- *Qubit-Resonator coupling*: The coupling of the qubits to the readout resonators has been spectroscopically determined as $g_0^I \simeq g_0^{II} = 50\ \mathrm{MHz}$

Readout Parameters

Qubit Readout, Driving, Relaxation and Dephasing Time

In order to obtain the relaxation time and the coupling of the qubit to the drive line, we perform an automated survey of qubit spectroscopies, qubit readout characterizations and T_1 measurements at different qubit frequencies. The results of such a parameter survey are summarized in fig 5.2, showing the relaxation time T_1, the readout contrast c_{10} and the Rabi frequency f_{Rabi} for a fixed drive amplitude for the two qubits in a frequency range between 5.2 and 6.5 GHz. As can be seen, the relaxation time of the qubits tends to increase the farther detuned each qubit is from its readout resonator. Not surprisingly, the drive frequency of the qubit also decreases when the qubit-resonator detuning increases as expected from the Purcell effect, which filters incoming microwave signals that are far-detuned from the resonator frequency. The inverse is true for the readout contrast, which increases near-linearly when reducing the qubit-resonator detuning due

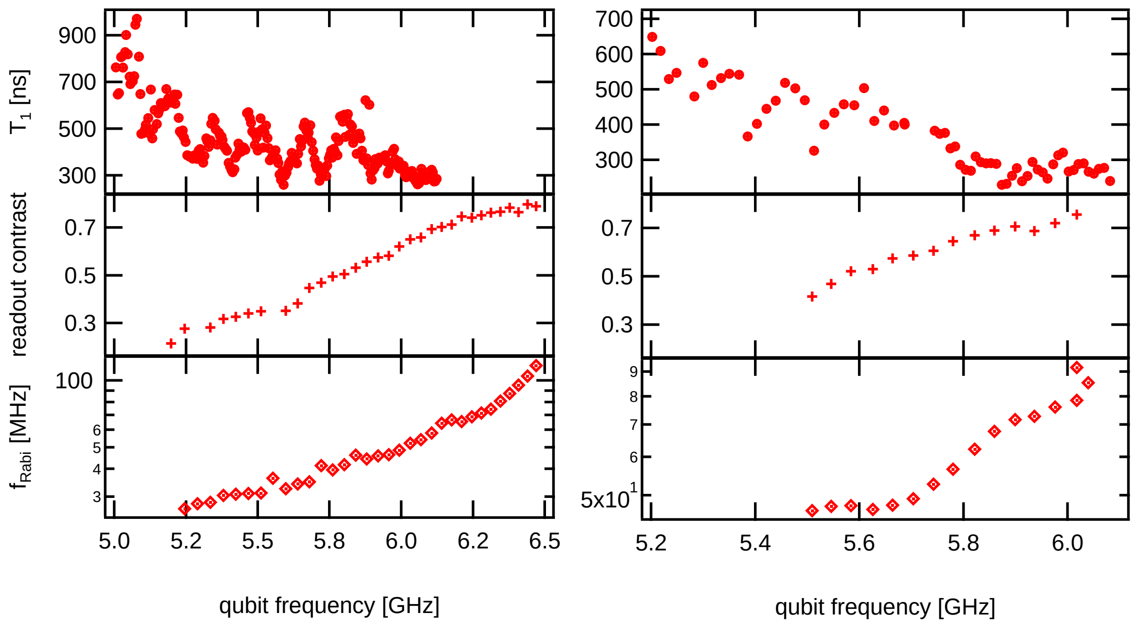

Figure 5.2: A qubit parameter survey showing the relaxation time T_1, the readout contrast and the Rabi frequency at a fixed drive amplitude for the two qubits over a large range of qubit frequencies.

to the increase of the dispersive resonator frequency shift induced by the qubit that gets stronger the less the qubit is detuned from the readout resonator.

It is interesting to note the non-monotnous characteristic of the qubit relaxation time T_1 shown in fig. 5.2, which cannot be explained by Purcell-filtering through the read-out resonator and hints at a different qubit relaxation process present in the system. A possible explanation would be the coupling of the qubit to a spurious low-Q resonance in the environment. Coupling to volumetric resonance modes of the sample holder or non-CPW resonance modes of the readout resonator can be possible explanations for the data. Also, the overall dependency of the relaxation time T_1 on the qubit-resonator detuning –ignoring the "fine-structure" present in the system– is not quadratic as would be expected from the Purcell theory but rather linear. Also, by comparing the qubit relaxation time to the Rabi drive frequency reveals that the increase in T_1 is cleary not proportional to the Purcell factor that determines the qubit relaxation rate through the readout resonator. However, the observed T_1 dependency can be partially explained by taking into account the qubit relaxation through the fast fluxline, which might be to strongly-coupled to the qubit on our chip, hence inducing additional qubit relaxation beyond the Purcell and intrinsic qubit relaxation rates. This effect will therefore be studied in more detail in the following sections.

5.2 Single-Qubit Operations

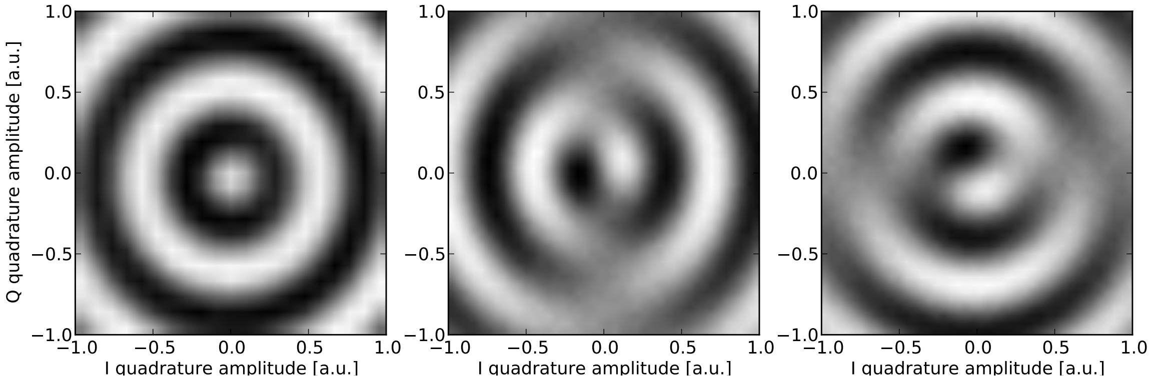

Figure 5.3: Demonstration of single-qubit IQ control. The figures show the state probability of a single qubit when preparing it in one of the states $|1\rangle$, $1/\sqrt{2}(|0\rangle+|1\rangle)$ or $1/\sqrt{2}(|0\rangle+i\,|1\rangle)$ and subjecting the qubit to a microwave drive pulse of the form $a(t) = V_I \cdot \cos\omega_{rf}t + V_Q \cdot \sin\omega_{rf}t$.

To perform arbitrary single-qubit operations – as needed e.g. for implementing a quantum algorithm or performing quantum state tomography – we need to implement a universal set of X, Y and Z qubit gates with our processor. Qubit rotations in the XY-plane are implemented through microwave drive pulses, where the phase of the drive pulse in reference to an arbitrary reference determines the rotation axis and the amplitude of the drive pulse the Rabi frequency of the gate. To characterize the drive pulses, we perform an experiment where we initialize a single-qubit in the states $|1\rangle$, $1/\sqrt{2}(|0\rangle+|1\rangle)$ and $\sqrt{2}(|0\rangle+i\,|1\rangle)$ and subject it afterwards to a single microwave pulse of the form $a(t) = V_I \cdot \cos\omega_{rf}t + V_Q \cdot \sin\omega_{rf}t$, which we tune by changing the input voltages V_I and V_Q to the IQ-mixer that generates the pulse from a continuous input micrwave-tone at frequency ω_{rf}. We measure the qubit state at different values of V_I, V_Q, obtaining the graph shown in fig. 5.3. The qubit which was prepared in state $|1\rangle$ shows a perfectly cylinder-symmetric switching probability pattern when subjecting it to an IQ-pulse of a given phase, which is what one would expect for a qubit being prepared in either the $|0\rangle$ or $|1\rangle$ state. On the contrary, the switching probability distributions of the measured qubits prepared in the states $1/\sqrt{2}(|0\rangle+|1\rangle)$ and $1/\sqrt{2}(|0\rangle+i\,|1\rangle)$ are mirror-symmetric, where the switching probability does not vary at all along the drive axis which corresponds to the axis along which the qubit has been prepared. These measurements demonstrate therefore our ability to prepare and drive the qubit along arbitrary axes of the Bloch sphere. In the following sections we will analyze more in detail the drive errors inherent to our system and quantitatively analyze differnt error sources.

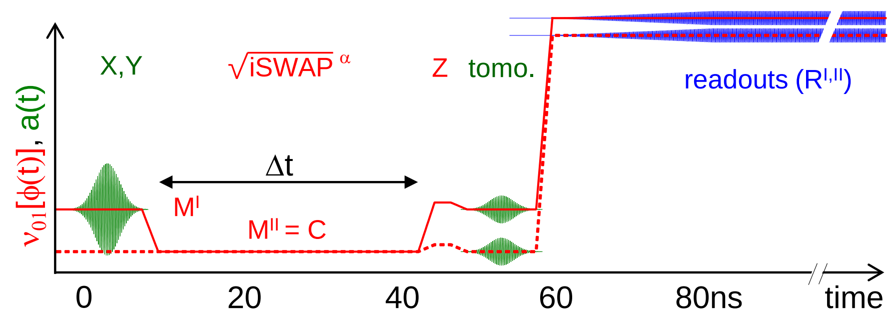

Figure 5.4

5.2.1 Estimation of drive errors

Since the Transmon is a weakly anharmonic multi-level system and thus no real qubit, driving the $|0\rangle \rightarrow |1\rangle$ transition with high power can induce transitions to higher Transmon levels. It is important to estimate and reduce these errors when performing fast qubit gates e.g. for state preparation or tomography. To model the driving of a Transmon, we use the simple drive model in the rotating-frame approximation and as used e.g. in Motzoi et al. (2009):

$$\hat{H} = \begin{pmatrix} 0 & \epsilon^*(t) & 0 \\ \epsilon(t) & \delta & \sqrt{2}\epsilon^*(t) \\ 0 & \sqrt{2}\epsilon(t) & 2\delta + \alpha \end{pmatrix} \tag{5.1}$$

Here, $\epsilon(t) = \epsilon_x(t) + i\epsilon_y(t)$ is the complex drive IQ amplitude in the rotating qubit frame, δ is the detuning of the microwave drive from the Transmon ω_{01} transition frequency and α is the Tranmon anharmonicity. To estimate the leakage

5.3 Two Qubit Operations

5.3.1 Creation of Entanglement

5.3.2 Violation of the Bell Inequality

$$\mathrm{CHSH} = \mathrm{QS} + \mathrm{RS} + \mathrm{RT} - \mathrm{QT} \tag{5.2}$$

with the operators $\mathrm{Q}, \mathrm{R}, \mathrm{S}, \mathrm{T}$ being defined as

$$\begin{aligned} \mathrm{Q} &= \sigma_z^1 & \mathrm{S} &= \sigma_z^2 \cdot \cos\phi + \sigma_x^2 \cdot \sin\phi \\ \mathrm{R} &= \sigma_x^1 & \mathrm{T} &= -\sigma_z^2 \cdot \sin\phi + \sigma_x^2 \cdot \cos\phi \end{aligned} \tag{5.3}$$

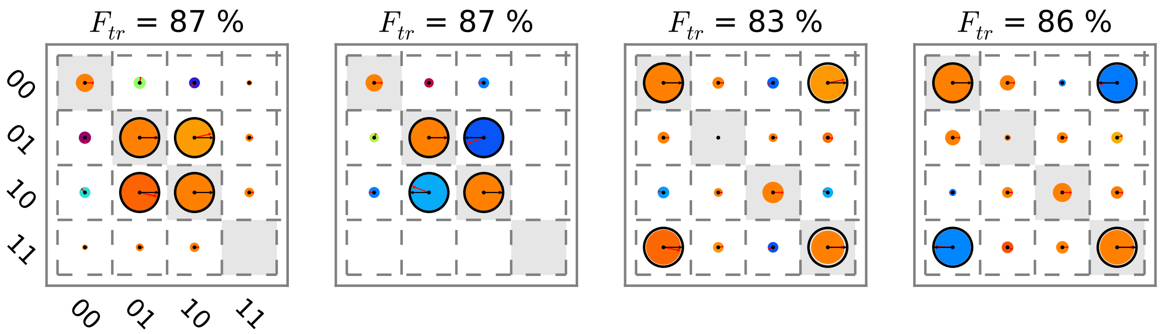

Figure 5.5: Experimentially created $|\psi_+\rangle$ $(F = 0.91)$ and $|\psi_-\rangle$ $(F = 0.93)$ states

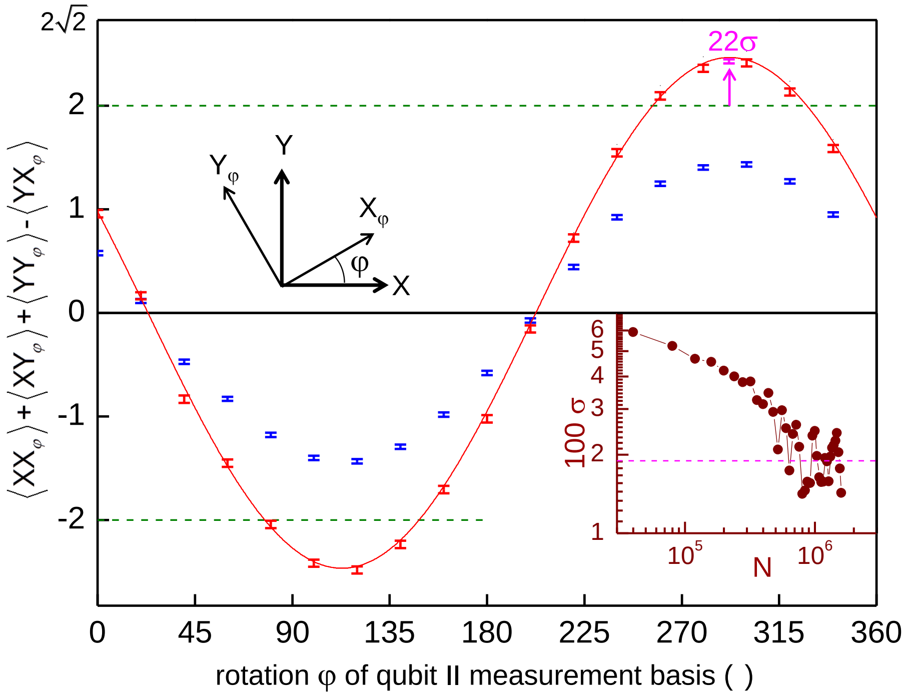

Figure 5.6

Here, the angle ϕ is a parameter that should be chosen in accordance to the phase of the Bell state on which it is applied.

5.3.3 Quantum State Tomography of Two-Qubit States

Quantum state tomography is the procedure of experimentally determining an unknown quantum state(Michael A. Nielsen and Isaac L. Chuang, 2000).

The density matrix of an n-qubit system can be written in general form as

$$\rho = \sum_{v_1, v_2 \dots v_n} \frac{c_{v_1, v_2 \dots v_n} \sigma_{v_1} \otimes \sigma_{v_2} \dots \sigma_{v_n}}{2^n} \tag{5.4}$$

$$c_{v_1, v_2 \dots v_n} = \operatorname{tr}\left(\sigma_{v_1} \otimes \sigma_{v_2} \dots \otimes \sigma_{v_n} \ \rho\right) \tag{5.5}$$

where $v_i \in \{X, Y, Z, I\}$ and n gives the number of qubits in the system and where the $c_{v_1, v_2 \dots v_n}$ are real-valued coefficients that fully describe the given density matrix. To reconstruct the density matrix of an experimental quantum system in a well-prepared state it is therefore sufficient to measure the expectation values of these $n^2 - 1$ coefficients on an ensemble of identically prepared systems. However, statistical and systematic measurement errors can yield a set of coefficients that corresponds to a *non-physical* density matrix which violates either the positivity or unity-trace requirement. In the following paragraph we will therefore discuss a technique with which one can estimate the density matrix of a system in a more correct way.

Maximum Likelihood Estimation of Quantum States

A method which is often used in quantum state tomography is the so-called *maximum-likelihood* technique. Rather than directly calculating the density matrix of the system from the obtained expectation values $c_{v_1, v_2 \dots v_n}$, it calculates the joint probability of measuring a set $\{c_{X,X,\dots,X}, c_{Y,X,\dots,X}, \dots, c_{I,I,\dots,I}\}$ for a given estimate of the density matrix $\hat{\rho}$. By numerically or analytically maximizing this joint probability over the set of possible density matrices we obtain the density matrix which is most likely to have produced the set of measurement outcomes that we have observed.

The joint measurement operators $\Sigma_j = \sigma_{v_1} \otimes \sigma_{v_2} \dots \otimes \sigma_{v_n}$ have the eigenvalues ± 1 and can thus be written as

$$\sigma_{v_1} \otimes \sigma_{v_2} \dots \otimes \sigma_{v_n} = \left|+_j\right\rangle \left\langle +_j\right| - \left|-_j\right\rangle \left\langle -_j\right| \tag{5.6}$$

where $\left|-_j\right\rangle$ and $\left|-_j\right\rangle$ are the eigenstates corresponding to the eigenvalues ± 1 of Σ_j.

The expectation value $\langle\Sigma_j\rangle$ can be estimated by the quantity

$$\widehat{\langle\Sigma_j\rangle}_\rho = \frac{1}{l}\sum_{i=1}^{l} M_i(\Sigma_j,\rho) \tag{5.7}$$

where $M_i(M,\rho)$ denotes the outcome of the i-th measurement of the operator M on the state described by the density matrix ρ. This quantity is binomially distributed with the expectation value $E(\widehat{\langle\Sigma_j\rangle}_\rho) = \langle\Sigma_j\rangle_\rho$ and the variance $\sigma^2(\widehat{\langle\Sigma_j\rangle}_\rho) = 1/l\cdot(1-\langle\Sigma_j\rangle_\rho^2)$. For large sample sizes l, the binomial distribution can be well approximated by a normal distribution with the same expectation value and variance. The joint probability of obtaining a set of measurement values $\{s_1,\ldots,s_{n^2-1}\}$ for the set of operators $\{\widehat{\langle\Sigma_1\rangle}_\rho,\ldots,\widehat{\langle\Sigma_{n^2-1}\rangle}_\rho\}$ is then given as

$$P\left(\widehat{\langle\Sigma_1\rangle}_\rho = s_1;\ldots;\widehat{\langle\Sigma_{n^2-1}\rangle}_\rho = s_{n^2-1}\right) = \prod_{i=1}^{n^2-1}\exp\left(-\frac{l}{2}\frac{(s_i-\langle\Sigma_i\rangle_\rho)^2}{1-\langle\Sigma_i\rangle_\rho^2}\right) \tag{5.8}$$

By maximizing this probability (or the logarithm of it) we obtain an estimate of the density matrix ρ of the quantum state. This technique also allows us to include further optimization parameters when calculating the joint probability. This is useful for modeling e.g. systematic errors of the measurement or preparation process, which can be described by modifying the operators contained in the probability sum. A common source of errors in our tomography measurements are errors in the microwave pulses used to drive the qubit. Since our measurement apparatus permits us only to measure the σ_z operator of each qubit we have to perform $\pi/2$ rotations about the Y or $-X$ axes of the Bloch sphere of each individual qubit in order to measure the values of the σ_x and σ_y operators, which we therefore replace with an effective measurement of each qubits σ_z operator preceded by a rotation R_{ν_i} given as

$$R_X = \exp(-i\sigma_y\pi/4) \tag{5.9}$$
$$R_Y = \exp(+i\sigma_x\pi/4) \tag{5.10}$$

Phase and amplitude errors can be modeled as

$$R_X = \exp\left(-i\left[+\sigma_y\cos\alpha+\sigma_x\sin\alpha\right]\left[\pi/4+\gamma\right]\right) \tag{5.11}$$
$$R_Y = \exp\left(+i\left[-\sigma_y\sin\beta+\sigma_x\cos\beta\right]\left[\pi/4+\delta\right]\right) \tag{5.12}$$

Here, α and β represent phase errors whereas γ and δ represent amplitude errors in the drive pulses.

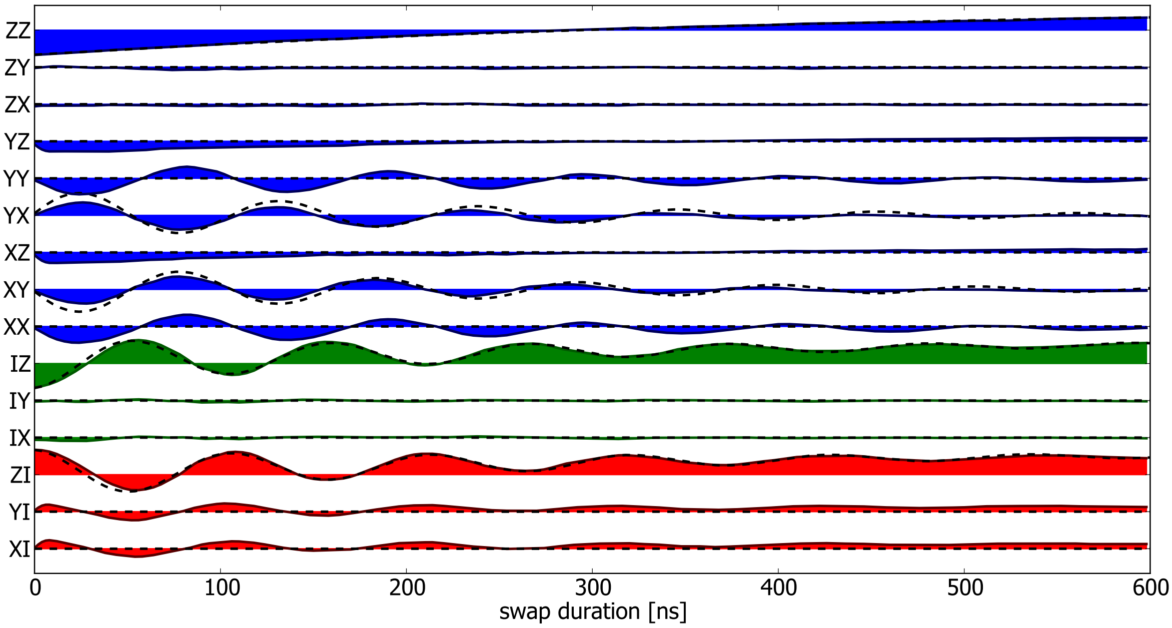

Figure 5.7: Measured Pauli operators $\sigma_i \otimes \sigma_j$ with $i, j \in \{X, Y, Z, I\}$ as a function of the interaction time. Shown are the 6 single-qubit operators as well as the 9 two-qubit correlation operators. The dashed line represents a master-equation simulation of the experiment.

5.4 Realizing a Two-Qubit Gate

5.4.1 Principle

5.4.2 Experimental Implementation

5.4.3 Quantum Process Tomography of the Gate

Introduction & Principle

Implementation

A quantum process can be described as a map $\mathcal{E} : \rho_{\mathcal{H}} \rightarrow \rho_{\mathcal{H}}$ that maps a density matrix ρ defined in a Hilbert space Q_1 to another density matrix $\mathcal{E}(\rho)$ defined in a target Hilbert space Q_2 and fulfilling three axiomatic properties Michael A. Nielsen and Isaac L. Chuang (2000); Haroche and Raimond (2006):

Axiom 5.0.1. $\mathrm{tr}\left[\mathcal{E}(\rho)\right]$ is the probability that the process represented by $\mathcal{E}$ occurs, when ρ is the initial state.

Axiom 5.0.2. $\mathcal{E}$ is a *convex-linear map* on the set of density matrices, that is, for probabilities $\{p_i\}$,

$$\mathcal{E}\left(\sum_i p_i \rho_i\right) = \sum_i p_i \mathcal{E}(\rho_i) \tag{5.13}$$

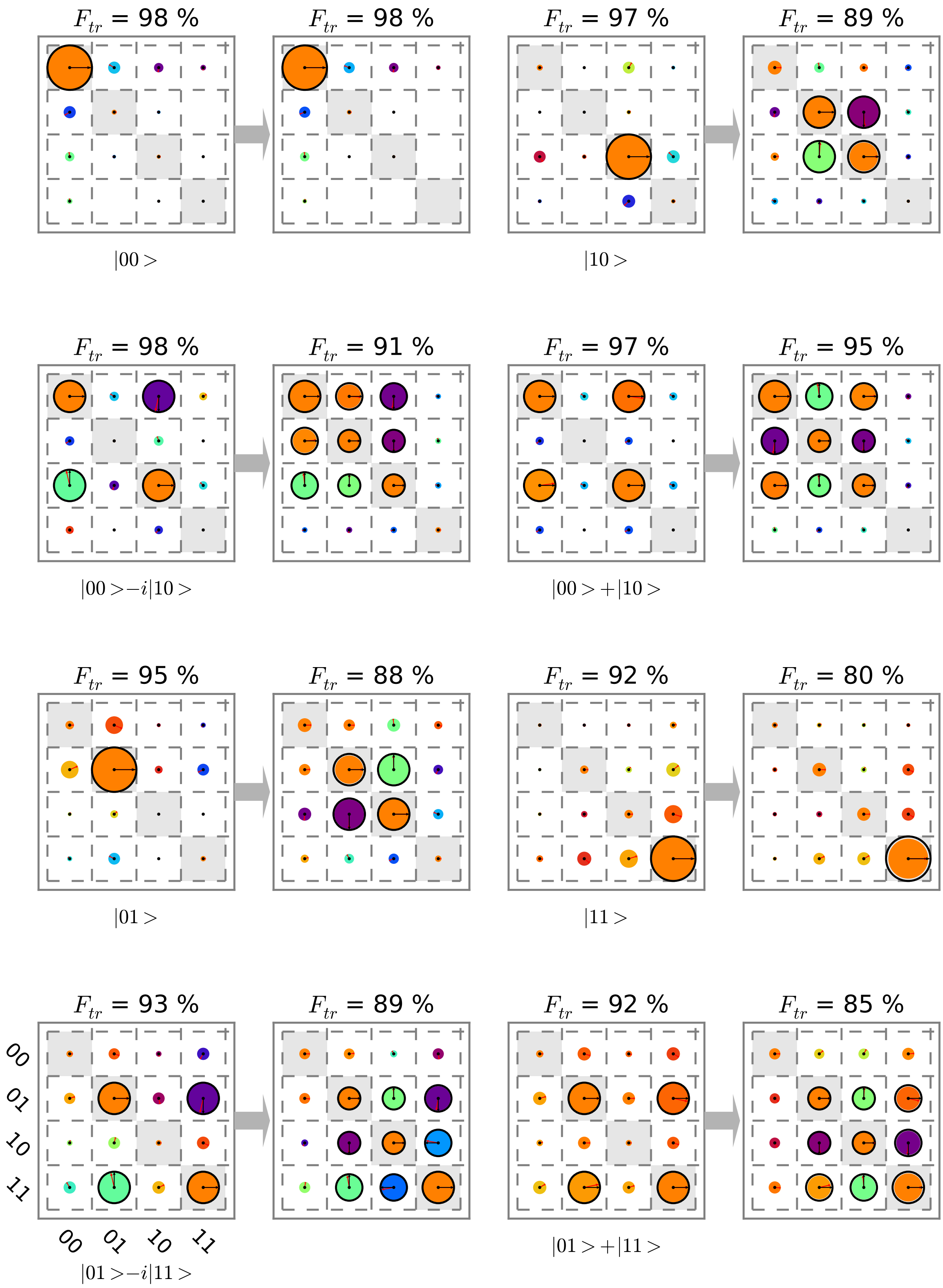

Figure 5.8: The input-output density matrix of the quantum process tomography of the $\sqrt{i\mathrm{SWAP}}$ gate. Shown are the measured density matrices of 16 different input states and the corresponding output matrices with their state fidelities. The ideal matrices are overlaid in red.

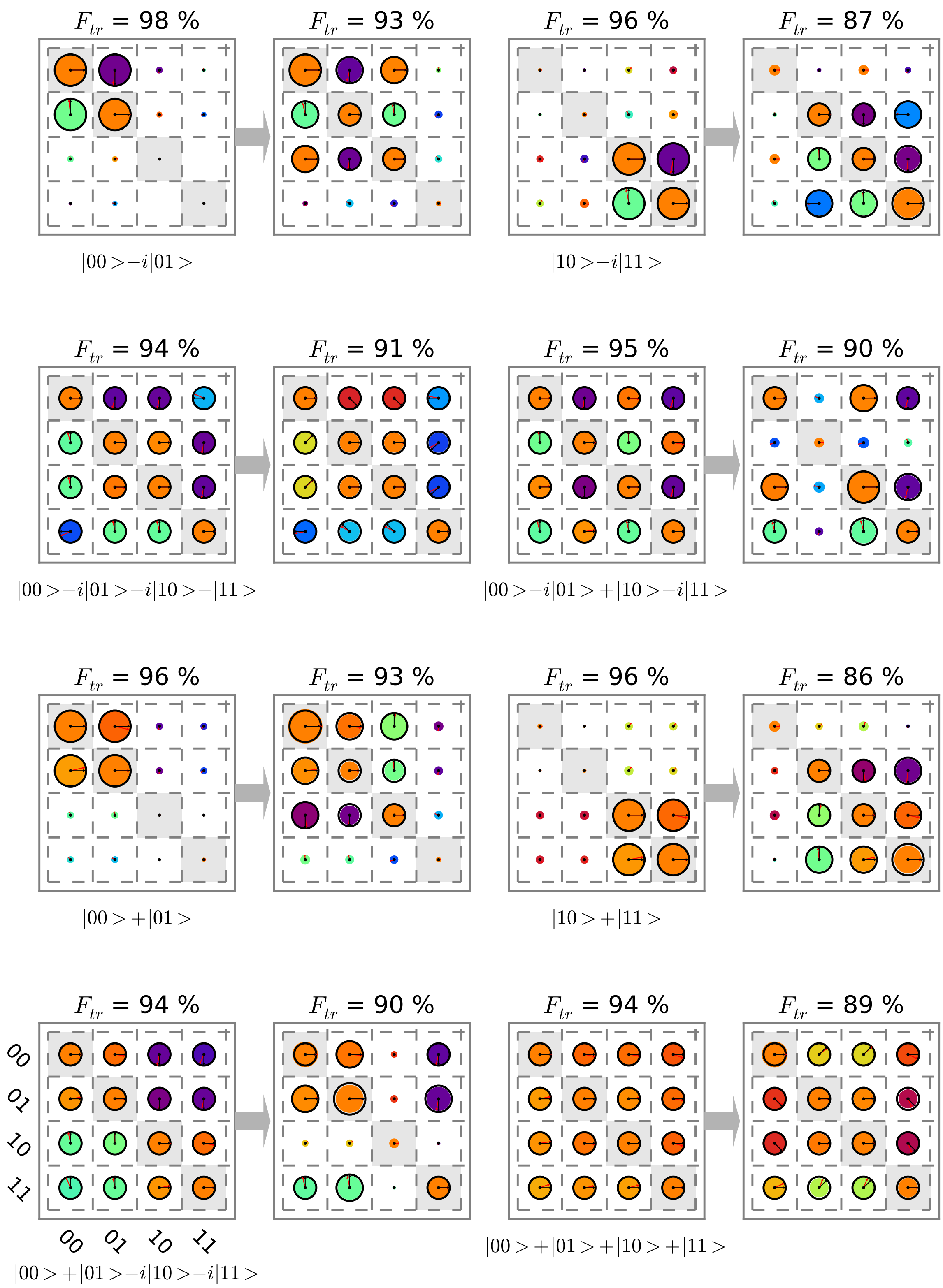

Figure 5.9: The input-output density matrix of the quantum process tomography of the $\sqrt{i\mathrm{SWAP}}$ gate. Shown are the measured density matrices of 16 different input states and the corresponding output matrices with their state fidelities. The ideal matrices are overlaid in red.

Axiom 5.0.3. $\mathcal{E}$ is a *completely-positive* map. That is, if $\mathcal{E}$ maps density operators of system Q_1 to density operators of system Q_2, then $\mathcal{E}(A)$ must be positive for any positive operator A. Furthermore, if we introduce an extra system R of arbitrary dimensionality, it must be true that $(\mathcal{I} \otimes \mathcal{E})(A)$ is positive for any positive operator A on the combined system RQ_1, where $\mathcal{I}$ denotes the identity map on system R.

As shown in Michael A. Nielsen and Isaac L. Chuang (2000), any quantum process fulfilling these criteria can be written in the form

$$\mathcal{E}(\rho) = \sum_i E_i \rho E_i^\dagger \tag{5.14}$$

for some set of operators $\{E_i\}$ which map the input Hilbert space to the output Hilbert space, and $\sum_i E_i^\dagger E_i \leq I$.

Now, if we express the operators E_i in a different operator basis $\tilde{E}_j$ such that $E_i = \sum_j a_{ij} \tilde{E}_j$ and insert into eq. (5.14), we obtain

$$\begin{aligned}
\mathcal{E}(\rho) &= \sum_i \sum_j a_{ij} \tilde{E}_j \; \rho \; \sum_k a_{ik}^* \tilde{E}_k^\dagger && (5.15) \\
&= \sum_{j,k} \tilde{E}_j \; \rho \; \tilde{E}_k^\dagger \sum_i a_{ij} a_{ik}^* && (5.16) \\
&= \sum_{j,k} \tilde{E}_j \; \rho \; \tilde{E}_k^\dagger \; \chi_{jk} && (5.17)
\end{aligned}$$

where we defined $\chi_{jk} = \sum_i a_{ij} a_{ik}^*$. This is the so-called χ-matrix representation of the quantum process. Here, all the information on the process is contained in the χ matrix, which controls the action of the process-independent operators $\tilde{E}_i$ on the initial density matrix ρ.

Now, the goal of *quantum process tomography* is to obtain the coefficients of the χ-matrix – or any other complete representation of the process – from a set of experimentally measured density matrices ρ and $\mathcal{E}(\rho)$.

To achieve this, several techniques have been developed. The technique used in this work is the so-called *standard quantum process tomography (SQPT)*. This technique proceeds as follows:

1. Choose a set of operators E_i that forms a full basis of $\mathcal{M} : Q_1 \to Q_2$. For n-qubit process tomography we usually choose $E_{i_1,i_2 \ldots i_n} = \sigma_{i_1} \otimes \sigma_{i_2} \ldots \otimes \sigma_{i_n}$, where σ_i are the single-qubit Pauli operators and $i \in \{I, X, Y, Z\}$.

2. Choose a set of pure quantum states $|\phi_i\rangle$ such that $|\phi_i\rangle \langle\phi_i|$ span the whole space of input density matrices ρ. Usually, for a n-qubit system we choose $\phi =$

$\{|0\rangle, |1\rangle, (|0\rangle + |1\rangle)/\sqrt{2}, (|0\rangle + i|1\rangle)/\sqrt{2}\}^{\otimes n}$, where $^{\otimes n}$ denotes the n-dimensional Kronecker product of all possible permutations.

3. For each of the $|\phi_i\rangle$, determine $\mathcal{E}(|\phi_i\rangle\langle\phi_i|)$ by quantum state tomography. Usually we also determine $|\phi_i\rangle\langle\phi_i|$ experimentally since the preparation of this state already entails small preparation errors that should be taken into account when performing quantum process tomography.

After having obtained the ρ_i and $\mathcal{E}(\rho_i)$ one obtains the χ-matrix by writing $\mathcal{E}(\rho_i) = \sum_j \lambda_{ij}\tilde{\rho}_j$, with some arbitrary basis $\tilde{\rho}_j$ and letting $\tilde{E}_m\tilde{\rho}_j\tilde{E}_n^\dagger = \sum_k \beta_{jk}^{mn}\tilde{\rho}_k$. We can then insert into eq. (5.17) and obtain

$$\sum_k \lambda_{ik}\tilde{\rho}_k = \sum_{m,n}\chi_{mn}\sum_k \beta_{ik}^{mn}\tilde{\rho}_k \tag{5.18}$$

This directly yields $\lambda_{ik} = \sum_{m,n}\beta_{ik}^{mn}\,\chi_{mn}$, which, by linear inversion, gives χ.

The Kraus Representation of the Quantum Process

Besides the χ-matrix representation, there is another useful way of expressing a quantum map, the so called *Kraus representation*, which is given as

$$\mathcal{E}(\rho) = \sum_i M_i\,\rho\,M_i^\dagger \tag{5.19}$$

It can be shown (Haroche and Raimond, 2006) that this sum contains at most N elements, where N is the dimension of the Hilbert space of the density matrix ρ. We can go from the χ representation to the Kraus representation by changing the basis $\tilde{E}_i$ such that

$$\tilde{E}_i = \sum_l a_{il}\,\breve{E}_l \tag{5.20}$$

which, for eq. (5.17), yields

$$\begin{aligned}\mathcal{E}(\rho) &= \sum_{j,k}\sum_l a_{jl}\breve{E}_l\,\rho\sum_m a_{km}^*\breve{E}_m^\dagger\,\chi_{jk} &(5.21)\\ &= \sum_{l,m}\breve{E}_l\,\rho\,\breve{E}_m^\dagger\,\sum_{j,k} a_{jl}a_{km}^*\chi_{jk} &(5.22)\end{aligned}$$

The last sum on the right side of eq. (5.22) corresponds to a change of coordinates of the matrix χ. Now, we can pick the a such that χ is diagonal in the new basis $\breve{E}$ and obtain

$$\mathcal{E}(\rho) = \sum_l \lambda_l \breve{E}_l \, \rho \, \breve{E}_l^\dagger \tag{5.23}$$

$$= \sum_l M_l \, \rho \, M_l^\dagger \tag{5.24}$$

with λ_l being the l-th eigenvalue of the χ matrix with the eigen-operator $\breve{E}_l$ and $M_l = \sqrt{\lambda_l}\breve{E}_l$.

5.4.4 Gate Fidelity

5.4.5 Gate Error Analysis

Tomographic errors are removed from the process map of our $\sqrt{iSWAP}$ gate using the following method. The measured Pauli sets corresponding to the sixteen input states are first fitted by a model including errors both in the preparation of the state (index $prep$) and in the tomographic pulses (index $tomo$). The errors included are angular errors $\varepsilon_{\mathrm{I,II}}^{\mathrm{prep}}$ on the nominal π rotations around $X_{\mathrm{I,II}}$, $\eta_{\mathrm{I,II}}^{\mathrm{prep,tomo}}$and $\delta_{\mathrm{I,II}}^{\mathrm{prep,tomo}}$ on the nominal $\pi/2$ rotations around $X_{\mathrm{I,II}}$ and $Y_{\mathrm{I,II}}$, a possible departure $\xi_{\mathrm{I,II}}$ from orthogonality of $\left(\overrightarrow{X_{\mathrm{I}}}, \overrightarrow{Y_{\mathrm{I}}}\right)$ and $\left(\overrightarrow{X_{\mathrm{II}}}, \overrightarrow{Y_{\mathrm{II}}}\right)$, and a possible rotation $\mu_{\mathrm{I,II}}$ of the tomographic XY frame with respect to the preparation one. The rotation operators used for preparing the states and doing their tomography are thus given by

$$\begin{gathered}
X_{\mathrm{I,II}}^{\mathrm{prep}}(\pi) = e^{-\mathrm{i}\left(\pi+\varepsilon_{\mathrm{I,II}}^{\mathrm{prep}}\right)\sigma_{\mathrm{x}}^{\mathrm{I,II}}/2}, \\
X_{\mathrm{I,II}}^{\mathrm{prep}}(-\pi/2) = e^{+\mathrm{i}\left(\pi/2+\eta_{\mathrm{I,II}}^{\mathrm{prep}}\right)\sigma_{\mathrm{x}}^{\mathrm{I,II}}/2}, \\
Y_{\mathrm{I,II}}^{\mathrm{prep}}(\pi/2) = e^{-\mathrm{i}\left(\pi/2+\delta_{\mathrm{I,II}}^{\mathrm{prep}}\right)\left[\cos\left(\xi_{\mathrm{I,II}}\right)\sigma_{\mathrm{y}}^{\mathrm{I,II}}-\sin\left(\xi_{\mathrm{I,II}}\right)\sigma_{\mathrm{x}}^{\mathrm{I,II}}\right]/2}, \\
X_{\mathrm{I,II}}^{\mathrm{tomo}}(\pi/2) = e^{-\mathrm{i}\left(\pi/2+\eta_{\mathrm{I,II}}^{\mathrm{tomo}}\right)\left[\sin\left(\mu_{\mathrm{I,II}}\right)\sigma_{\mathrm{x}}^{\mathrm{I,II}}+\cos\left(\mu_{\mathrm{I,II}}\right)\sigma_{\mathrm{y}}^{\mathrm{I,II}}\right]/2}, \\
Y_{\mathrm{I,II}}^{\mathrm{tomo}}(-\pi/2) = e^{+\mathrm{i}\left(\pi/2+\delta_{\mathrm{I,II}}^{\mathrm{tomo}}\right)\left[\cos\left(\mu_{\mathrm{I,II}}+\xi_{\mathrm{I,II}}\right)\sigma_{\mathrm{y}}^{\mathrm{I,II}}-\sin\left(\mu_{\mathrm{I,II}}+\xi_{\mathrm{I,II}}\right)\sigma_{x}^{\mathrm{I,II}}\right]/2}.
\end{gathered}$$

The sixteen input states are then $\left\{\rho_{\mathrm{in}}^{\mathrm{e}} = U\left|0\right\rangle\left\langle 0\right| U^\dagger\right\}$ with $\{U\} = \{I_{\mathrm{I}}, X_{\mathrm{I}}^{\mathrm{prep}}(\pi), Y_{\mathrm{I}}^{\mathrm{prep}}(\pi/2), X_{\mathrm{I}}^{\mathrm{prep}}(-$ $\{I_{\mathrm{II}}, X_{\mathrm{II}}^{\mathrm{prep}}(\pi), Y_{\mathrm{II}}^{\mathrm{prep}}(\pi/2), X_{\mathrm{II}}^{\mathrm{prep}}(-\pi/2)\}$, and each input state yields a Pauli set $\{\langle P_{\mathrm{k}}^{\mathrm{e}}\rangle = Tr\left(\rho_{\mathrm{in}}^{\mathrm{e}} P_{\mathrm{k}}^{\mathrm{e}}\right)$ with $\{P_{\mathrm{k}}^{\mathrm{e}}\} = \{I_{\mathrm{I}}, X_{\mathrm{I}}^{\mathrm{e}}, Y_{\mathrm{I}}^{\mathrm{e}}, Z_{\mathrm{I}}\} \otimes \{I_{\mathrm{II}}, X_{\mathrm{II}}^{\mathrm{e}}, Y_{\mathrm{II}}^{\mathrm{e}}, Z_{\mathrm{II}}\}$, $X^{\mathrm{e}} = Y^{\mathrm{tomo}}(-\pi/2)^\dagger \sigma_z Y^{\mathrm{tomo}}(-\pi/2)$, and $Y^{\mathrm{e}} = X^{\mathrm{tomo}}(\pi/2)^\dagger \sigma_{\mathrm{z}} X^{\mathrm{tomo}}(\pi/2)$. Figure S5.1 shows the best fit of the modelled $\{\langle P_k^e\rangle\}$ set to the measured input Pauli sets, yielding $\varepsilon_{\mathrm{I}}^{\mathrm{prep}} = -1°$, $\varepsilon_{\mathrm{II}}^{\mathrm{prep}} = -3°$, $\eta_{\mathrm{I}}^{\mathrm{prep}} = 3°$, $\eta_{\mathrm{II}}^{\mathrm{prep}} = 4°$, $\delta_{\mathrm{I}}^{\mathrm{prep}} = -6°$, $\delta_{\mathrm{II}}^{\mathrm{prep}} = -3°$, $\eta_{\mathrm{I}}^{\mathrm{tomo}} = -6°$, $\eta_{\mathrm{II}}^{\mathrm{tomo}} = -4°$, $\lambda_{\mathrm{I}}^{tomo} = 12°$, $\lambda_{\mathrm{II}}^{\mathrm{tomo}} = 5°$, $\xi_{\mathrm{I}} = 1°$, $\xi_{\mathrm{II}} = -2°$, and $\mu_{\mathrm{I}} = \mu_{\mathrm{II}} = -11°$.

Knowing the tomographic errors and thus $\{\langle P_{\mathrm{k}}^{\mathrm{e}}\rangle\}$, we then invert the linear relation $\{\langle P_{\mathrm{k}}^{\mathrm{e}}\rangle = Tr\left(\rho P_{\mathrm{k}}^{\mathrm{e}}\right)\}$ to find the 16×16 matrix B that links the vector $\overrightarrow{\langle P_{\mathrm{k}}^{\mathrm{e}}\rangle}$ to the columnized density matrix $\overrightarrow{\rho}$, i.e. $\overrightarrow{\rho} = B.\overrightarrow{\langle P_{\mathrm{k}}^{\mathrm{e}}\rangle}$. The matrix B is finally applied to the measured sixteen input and sixteen output Pauli sets to find the sixteen $(\rho_{\mathrm{in},}, \rho_{\mathrm{out}})_{\mathrm{k}}$ couples to be used for calculating the gate map.

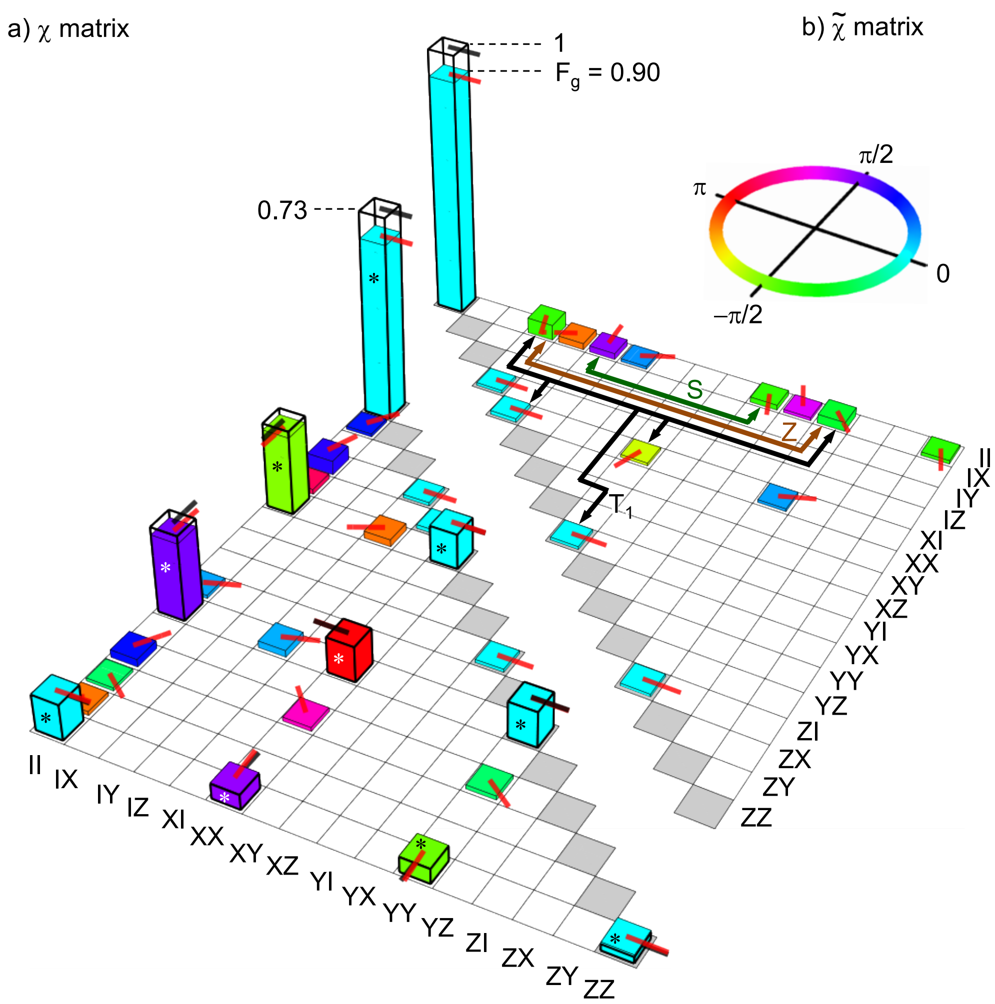
a) χ matrix
b) $\tilde{\chi}$ matrix
1
F_g = 0.90
0.73
π/2
π
0
−π/2
S
Z
T_1
II
IX
IY
IZ
XI
XX
XY
XZ
YI
YX
YY
YZ
ZI
ZX
ZY
ZZ

Figure 5.10

Chapter 6

Running the Grover Search Algorithm

This chapter will describe the experimental implementation of the so-called *Grover search algorithm* with our two-qubit quantum processor. The first section will provide a short introduction of the algorithm and motivate the interest in realizing it. The following sections will then discuss the details of the experimental realization of this algorithm. We will discuss the results that we obtained and compare the algorithm fidelity and runtime to that of an equivalent, classical algorithm. Finally, we will analyze all relevant errors made in our experiment.

6.1 Introduction & Motivation

Search algorithms are of great importance in many domains of mathematics and computer science. One such search problem that often arises and which will be discussed in the following sections can be formulated in simple terms as follows:

Theorem 6.1. Assume that we have a search space $\mathcal{S}$ that consists of a finite number N of states $s \in \mathcal{S}$. The solution to our search problem corresponds to a subset of M states of the search space $\mathcal{T} \subset \mathcal{S}$. We can then define a search function $\mathcal{C}(s) : \mathcal{S} \to \{0, 1\}$ that discriminates between states that solve the search problem and states that don't, such that $\mathcal{C}(s) = 1$ for $s \in \mathcal{T}$ and $\mathcal{C}(s) = 0$ otherwise.

Using this definition of the search problem, the goal of a search algorithm is to find all states $t \in \mathcal{S}$ for which $\mathcal{C}(t) = 1$. In the following sections, for the sake of simplicity we will assume in the following sections that the solution set $\mathcal{T}$ contains only one single state t. This special case can easily be generalized to cases where more than one solution exists to the search problem.

The first step in order to solve a search problem of the kind described above is to map the problem above to a form suitable for solution by a digital (quantum) computer. For this, we first number and encode the N input states $s_i \in \mathcal{S}$ in binary form such that

$s_i = \sum_{j=0}^{l} s_{ij} 2^j$, where l is the minimum required length of a binary register that can hold all N input states. With this definition, it is then also trivial to reformulate $\mathcal{C}$ such that the function operates on a binary input register instead of the original input states.

Using these assumptions and definitions, it can then be shown that the most efficient classical search algorithm for solving the search problem above will use $\mathcal{O}(N)$ calls of the function $\mathcal{C}$ to find the solution t of the search problem. Assuming that the time to evaluate the function $\mathcal{C}$ is far superior to the time needed to perform any other operation during the search algorithm, the number of calls to $\mathcal{C}$ also corresponds approximately to the runtime of the whole search algorithm.

Amazingly, in 1997, Lev Grover found a quantum algorithm that could solve exactly the same search problem with only $\mathcal{O}(\sqrt{N})$ calls to the function $\mathcal{C}$ (Grover, 1997). His algorithm achieves this by repeatedly calling a quantum-mechanical implementation of the function $\mathcal{C}$ with a highly superposed qubit state and applying a special operator to the output state afterwards. The individual steps of the algorithm are straightforward and are given as follows:

1. Initialize a qubit register to the state $|\psi\rangle = |0\rangle$ (corresponding to a binary input state $|0000\ldots0_B\rangle$)

2. Apply the generalized Hadamard operation to the qubit register, producing a fully superposed quantum state
$$|\psi\rangle = \frac{1}{\sqrt{N}} \sum_{i=0}^{N-1} |i\rangle$$

3. Repeat the following sequence $\mathcal{O}(\sqrt{N})$ times:

   a) Apply the *Oracle operator* $|i\rangle \rightarrow (-1)^{\mathcal{C}(i)} |i\rangle$ to the state $|\psi\rangle$

   b) Apply the *diffusion operator* $|i\rangle \rightarrow -|i\rangle + \frac{2}{N} \sum_{i=0}^{N-1} |j\rangle$ to the state $|\psi\rangle$

4. Measure the state of the quantum register

Here, we have enumerated the states of the qubit register from $|0\rangle$ to $|N-1\rangle$. Basically, the Grover algorithm makes use of quantum parallelism to solve the search problem $\mathcal{O}(\sqrt{N})$ times faster than the most efficient classical algorithm. To understand better its strategy used to solve the search problem, the different steps of the algorithm can be rephrased in the following, more intuitive way:

- First, it creates a fully superposed quantum state which contains all possible solutions to the search problem at once. The amplitudes and phases of each individual state are all equal in the beginning.

- Then, it applies the so-called Oracle operator to this superposed state. The effect of the Oracle is to turn the phase of the states t for which $\mathcal{C}(t) = 1$ by an angle π. As will be shown later, such an Oracle operator can be implemented in a straightforward way for any classical search function.
- In the next step, it applies a diffusion operator to the quantum state which transfers a fraction of the amplitude from states with zero phase to the turned states, increasing thus the amplitude of the latter. In this process, the phases of all states also get turned back to zero, allowing the algorithm to repeat the sequence above.
- Repeating these two operations increases the amplitude of the states that correspond to a solution of the search problem until the amplitudes of all the other states are zero. After that point, the process reverses and the amplitude is transferred back to the original states. It is therefore crucial to stop the repetition sequence given above after the right number of iterations.

By implementing the search function as a quantum operator, the Grover algorithm is able to evaluate it in one single call for all possible input states. This so-called *quantum parallelism* provides the basis for the speed-up of the search in comparision to a classical algorithm. However, being able to encode the result of the search function in the phase of a multi-qubit state does not directly translate to a speed advantage since it is usually very hard to extract this phase information from the quantum state. Indeed, to extract the values of all phases from an N-qubit state, it is necessary to perform $\mathcal{O}(2^N)$ measurements on an ensemble of identically prepared quantum states. However, extracting the state amplitudes from such a state takes only $\mathcal{O}(N)$ measurements, which in addition can usually be carried out in parallel. It is for this that the Grover algorithm uses an operator that transforms the information encoded in the phases of the qubits to an information encoded in their amplitude. However, since the conversion between phase to amplitude information through the application of an unitary operator is limited by certain physical constraints, the algorithm needs to repeat the encode-and-transfer sequence described above $\mathcal{O}(\sqrt{N})$ times.

To analyze further the constraints and principles of the algorithm, we will discuss a more detailed derivation of it starting from the Schrödinger equation and we will also explain what limits the efficiency of the phase-to-amplitude conversion in the algorithm.

6.1.1 Deriving the Grover Algorithm from Schrödinger's Equation

An interesting derivation of the Grover algorithm algorithm starting from Schrödinger's equation has been detailed by Grover himself in a seminal paper (Grover, 2001) and shall be briefly rediscussed here since it sheds light on the basic principles on which the algorithm is based. The derivation begins by considering a quantum system governed by Schrödinger's equation, which can be written as (omitting all physical constants)

$$-i\frac{\delta}{\delta t}\psi(x,t) = \frac{\delta^2}{\delta x^2}\psi(x,t) - V(x)\psi(x,t) \tag{6.1}$$

Here $\psi(x,t)$ describes the wave-function and V is a time-indepenent potential. Let us assume that the potential $V(x)$ is shaped as in fig. 6.1, i.e. possessing a local minimum of energy. When one initializes the system to a state $\psi_0(x,t_0)$ and lets it evolve for a given time, $\psi(x,t)$ will be attracted by the minimum of potential energy and "fall into it" much like a classical particle in such a potential would[1]. Ony might thus ask if one could encode the solution to a search problem as a point of minimum energy x_0 of a potential $V(x)$, take an initial state $\psi_0(x,t_0)$ and let it evolve into a state that has a high probability around x_0, thereby solving the search problem. To answer this question it is first necessary to discretize the wavefunction $\psi(x,t)$ such that it can represent the search problem stated in the last chapter, which is defined over a finite number of states. In the most simple case, we can use a regular grid of points x_i with a spacing dx for this, as shown in fig. 6.1b. Discretizing the time evolution of eq. 6.1 in steps dt as well and defining $\epsilon = dt/dx^2$, we obtain a new equation of the form

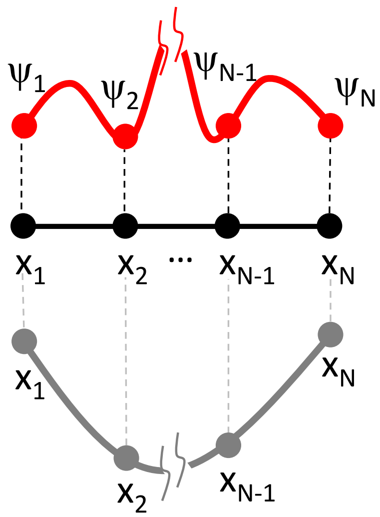

Figure 6.1: A wavefunction $\psi(x)$ and potential $V(x)$ defined on a grid of points $x_1,\ldots,x_N$.

$$-\frac{\psi_i^{t+dt}-\psi_x^t}{dt} = \frac{\psi_{i+1}^t+\psi_{i-1}^t-2\psi_x^t}{dx^2} - V(x_i)\psi_i^t \tag{6.2}$$

where we have written $\psi(x_i,t)=\psi_i^t$. For a circular grid with N points we can write this equation in matrix form as

$$\vec{\psi}^{t+dt} = S^t\cdot\vec{\psi}^t \tag{6.3}$$

[1]of cource, since there is no dissipation, the state will not come to rest at the minimum point of energy but rather oscillate around it conserving its total potential and kinetic energy

with S being a state transition matrix of the form

$$S = \begin{pmatrix} 1-2i\epsilon - iV(x_1)dt & i\epsilon & 0 & \dots & i\epsilon \\ i\epsilon & 1-2i\epsilon - iV(x_2)dt & i\epsilon & \dots & 0 \\ 0 & i\epsilon & \ddots & & \vdots \\ \vdots & & & \ddots & \vdots \\ i\epsilon & 0 & \dots & i\epsilon & 1-2i\epsilon - iV(x_N)dt \end{pmatrix} \tag{6.4}$$

For infinitesimal times dt we can seperate the effect of the potential $V(x)$ on the wavefunction from the spatial dispersion by writing $S \approx D \cdot R$ with

$$D = \begin{pmatrix} 1-2i\epsilon & i\epsilon & 0 & 0 & \dots & i\epsilon \\ i\epsilon & 1-2i\epsilon & i\epsilon & 0 & \dots & 0 \\ \dots & \ddots & & & & \vdots \\ i\epsilon & 0 & 0 & \dots & i\epsilon & 1-2i\epsilon \end{pmatrix} \tag{6.5}$$

and

$$R = \begin{pmatrix} e^{-iV(x_1)dt} & 0 & \dots & 0 & \\ 0 & e^{-iV(x_2)dt} & \dots & 0 & \\ 0 & \dots & & 0 & e^{-iV(x_N)dt} \end{pmatrix} \tag{6.6}$$

This approximation is correct to $\mathcal{O}(\epsilon)$ up to an unrelevant renormalization factor. We can now repeatedly apply the matrix product $D \cdot R$ to the waveunction to obtain its state after a given finite time Δt by writing

$$\vec{\psi}^{t+\Delta t} = \left(\prod_{i=1}^{\Delta t/dt} D \cdot R \right) \cdot \vec{\psi}^{t} \tag{6.7}$$

This technique of splitting up the full evolution operator into a product of two or more non-commuting operators that are applied repeatedly to the wavefunction to obtain its state after a finite time is sometimes referred to as *Trotterification* – in reference to the so-called *Lie-Trotter formula* on which it is based – and is widely in digital quantum simulation (Lloyd, 1996; Lanyon et al., 2011).

As can be seen in eq. (6.7), the evolution of the wavefunction at infinitsemial times is governed by two processes: The interaction with the potential V and a spatial dispersion process that mixes different spatial parts of the wavefunction with each other. The operator D resembles a Markov diffusion process since each row and column of the matrix sums up to unity, whereas R changes the phase of each element of the wavefunction in accordance with the local potential seen by it. If we apply R to a fully superposed initial state of the form $\psi_i = 1$ (omitting the normalization factor for clarity) and assume that $V_i = 0$ for $i \neq j$ and $V_j dt = \pi/2$ (the potential thus encoding a search function with $\mathcal{C}(j) = 1$ and $\mathcal{C}(i) = 0$ for $i \neq j$), the element ψ_j will get turned according to $\psi_j \to i\psi_j$, whereas all other elements ψ_i will remain unchanged. Applying the operator D to the resulting state will transform ψ_j according to $\psi_j \to \psi_j(i + 2\epsilon(1+i))$ with a corresponding amplitude $\sqrt{1 + 4\epsilon + \mathcal{O}(\epsilon^2)}$ and the adjacent states $\psi_{j\pm1}$ according to $\psi_{j\pm1} \to \psi_{j\pm1}(1 - \epsilon(1+i))$ with an amplitude $\sqrt{1 - 2\epsilon + \mathcal{O}(\epsilon^2)}$. Hence there is a transfer of amplitude between the state whose phase has been turned and its neighboring states. If we reset the phases of all the ψ_i to zero afterwards, we can iterate the application of $D \cdot R$ until all of the amplitude has been transferred to the element ψ_j that solves the search problem. This is, in essence, exactly what the Grover algorithm does, the only difference being that it replaces the matrix D with an unitary matrix that maximizes the amplitude transfer to the states solving the search problem, thereby speeding up the algorithm. As stated before, the efficiency with which the algorithm can transfer amplitude between different states is limited by physical constraints, in the next section we will therefore discuss exactly what limits this efficiency and which unitary matrix one should choose to maximize it.

Efficiency of Quantum “Crawling”

It is interesting to ask which is the maximum amount of amplitude that can be transferred in a single step of the Grover search algorithm and which form the matrix D should have to maximize this transfer. To answer this question and derive the ideal diffusion matrix, we will assume first that the matrix R which encodes the value of the search function $\mathcal{C}$ in the quantum state of the qubit register can be written in the most general case as

$$R = \sum_{i=0}^{N-1} \exp\left[i\alpha\mathcal{C}(i)\right] |i\rangle \langle i| \tag{6.8}$$

Here, α is a factor which we can choose arbitrarily. So, without loss of generality, we can choose $\alpha = \pi$, yielding an Oracle operator of the form

$$R = \mathrm{I} - 2\sum_{i=0}^{N-1} \mathcal{C}(i) |i\rangle \langle i| \tag{6.9}$$

This operator will flip the sign of all states for which $\mathcal{C}(i) = 1$. Now, the next step consists in finding a diffusion or state transfer matrix which will maximize the amplitude transfer to states marked by the Oracle operator above and which will also reset the phases of the quantum register to zero afterwards, such that we might apply the Oracle operator to the resulting state again. In the most general case, such a state transfer matrix will have the form

$$D_c = \begin{pmatrix} b & a & a & \dots & a \\ a & b & a & \dots & a \\ \vdots & & \ddots & & \vdots \\ a & & \dots & a & b \end{pmatrix} \tag{6.10}$$

Here, we assume that all non-diagonal elements of the matrix are equal, which is well justified since we have no knowledge of the structure of the search space of the problem and therefore want to treat all basis states equally during the phase-to-amplitude conversion. Furthermore, since both the initial quantum state and the Oracle operator as given by eq. (6.9) contain only real numbers and we demand that the quantum state after applying D_c may contain only positive real numbers it is easy to show that a, b must be real numbers. Finally, the unitarity of quantum operators demands that $D_c^\dagger D_c = \mathrm{I}$, which for the matrix above is equivalent to the two conditions

$$1 = b^2 + (N-1)a^2 \tag{6.11}$$

$$0 = 2ab + (N-2)a^2 \tag{6.12}$$

Solving these two equations for a, b yields the trivial solution $b = \pm 1$, $a = 0$ and the more interesting one $b = \pm(1 - 2/N)$, $a = \mp 2/N$. As can be checked easily, the solution $b = 1 - 2/N$, $a = 2/N$ results in a maximum amplitude transfer from states $|i\rangle$ for which $\mathcal{C}(i) = 0$ to states $|j\rangle$ for which $\mathcal{C}(j) = 1$. Thus the ideal diffusion matrix to be used in the Grover algorithm is given as

$$D = \begin{pmatrix} -1+2/N & 2/N & 2/N & \dots & 2/N \\ 2/N & -1+2/N & 2/N & \dots & 2/N \\ \vdots & & \ddots & & \vdots \\ 2/N & 2/N & 2/N & \dots & -1+2/N \end{pmatrix} \tag{6.13}$$

This matrix, together with an Oracle operator R as given by eq. (6.9) will yield the maximum amplitude transfer from states not solving the search problem to states that solve it. Repeating the application of $D \cdot R$ on an initially fully superposed quantum states for $\mathcal{O}(\sqrt{N})$ times will transform the input state to a state containing only the solutions of the search problem, thus solving the problem quadratically faster than would be possible with any classical algorithm.

To be able to compare the Grover algorithm as outlined here to a classical version solving the same search problem, we will now discuss another variant of the algorithm using an ancilla qubit to encode the result of the search function. This implementation will make it possible to devise a classical algorithm that can then be compared to the quantum algorithm discussed here. In the discussion in following sections we will focus

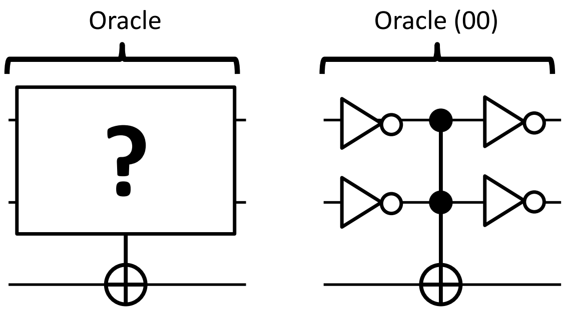

Figure 6.2: a) Ancilla-based implementation of the Oracle function $\mathcal{C}$. The state of the third bit get flipped if the search function $\mathcal{C}(i) = 1$ for the given input state i. b) An example of an ancilla-based search function that returns a true value for the input state 00.

entirely on the two-qubit case, which is the case most relevant to this work.

6.1.2 Ancilla-based Implementation of the Algorithm

The implementation of the Grover search algorithm outlined above encodes the value of the search function $\mathcal{C}$ in the phase of the input state supplied to this function. This makes it hard to compare the algorithm to a classical search algorithm which operates on a binary input states and, in general, cannot encode the result of the search function directly in the input state. It is therefore useful to formulate a version of the Grover algorithm where the Oracle function does not directly encode the marked state in the input qubit register but rather uses an ancialla qubit to store the result of calling $\mathcal{C}$. Such a representation of the algorithm is very useful since it can be directly compared to a classical algorithm implemented with reversible logic gates, thus making it possible to benchmark our algorithm against a classical counterpart.

Exemplary implementations of ancilla-based search functions $\mathcal{C}$ implemented using reversible (quantum) gates are shown in fig. 6.2 for the two-qubit case. There, a two-qubit Tofolli gate in combination with several single-qubit NOT gates (that can be easily implemented as single-qubit X_π rotations) is used to flip the state of an ancilla-qubit conditionally on the input state of the gate. Using this approach, any arbitrary classical search function $\mathcal{C}$ that can be implemented with a set of universal reversible logic gates (e.g. the Toffoli gate and the NOT gate) can be directly mapped to a corresponding quantum operator that works on quantum-mechanical input states and implements the classical search function.

Now, to use the Grover algorithm with such an ancilla-based quantum Oracle, it is neccessary to re-encode the result of the Oracle in the qubit input state. Fig. 6.3 shows a version of the two-qubit Grover algorithm that achieves exactly this by using a three-qubit control-not (CNOT) gate C of the form

$$C = \mathrm{I}^{n\otimes n} - 2\sum_{ij} |ij1\rangle \langle ij1| \tag{6.14}$$

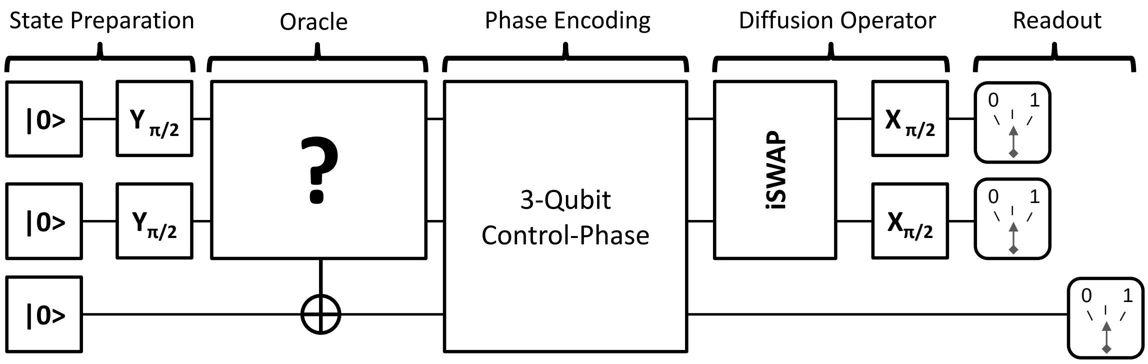

Figure 6.3: A full version of an ancilla-based implementation of the two-qubit Grover search algorithm. The algorithm works on a two-qubit input state and flips the state of a control qubit for one of the four possible input states in accordance to an unknown Oracle function. It then applies a 3-qubit control-phase operation of that maps $|xx1\rangle \to -|xx1\rangle$, $|xx0\rangle \to |xx0\rangle$ to encode the state of the control qubit directly in the two input qubits and then uses a diffusion operator to determine the state which has been marked by the Oracle function.

to phase-encoded the state of the anciall qubit in the state of the input qubit register. After the re-encoding of the result, the ancilla qubit is not needed during the remainder of the algorithm and must not be read out before the algorithm terminates.

6.2 Comparision to a Classical Algorithm

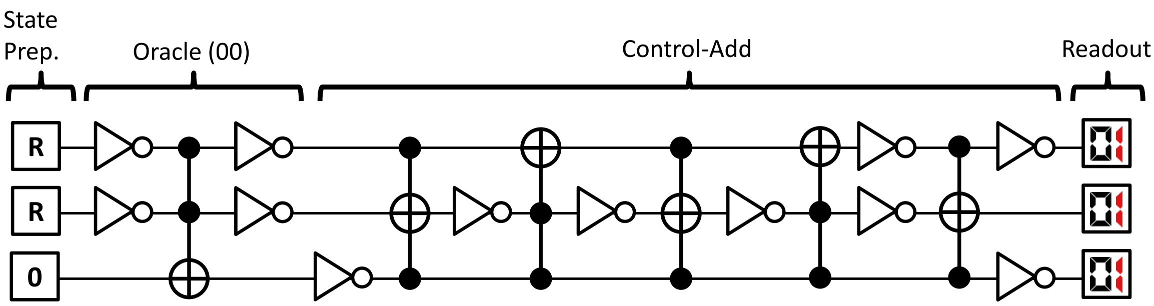

Figure 6.4: Classical reversible implementation of a search algorithm on a two-bit input register. The Oracle function can be implemented by two single-bit NOT operations and a Toffoli gate. R designates the generation of a random binary value at the beginning of the algorithm. If the Oracle does not yield the correct answer, the test state is incremented. The average success probability of the algorithm is 50 %.

In order to quantify the quantum speed-up achieved by a quantum algorithm it is necessary to map the problem it solves to an equivalent problem that can be solved by a classical algorithm. For the Grover algorithm, this is the search problem that we discussed in the first section of this chapter. Now, with the ancilla-based version of the Grover algorithm introduced in the last section it is possible to directly formulate a classical algorithm that solves the same problem and compare the efficiency of the two. We can use reversible logic gates such as the Toffoli gate and the single-(qu)bit NOT gate to implement the classical algorithm, thereby achieving a maxmimum comparability with the quantum version. Since the two-qubit Grover algorithm evaluates the search function $\mathcal{C}$ only once it is interesting to ask what would be the performance of an equivalent classical algorithm which calls $\mathcal{C}$ once and returns an estimate of the state solving the search problem. Such an algorithm is shown in fig. 6.4. It achieves a success probability of 50 % by evaluating the function $\mathcal{C}$ for a randomly generated two-bit input value r and returning r if it found $\mathcal{C}(r) = 1$ or $r + 1 (\mathrm{mod}\ 4)$ otherwise. The 50 % success rate of this algorithm provides a benchmark against which we will measure the speed-up of our implementation of the Grover algorithm.

6.3 Experimental Implementation

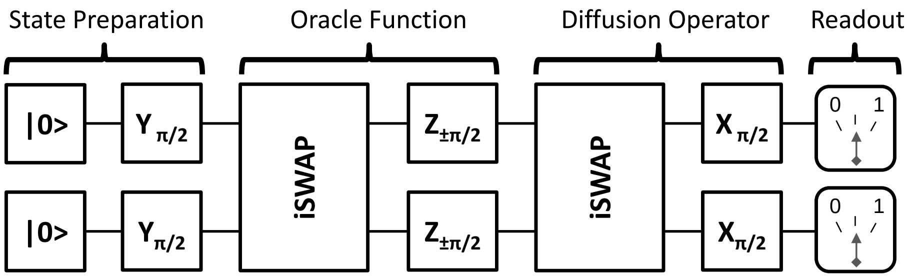

Figure 6.5: Schematic of our implementation of the Grover search algorithm. The algorithm consists in generating a fully superposed input state, applying the Oracle function to it and analyzing the resulting state by applying the Diffusion transform to it and reading out the value of the qubit register afterwards.

In this work we implement a compiled version of the two-qubit Grover algorithm. The gate sequence of the algorithm is shown in fig. 6.5 and consists in two $i\mathrm{SWAP}$ gates and six single-qubit gates applied to an initial state $|00\rangle$. The first $i\mathrm{SWAP}$ gate together with the two single-qubit $Z_{\pm\pi}$ rotations implements the Oracle function $f(x)$ as given in eq. (6.9), where the signs of the rotation operations determines the state which is marked and can be either $|00\rangle$ (corresponding to a $Z^1_{-\pi/2} \cdot Z^2_{-\pi/2}$ rotation), $|01\rangle$ ($Z^1_{-\pi/2} \cdot Z^2_{\pi/2}$), $|10\rangle$ ($Z^1_{\pi/2} \cdot Z^2_{-\pi/2}$) or $|11\rangle$ ($Z^1_{\pi/2} \cdot Z^2_{\pi/2}$). The second $i\mathrm{SWAP}$ operation together with the following $X^1_{\pi/2} \cdot X^2_{\pi/2}$ operation implements the difussion operator as given by eq (6.13). The final step of the algorithm consists in reading out the two-qubit register.

6.3.1 Pulse Sequence

To implement the gate sequence described above we need to realize a sequence of microwave and flux pulses which realize the individual quantum gates of the sequence. To eliminate possible gate errors, we perform a series of calibration measurements before to tune-up the individual single- and two-qubit gates needed for the algorithm. In addition, we run individual parts of the algorithm successively and perform quantum state tomography to characterize the state of the quantum register after each step of the algorithm and correct the gate operations applied to the qubit in order to maximize the fidelity of the measured states in respect to the ideal ones. Fig. 6.6 shows an experimental pulse sequence for the Grover algorithm with an Oracle operator marking the state $|00\rangle$. Shown are the frequencies of the two qubits during the runtime of the algorithm and the microwave drive and readout pulses applied to them.

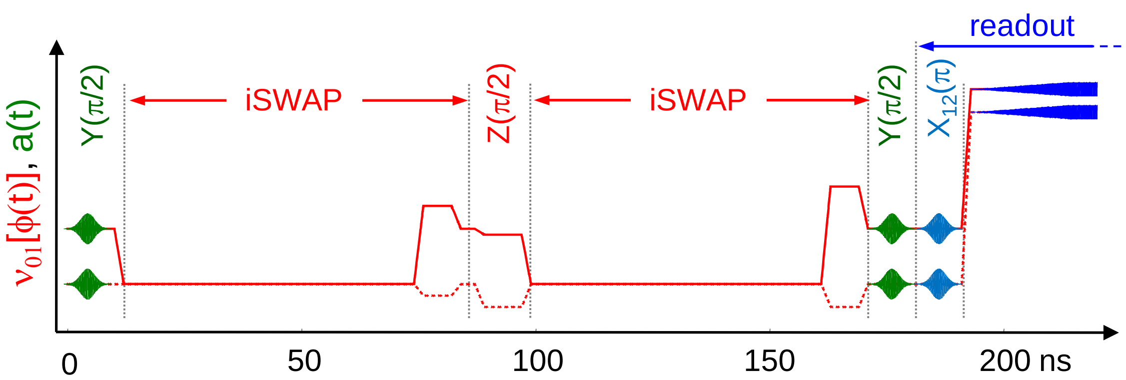

Figure 6.6: The pulse sequence used in realizing Grover's quantum search algorithm. First, a $Y_{\pi/2}$ pulse is applied to each qubit to produce the fully superposed state $1/2(|00\rangle + |01\rangle + |10\rangle + |11\rangle)$. Then, an $i\mathrm{SWAP}$ gate is applied, followed by a $Z_{\pm\pi/2}$ gate on each qubit, which corrsponds to the application of the oracle function. The resulting state is then analyzed using another $i\mathrm{SWAP}$ gate and two $X_{\pi/2}$ gates to extract the state which has been marked by the oracle function. Optionally, a Y_{π}^{12} pulse is used on each qubit to increase the readout fidelity.

6.4 Results

Here we discuss the results obtained when running the Grover search algorithm with our two-qubit processor. In the first section we will analyze the quantum state of the qubit register during the algorithm by performing quantum state tomography. In the second section we will present and discuss the single-run results obtained in our experiment.

6.4.1 State Tomography of the Algorithm

Fig. 6.7 shows the results when running the Grover search algorithm for the four possible Oracle functions. Shown are quantum state tomographies after each step of the algorithm and the single-run results obtained when measuring the qubit register after the final step of the algorithm. In subfigures (a)-(d) The black outlined circles in the density matrices represent the ideal theoretical states, whereas the colored, solid circles represent the experimentially measured states. The trace fidelities of all states with the ideal ones are noted above each density matrix. As can be seen, the fidelity diminshes as a function of the runtime of the algorithm due to dephasing and relaxation of the qubit register. The experimental single-shot probabilities in subfigure (e) are shown along with the expected probabilities, which are calculated based on the readout matrix of our two-qubit system and the state tomographies after the final state of the algorithm.

6.4.2 Single Run Results

The experimental state tomographies discussed in the last section show that we are able to implement the Grover search algorithm with adequate fidelity using our two-qubit processor. However, the analysis of the two-qubit register by quantum state tomography at the end of the algorithm does not prove that we can achieve real quantum speed-up with our processor. For this, it is necessary to directly read out the state of the qubit register at the end of the algorithm *without* performing any kind of error correction afterwards. By looking at this “raw” outcome data and averaging it over many identical runs of the processor we can then quantify the success rate and the fidelity of the algorithm we implemented. The results of such measurements that we performed for the four possible Oracle functions is shown in fig. 6.8. Besides the single-run probabilities for all four Oracle functions, the diagram also shows for comparision the expected outcome probabilities that are calculated based on the quantum state tomographies discussed above and the readout matrix of the two-qubit system. As can be seen, the agreement between the measured and calculated probabilities is quite good. The dashed line in the diagrams corresponds to the success probability of a classical “query-and-guess” algorithm as described above, which is bound to 50 % and provides the benchmark against which we measure the quantum speed-up in this system. As can be seen, our implementation of the Grover search algorithm outperforms a classical search algorithm for all four Oracle functions, if only by a small margin.

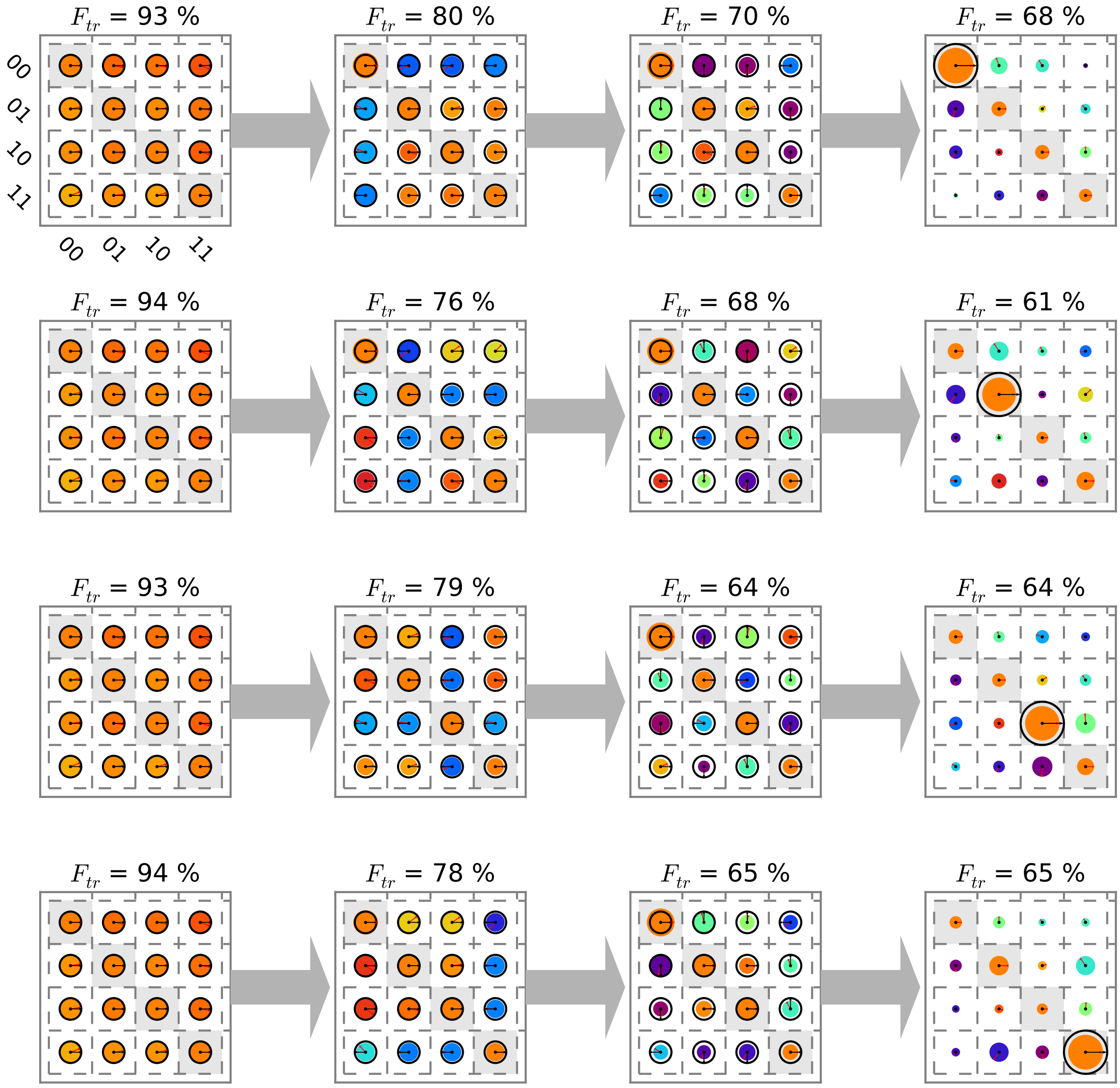

Figure 6.7: Quantum state tomographies at different steps of the Grover search algorithm. The density matrices show the experimentally measured states in color and the theoretical states in black. For each state, the trace fidelity $F_{tr}(\rho_A, \rho_B) = \mathrm{Tr}\{\rho_A \cdot \rho_B\}$ is shown above the density matrix.

6.5 Algorithm Fidelity

We can define the average fidelity of the algorithm in a single run, which corresponds to the averaged success probabilities measured for all four Oracle functions and averaged over a large sample set. Table 6.1 shows these single-run probabilities along with the so-called *user fidelities*, which are given as

$$f_{ab} = p(|ab\rangle\,|ab) = \frac{p(ab|\,|ab\rangle)}{\sum_{uv} p(uv|\,|uv\rangle)} \tag{6.15}$$

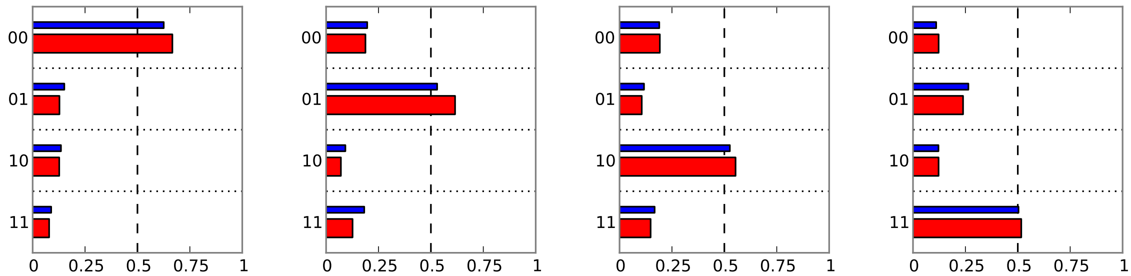

Figure 6.8: The single-run success probabilities of our implementation of the Grover search algorithm. Shown are the averaged probabilities for the four possible Oracle functions. The red bars correspond to measured values, the blue ones to expected probabilities calculated using the reconstructed density matrices after the final step of the algorithm and the measured two-qubit readout matrix. The dashed line indicates the average success probability of a classical query-and-guess algorithm for comparision.

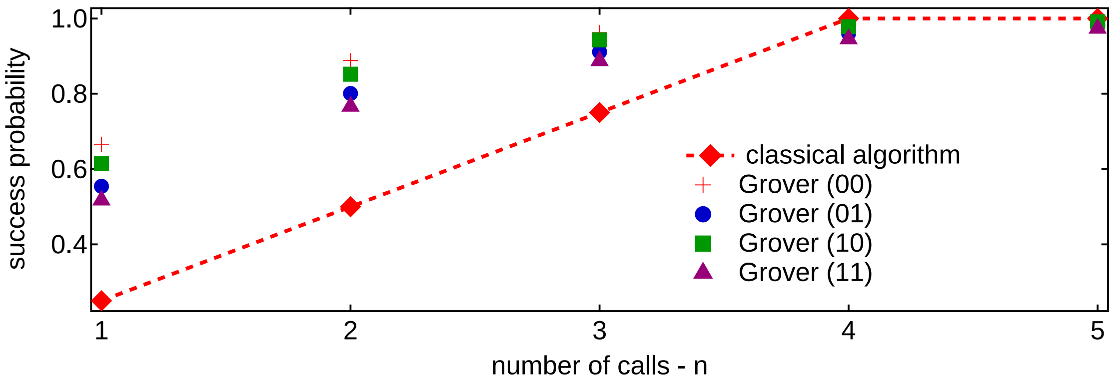

Figure 6.9

and correspond to the probability of having obtained the correct answer given a certain outcome, averaged over all four possible Oracle functions. For all four, both the single-run and user fidelities are $> 50\%$, hence demonstrating quantum speed-up in comparision with a classical query-and-guess algorithm as discussed above.

$ab/\|uv\rangle$	$\|00\rangle$	$\|01\rangle$	$\|10\rangle$	$\|11\rangle$	$\sum$	f_{ab}
00	0.666	0.192	0.188	0.122	1.168	57.0 %
01	0.127	0.554	0.071	0.122	0.874	63.4 %
10	0.128	0.106	0.615	0.239	1.088	56.5 %
11	0.079	0.148	0.126	0.517	0.870	59.4 %

Table 6.1: Conditional probabilities $p_{ab/|uv\rangle}$ and statistical fidelities f_{ab} for all possible outcomes ab, measured for our version of Grover's algorithm.

6.6 Error Analysis

There are three kind of errors arising in our implementation of the Grover search algorithm that we will analyze in the following section. These errors are:

1. Deterministic, unitary gate errors
2. Stochastic errors introduced due to qubit decoherence during the runtime of the algorithm
3. Readout errors due to qubit relaxation during the readout of the qubit state, insufficient coupling between the qubit and the readout or retrapping of the readout state during measurement

We will analyze the contributions of all these three error sources for the implementation of the algorithm below.

6.6.1 Gate Errors & Decoherence

Gate errors are unitary errors that arise due to misshaped or mistuned gate pulses. Usually the effect of these errors is combined with stochastic, non-unitary errors arising due to qubit decoherence during the runtime of the algorithm and therefore has to be analyzed together with the latter. Hence, in order to quantify these errors it is necessary to generate an error model of our algorithm that takes into account both unitary as well as non-unitary errors and whose parameters we obtain by fitting the model to our experimental results. Repeating this procedures for the experimental runs implementing the four different Oracle functions we obtain a full quantitative error model for all of them.

Modeling Decoherence

We could again model decoherence processes in our algorithm by formulating an effective master equation of the two-qubit system that includes relaxation and dephasing processes as we did when anylyzing the universal quantum gate that we implemented. For our implementation of the Grover algorithm, however, we chose to rather use a set of discrete decoherence operators that model amplitude (i.e. T_1) and phase daming (i.e. T_ϕ) processes and which we can directly integrate in a more simple, operator-based model of the algorithm. We can then model the decoherence in our algorithm by applying these operators to the calculated quantum states after each individual step of the algorithm. Like this we can generate an error model incorporating the most relevant experimental decoherence processes without the need to numerically integrate an effective master equation, thereby greatly speeding up the process of fitting our experimental data to the formulated error model. In the following paragraphs we introduce the reader to the operators we use to model relaxation and dephasing processes in our error model.

To model qubit relaxation, we can use a pair of single-qubit operators describing amplitude-daming of the qubit state, which given as (Michael A. Nielsen and Isaac L. Chuang, 2000)

$$E_1^{T_1} = \begin{pmatrix} 1 & 0 \\ 0 & \sqrt{1-\gamma_{T_1}} \end{pmatrix} \qquad E_2^{T_1} = \begin{pmatrix} 0 & \sqrt{\gamma_{T_1}} \\ 0 & 0 \end{pmatrix} \tag{6.16}$$

On the other hand, phase-daming operators describing qubit dephasing can be written analogously as

$$E_1^{T_{\phi 1}} = \begin{pmatrix} 1 & 0 \\ 0 & \sqrt{1-\gamma_{\phi}} \end{pmatrix} \qquad E_2^{T_{\phi 1}} = \begin{pmatrix} 0 & 0 \\ 0 & \sqrt{\gamma_{\phi}} \end{pmatrix} \tag{6.17}$$

Both operators are applied to a quantum state ρ according to

$$\rho \to E_1 \rho E_1^\dagger + E_2 \rho E_2^\dagger \tag{6.18}$$

and yield a trace-preserving, non-unitary evolution of the quantum state of ρ. The decoherence fraction γ that is used in the operators can be calculated from the corresponding relaxation and dephasing rates as $\gamma_{T_{1,2}}(t) = 1 - \exp\left(-t\Gamma_{1,2}^{T_1}\right)$ and $\gamma_{\phi_{1,2}} = 1 - \exp\left(-t\Gamma_{1,2}^{T_\phi}/2\right)$, where t is the time during which the state is exposed to the given decoherence process.

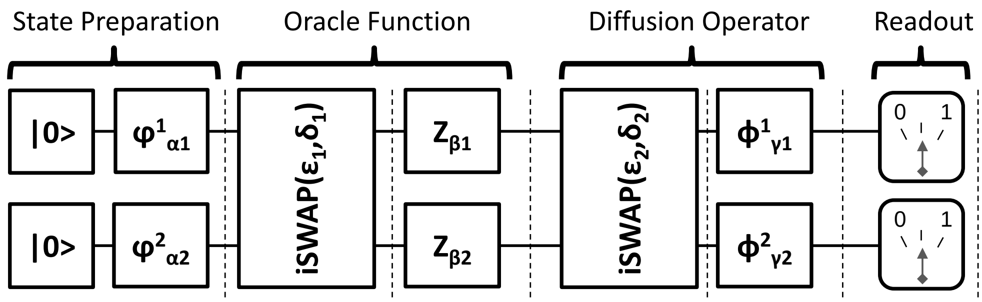

Figure 6.10: The error model we use to analyze the different gate and decoherence errors present when running the Grover search algorithm. The dotted lines indicate the points at which the quantum state has been measured by state tomography.

Using these two operators combined with a set of unitary operators describing the quantum operations performed during the algorithm we formulate a full error model that we use to model our experimental data, as shown in fig. 6.10. This model takes into account the following error sources:

- **Energy relaxation and phase decoherence**: Energy relaxation and dephasing of the qubit is modeled using the processes given in eqs. (6.16) and (6.17), applying these operators with an adapted γ after each unitary operation performed during the algorithm.
- **Single-qubit gate errors**: We model rotation angle and rotation phase errors of our single-qubit X_α and Y_α gates by replacing them with operators of the form $X_\alpha \to \phi_{\alpha'} = \cos\phi X_{\alpha'} + \sin\phi Y_{\alpha'}$ and $Y_\alpha \to \varphi_{\alpha'} = \sin\varphi X_{\alpha'} + \cos\varphi Y_{\alpha'}$. For Z-type single-qubit operators we model only rotation angle errors by replacing $Z_\alpha \to Z_{\alpha'}$
- **Two-qubit gate errors:** We model both detuning and gate-length errors of our $i\mathrm{SWAP}$ 2-qubit gates.

For the two-qubit gates, we model the errors present in the $i\mathrm{SWAP}$ operation by using the model

$$i\mathrm{SWAP}(t,\Delta) = \begin{pmatrix} 1 & 0 & 0 & 0 \\ 0 & \cos tg_e - i\frac{\Delta}{g_e}\sin tg_e & i\frac{g}{g_e}\sin tg_e & 0 \\ 0 & i\frac{g}{g_e}\sin tg_e & \cos tg_e + i\frac{\Delta}{g_e}\sin tg_e & 0 \\ 0 & 0 & 0 & 1 \end{pmatrix} \tag{6.19}$$

where $g_e = \sqrt{g^2 + \Delta^2}$ is the effective swap frequency at a qubit frequency detuning $f_{01}^1 - f_{01}^2 = 2\Delta$. Often it is pratical to replace t and Δ with $\beta = tg_e$ and $\delta = \Delta/g$. Using this notation of the iSWAP gate and the definition of the single-qubit gates as discussed before, the full algorithm with gate errors can be written as (for right-multiplication)

$$\mathrm{Grover} = \phi_{\gamma_1}^1 \otimes \phi_{\gamma_2}^2 \cdot i\mathrm{SWAP}(\epsilon_2, \delta_2) \cdot Z_{\beta_1} \otimes Z_{\beta_2} \cdot i\mathrm{SWAP}(\epsilon_1, \delta_1) \cdot \varphi_{\alpha_1}^1 \otimes \varphi_{\alpha_2}^2 \tag{6.20}$$

In addition, we add a dephasing and relaxation error after each step of the algorithm to model the decoherence during the runtime of the algorithm. Numerical optimization is then used to produce a fit of all the gate errors, which is shown in tab. 6.2. Here, the qubit relaxation and dephasing times were measured independently and are not part of the fit.

The resulting fitted error models obtained for our experimental data are shown in tab. 6.2. As can bee seen, the phase and gate-time errors for the first gates are comparatively small and grow bigger during the following steps of the algorithm. Curiously, the phase errors are bigger for the states $|10\rangle$ and $|11\rangle$, as are the gate-length errors for the two $i\mathrm{SWAP}$ gates used in the algorithm. This fact might be explained by a drift of the

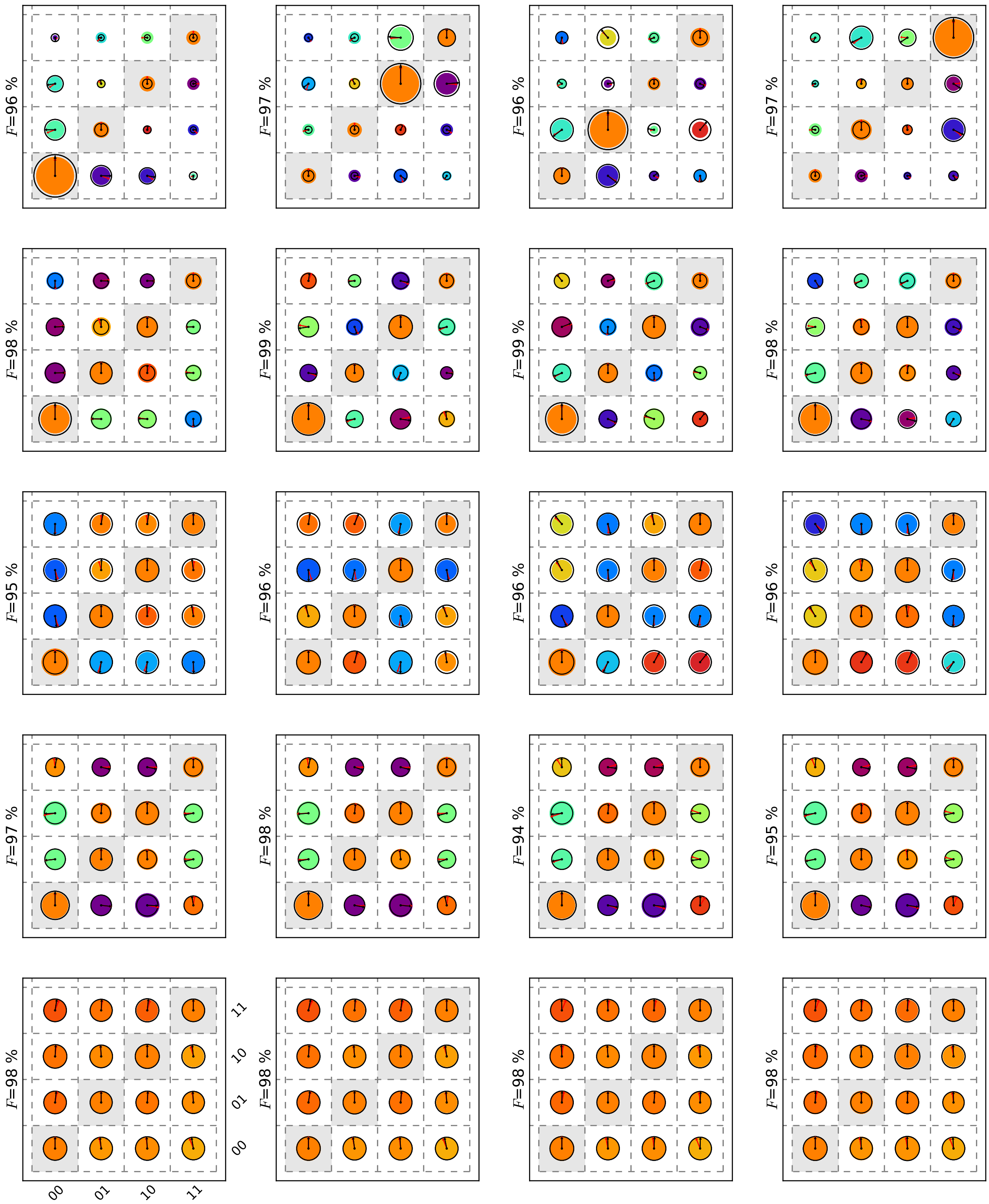

Figure 6.11: Comparision of the fitted error model as given by eq. (6.20) to our experimental data. Experimental data is shown in color, the fitted density matrices as black outlines. As before, we show the state fidelity according to eq. (**??**) between experimental and fitted states.

state	δ_1	δ_2	α_1	α_2	φ_1	φ_2	ϵ_1	β_1	β_2	ϵ_2	γ_1	γ_2	ϕ_1	ϕ_2
$\lvert 00\rangle$	0.06	-0.06	-2.5	2.7	6.1	3.1	-7.3	-3.3	-4.1	7.5	29	9.3	0.66	-1.7
$\lvert 01\rangle$	0.04	-0.3	-0.1	0.1	7.9	3.6	-11	-5.9	2.2	-6.9	28	-19	9	2
$\lvert 10\rangle$	0.09	-0.2	-3.1	1.7	1	-2.5	-6.5	-15	-22	-7.5	-15	32	3.6	5.2
$\lvert 11\rangle$	0.16	0.13	-6	3.9	2.2	0.9	-9.5	-20	-15	17	-12	-32	-7	-8.9

Table 6.2: Fitted error parameters for the measured density matrices, modeled according to the error model given in eq. (6.20). Alle angles are given in deg.

operating point of our microwave setup during the time it took to take the data for the four possible Oracle operators, during which the parameters of individual qubit gates were not recalibrated.

Fig. 6.11 shows again the measured density matrices for our realization of the Grover search algorithm, this time overlaid with the numerically optimized error model according to eq. (6.20). As can be seen, our error model is able to capture most of the observed experimental errors and can reproduce to very good accuracy the observed density matrices. The state fidelities according to eq. **??** between the measured density matrices and those of the fitted error model are shown above each density matrix.

Fidelity of the Oracle and diffusion operators

It is interesting to analyze the individual experimental fidelities of the Oracle and diffusion operators that make up the Grover algorithm achieved in our experiment. For this, we compare the action of the ideal operators D' and R' with that of the experimentally implemented versions D'_e and R'_e, taking the measured quantum states before applying each of the operators as input. We take then as the fidelity of each operator the average state fidelity of the measured output states as compared to the calculated ones, i.e.

$$
\begin{aligned}
F(D'_e) &= F(D'\rho_{in}D'^{\dagger}, D'_e\rho_{in}D'^{\dagger}_e) && (6.21)\\
F(R'_e) &= F(R'\rho_{in}R'^{\dagger}, R'_e\rho_{in}R'^{\dagger}_e) && (6.22)
\end{aligned}
$$

where we also make use of the state fidelity according to eq. **??**. By this method, we obtain the following experimental fidelities for the two gate operations:

Operator / State	$\lvert 00\rangle$	$\lvert 01\rangle$	$\lvert 10\rangle$	$\lvert 11\rangle$	Average
D'	92.3	93.4	94.3	91.7	92.9
R'	94.5	93.6	88.5	87.7	91.1

Table 6.3: Measured fidelities of the quantum Oracle and diffusion operators used in the Grover search algorithm according to eqs. (6.21) and (6.22). All fidelities are given in percent.

As can be seen, on average we are able to implement both the diffusion operator and the quantum Oracle with a fidelity $> 90\%$.

6.6.2 Readout Errors

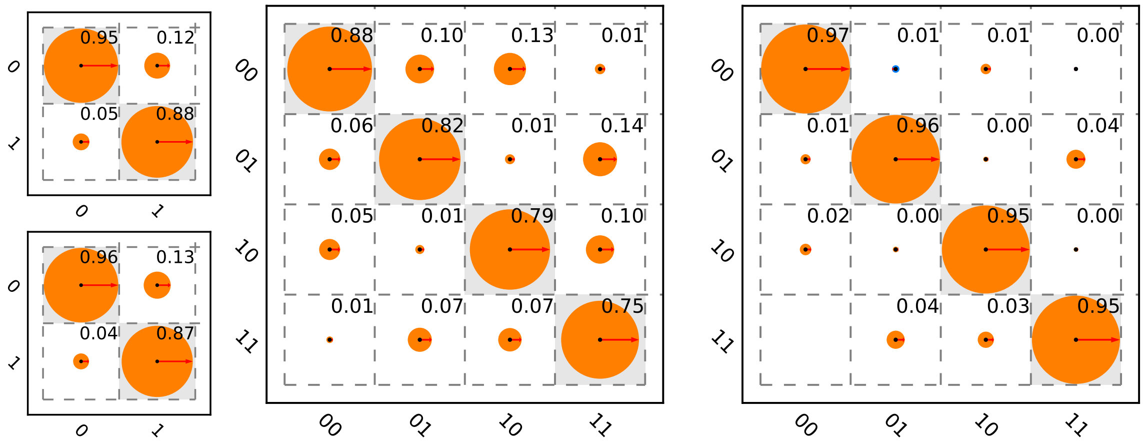

Figure 6.12: a.)The measured single-qubit readout matrices, showing the readout outcome probabilities as a function of the prepared state for both qubits. b.)The measured two-qubit readout matrix, showing again the detector outcome probabilities versus the prepared qubit states. c.) The crosstalk matrix, corresponding to the product of the inverse two-qubit readout matrix and the Kronecker product of the single-qubit readout matrices. Note that the $|1\rangle \rightarrow |2\rangle$ shelving method is used for reading out the qubit state, which increases readout fidelity but also inter-qubit readout crosstalk.

Another source of errors affecting the single-run fidelities of the algorith arises due to the imperfection of our qubit readout. Here, mostly qubit relaxation during the readout process reduces the visibility of individual qubit states and introduces errors when reading out the qubit register in the final step of the algorithm. We can easily quantify those readout errors by using the readout matrix that was introduced in the last chapter. When running the Grover algorithm we use the $|1\rangle \rightarrow |2\rangle$ shelving method described in the last chapter to increase the readout contrast and thereby the algorithm fidelity. This technique reduces single-qubit readout errors but increases inter-qubit readout crosstalk. To quantify all single-qubit and inter-qubit readout errors, we first model the readout matrix R of the two-qubit system as a product $R = R_v \cdot R_{ct}$, where R_v is the so-called *visibility matrix* and R_{ct} a matrix describing the readout crosstalk. The visibility matrix can be written as the Kronecker product $R_v = R_v^1 \otimes R_v^2$ of the two single-qubit readout matrices, which have the form

$$R_v^{1,2} = \begin{pmatrix} p_{00}^{1,2} & 1 - p_{11}^{1,2} \\ 1 - p_{00}^{1,2} & p_{11}^{1,2} \end{pmatrix} \tag{6.23}$$

Here, $p_{00}^{1,2}$ ($p_{11}^{1,2}$) corresponds to the probability to measure the value 0 (1) at the readout after having prepared the qubit in state $|0\rangle$ ($|1\rangle$). Usually, the full two-qubit readout matrix R and the single-qubit readout matrices $R_v^{1,2}$ are measured experimentially which allows us then to calculate the crosstalk matrix as $R_{ct} = R_v^{-1} \cdot R$. The three matrices measured in our experiment are shown in fig. 6.12. As can be seen, the single-qubit readout fidelities range between 87 - 96 % and the combined two-qubit readout fidelities between 75 - 85 %. Depending on the qubit state we also observe between 3-5 % inter-qubit readout crosstalk in our system.

Fig. 6.7e shows the single-run probabilities when running the Grover algorithm for the four different Oracle functions. In blue, the expected readout outcome probabilities, as calculated using the state tomography of the final states given in fig. 6.7d and the measured readout matrix of our system are shown along the measured readout outcome probabilities. The readout error model shows good quantitative agreement with the measured data, with deviations most probably due to parameter drifts occured between the measurment of the quantum state tomography and the single-run experiment.

6.7 Conclusions

To summarize, we have shown that we can implement the Grover search algorithm with our quantum processor and achieve a single-run fidelity that is sufficient to demonstrate simple probabilistic quantum speed-up as compared to a classical, reversible search algorithm. The error model formulated in this chapter is able to account for most of the observed imperfections and can explain the data we observed. Unfortunately, the coherence times of our qubits does not permit the realization of more complex algorithm with this system, but nevertheless it provides a proof-of-principle of our approach to build a superconducting quantum computer with individual-qubit single shot readout.

In the following chapter, we will discuss the extension of this approach to a system of four qubits and explain different strategies for scaling up such system to an even larger number of qubits.

Chapter 7

Conclusions & Perspective

7.1 Future Directions in Superconducting QC

7.1.1 3D Circuit Quantum Electrodynamics

7.1.2 Hybrid Quantum Systems

7.1.3 Quantum Error Correction & Feedback

Appendix A

Modeling of Multi-Qubit Systems

A.1 Analytical Approach

A.1.1 Multi-Qubit Hamiltonian

A.1.2 Energies and Eigenstates

A.2 Master Equation Approach

$$\frac{d\rho}{dt} = -\frac{i}{\hbar}[H, \rho] + \sum_j \left[2L_j\ \rho\ L_j^\dagger - \{L_j^\dagger L_j, \rho\}\right] \tag{A.1}$$

A.2.1 Direct Integration

A.2.2 Monte Carlo Simulation

A.2.3 Speeding Up Simulations

Appendix B

Data Acquisition & Management

B.1 Data Acquisition Infrastructure

B.2 Data Management Requirements

B.3 PyView

B.3.1 Overview

B.3.2 Instrument Management

B.3.3 Data Acquisition

B.3.4 Data Management

B.3.5 Data Analysis

Appendix C

Design & Fabrication

C.1 Mask Design

C.2 Optical Lithography

C.3 Electron Beam Lithography

Bibliography

Blais, A., Gambetta, J., Wallraff, A., Schuster, D. I., Girvin, S. M., Devoret, M. H., and Schoelkopf, R. J. (2007). Quantum-information processing with circuit quantum electrodynamics. *Physical Review A*, 75(3):032329.

Blais, A., Huang, R., Wallraff, A., Girvin, S. M., and Schoelkopf, R. J. (2004). Cavity quantum electrodynamics for superconducting electrical circuits: An architecture for quantum computation. *Physical Review A*, 69(6):062320.

Bouchiat, V., Vion, D., Joyez, P., Esteve, D., and Devoret, M. H. (1998). Quantum coherence with a single cooper pair. *Physica Scripta*, T76(1):165.

Chiorescu, I., Nakamura, Y., Harmans, C. J. P. M., and Mooij, J. E. (2003). Coherent quantum dynamics of a superconducting flux qubit. *Science*, 299(5614):1869 –1871.

Clarke, J., Cleland, A. N., Devoret, M. H., Esteve, D., and Martinis, J. M. (1988). Quantum mechanics of a macroscopic variable: The phase difference of a josephson junction. *Science*, 239(4843):992–997.

Clauser, J. F., Horne, M. A., Shimony, A., and Holt, R. A. (1969). Proposed experiment to test local Hidden-Variable theories. *Physical Review Letters*, 23(15):880–884.

Collin, E., Ithier, G., Aassime, A., Joyez, P., Vion, D., and Esteve, D. (2004). NMR-like control of a quantum bit superconducting circuit. *Physical Review Letters*, 93(15):157005.

Cottet, A. (2002). *Implementation of a quantum bit in a superconducting circuit*. PhD thesis, Université Paris VI, Paris.

Deutsch, D. (1985). Quantum theory, the Church-Turing principle and the universal quantum computer. *Proceedings of the Royal Society of London. A. Mathematical and Physical Sciences*, 400(1818):97 –117.

Devoret, M. (1995). Quantum fluctuations in electrical circuits. In *Les Houches Session on Quantum Fluctuations*, volume LXIII, pages 351–386.

Devoret, M. H., Martinis, J. M., and Clarke, J. (1985). Measurements of macroscopic quantum tunneling out of the Zero-Voltage state of a Current-Biased josephson junction. *Physical Review Letters*, 55(18):1908–1911.

DiCarlo, L., Chow, J. M., Gambetta, J. M., Bishop, L. S., Johnson, B. R., Schuster, D. I., Majer, J., Blais, A., Frunzio, L., Girvin, S. M., and Schoelkopf, R. J. (2009). Demonstration of two-qubit algorithms with a superconducting quantum processor. *Nature*, 460(7252):240–244.

DiCarlo, L., Reed, M. D., Sun, L., Johnson, B. R., Chow, J. M., Gambetta, J. M., Frunzio, L., Girvin, S. M., Devoret, M. H., and Schoelkopf, R. J. (2010). Preparation and measurement of three-qubit entanglement in a superconducting circuit. *Nature*, 467(7315):574–578.

DiVincenzo, D. P. (2000). The physical implementation of quantum computation. *Fortschritte der Physik*, 48(9-11):771–783.

Fedorov, A., Steffen, L., Baur, M., and Wallraff, A. (2011). Implementation of a toffoli gate with superconducting circuits. *arXiv:1108.3966*.

Feynman, R. (1982). Simulating physics with computers. *International Journal of Theoretical Physics*, 21(6):467–488.

Göppl, M., Fragner, A., Baur, M., Bianchetti, R., Filipp, S., Fink, J. M., Leek, P. J., Puebla, G., Steffen, L., and Wallraff, A. (2008). Coplanar waveguide resonators for circuit quantum electrodynamics. *Journal of Applied Physics*, 104(11):113904–113904–8.

Grover, L. K. (1996). A fast quantum mechanical algorithm for database search. In *Proceedings of the twenty-eighth annual ACM symposium on Theory of computing*, STOC '96, page 212–219, New York, NY, USA. ACM.

Grover, L. K. (1997). Quantum mechanics helps in searching for a needle in a haystack. *Physical Review Letters*, 79(2):325–328.

Grover, L. K. (2001). From schrödinger's equation to the quantum search algorithm. *American Journal of Physics*, 69(7):769–777.

Haroche, S. and Raimond, J. (2006). *Exploring the Quantum: Atoms, Cavities and Photons*. Oxford University Press.

Josephson, B. (1962). Possible new effects in superconductive tunnelling. *Physics Letters*, 1(7):251–253.

Koch, J., Yu, T. M., Gambetta, J., Houck, A. A., Schuster, D. I., Majer, J., Blais, A., Devoret, M. H., Girvin, S. M., and Schoelkopf, R. J. (2007). Charge-insensitive qubit design derived from the cooper pair box. *Physical Review A*, 76(4):042319.

Lanyon, B. P., Hempel, C., Nigg, D., Müller, M., Gerritsma, R., Zähringer, F., Schindler, P., Barreiro, J. T., Rambach, M., Kirchmair, G., Hennrich, M., Zoller, P., Blatt, R., and Roos, C. F. (2011). Universal digital quantum simulation with trapped ions. *Science*, 334(6052):57–61.

Lloyd, S. (1996). Universal quantum simulators. *Science*, 273(5278):1073–1078.

Mallet, F., Ong, F. R., Palacios-Laloy, A., Nguyen, F., Bertet, P., Vion, D., and Esteve, D. (2009). Single-shot qubit readout in circuit quantum electrodynamics. *Nat Phys*, 5(11):791–795.

Martinis, J. M., Devoret, M. H., and Clarke, J. (1985). Energy-Level quantization in the Zero-Voltage state of a Current-Biased josephson junction. *Physical Review Letters*, 55(15):1543–1546.

Martinis, J. M., Devoret, M. H., and Clarke, J. (1987). Experimental tests for the quantum behavior of a macroscopic degree of freedom: The phase difference across a josephson junction. *Physical Review B*, 35(10):4682–4698.

Michael A. Nielsen and Isaac L. Chuang (2000). *Quantum Compuation and Quantum Information*. Cambridge University Press.

Mooij, J. E., Orlando, T. P., Levitov, L., Tian, L., van der Wal, C. H., and Lloyd, S. (1999). Josephson Persistent-Current qubit. *Science*, 285(5430):1036 –1039.

Motzoi, F., Gambetta, J. M., Rebentrost, P., and Wilhelm, F. K. (2009). Simple pulses for elimination of leakage in weakly nonlinear qubits. *Physical Review Letters*, 103(11):110501.

Nakamura, Y., Pashkin, Y. A., and Tsai, J. S. (1999). Coherent control of macroscopic quantum states in a single-Cooper-pair box. *Nature*, 398(6730):786–788.

Paik, H., Schuster, D. I., Bishop, L. S., Kirchmair, G., Catelani, G., Sears, A. P., Johnson, B. R., Reagor, M. J., Frunzio, L., Glazman, L. I., Girvin, S. M., Devoret, M. H., and Schoelkopf, R. J. (2011). Observation of high coherence in josephson junction qubits measured in a Three-Dimensional circuit QED architecture. *Physical Review Letters*, 107(24):240501.

Palacios-Laloy, A. (2010). *Superconducting qubit in a resonator: Test of the Leggett-Garg inequality and single-shot readout*. PhD thesis, Université Paris VI, Paris.

Pozar, D. M. (2011). *Microwave Engineering*. Wiley, 4 edition.

Reed, M. D., DiCarlo, L., Nigg, S. E., Sun, L., Frunzio, L., Girvin, S. M., and Schoelkopf, R. J. (2011). Realization of Three-Qubit quantum error correction with superconducting circuits. *arXiv:1109.4948*.

Schuster, D. I. (2007). *Circuit Quantum Electrodynamics*. PhD thesis, Yale University, New Haven.

Siddiqi, I., Vijay, R., Metcalfe, M., Boaknin, E., Frunzio, L., Schoelkopf, R. J., and Devoret, M. H. (2006). Dispersive measurements of superconducting qubit coherence with a fast latching readout. *Physical Review B*, 73(5):054510.

Siddiqi, I., Vijay, R., Pierre, F., Wilson, C. M., Metcalfe, M., Rigetti, C., Frunzio, L., and Devoret, M. H. (2004). RF-Driven josephson bifurcation amplifier for quantum measurement. *Physical Review Letters*, 93(20):207002.

Vijay, R., Devoret, M. H., and Siddiqi, I. (2009). Invited review article: The josephson bifurcation amplifier. *Review of Scientific Instruments*, 80(11):111101–111101–17.

Vion, D., Aassime, A., Cottet, A., Joyez, P., Pothier, H., Urbina, C., Esteve, D., and Devoret, M. H. (2002). Manipulating the quantum state of an electrical circuit. *Science*, 296(5569):886 –889.

Wallraff, A., Schuster, D. I., Blais, A., Frunzio, L., Huang, R.-S., Majer, J., Kumar, S., Girvin, S. M., and Schoelkopf, R. J. (2004). Strong coupling of a single photon to a superconducting qubit using circuit quantum electrodynamics. *Nature*, 431(7005):162–167.

Yurke, B. and Denker, J. S. (1984). Quantum network theory. *Physical Review A*, 29(3):1419–1437.